Convective transport by intermittent blob-filaments: comparison of theory and experiment

D. A. D'Ippolito[1], **J. R. Myra**[1] **and S. J. Zweben**[2]

[1]*Lodestar Research Corporation, Boulder, Colorado*

[2]*Princeton Plasma Physics Laboratory, Princeton, New Jersey*

December, 2010; revised March, 2011

Submitted to Phys. Plasmas

DOE/ER/54392-62 LRC-10-139

Lodestar Research Corporation

2400 Central Avenue #P-5

Boulder, CO 80301

Convective transport by intermittent blob-filaments: comparison of theory and experiment

D. A. D'Ippolito[†] and J. R. Myra

Lodestar Research Corporation, 2400 Central Avenue, Boulder, Colorado 80301

S. J. Zweben

Princeton Plasma Physics Laboratory, Princeton, New Jersey 08540

Abstract

A blob-filament (or simply "blob") is a magnetic-field-aligned plasma structure which is considerably denser than the surrounding background plasma and highly localized in the directions perpendicular to the equilibrium magnetic field **B**. In experiments and simulations, these intermittent filaments are often formed near the boundary between open and closed field lines, and seem to arise in theory from the saturation process for the dominant edge instabilities and turbulence. Blobs become charge-polarized under the action of an external force which acts unequally on ions and electrons; the resulting **E**×**B** drift moves the blobs radially outwards across the scrape-off-layer (SOL). Since confined plasmas generally are subject to radial or outwards expansion forces (e.g. curvature and ∇**B** forces in toroidal plasmas), blob transport is a general phenomenon occurring in nearly all plasmas. This paper reviews the relationship between the experimental and theoretical results on blob formation, dynamics and transport and assesses the degree to which blob theory and simulations can be compared and validated against experiments.

PACS: 52.30.-q, 52.35.Ra, 52.55.Dy, 52.55.Rk

†email: **dippolito@lodestar.com**

Table of Contents

I. Introduction

II. Overview of theory

A. Blob properties

B. Blob definition

C. Theoretical and simulation models

III. Basic blob characteristics

A. Blob motion

1. Charge polarization mechanism
2. Observation of blob / hole transport

B. Non-Gaussian statistics

IV. Overview of experimental results

A. Experimental tables

B. Diagnostics

C. Definitions

D. Analysis techniques

E. Location and structure

F. Potential and magnetic field

G. Scalings

H. Comparisons of different devices

I. Summary of experimental overview

V. Blob structure and intermittency

A. Density and potential structure and pulse shape

B. Skewness and Kurtosis

C. Probability distribution function

D. Statistical theories

VI. Scaling of ballistic motion and blob particle transport

A. Theory of blob transport

1. Blob equivalent circuit
2. Blob correspondence principle
3. Analytic blob velocity scalings

B. Experimental tests of theoretical scalings with blob size

1. Blobs
2. ELM filaments
3. Inter-machine comparison

C. Scaling of blob velocity with collisionality and magnetic geometry

1. Theoretical predictions
2. Experimental evidence for collisionality dependence
3. Experimental evidence for blob disconnection

D. More general convective transport

1. Other forces
2. X-point effects, divertor leg blobs and plate tilt

E. Blob stability

1. Most stable blob size
2. Effects of internal spin and external sheared flow

VII. Blob generation by turbulence

A. Blob birth zone: role of gradients and sheared zonal flows

1. Sheared flow regimes
2. No sheared flows: radial streamers
3. Weak sheared flows: blobs (L-mode)
4. Strong sheared flows: blobs (H-mode)
5. Blobs due to drift waves
6. Other nonlinear effects on blob formation

B. Blob generation rate

1. Estimates of blob birth rate and packing fraction
2. Experimental data

VIII. Ongoing and future work

A. Blob generated sheared flows

B. Ballooning and parallel transport

C. Electromagnetic effects on blob-filaments

D. Comparison of turbulence simulations with experiments

E. Modeling intermittent transport

F. Finite T_i effects

IX. Summary and discussion

Appendix: List of abbreviations and symbols

I. Introduction

Our understanding of edge turbulence and transport in fusion experiments has improved considerably in the past two decades. A rapidly growing body of theoretical, computational and experimental work has come together to provide a new physical picture of the radial convection of coherent plasma structures called "blob-filaments" or simply "blobs." These objects transport plasma across the open magnetic field line region known as the scrape-off-layer (SOL) and enhance the plasma interaction with the surrounding material boundaries. Several recent review articles have already described measurements of edge plasma turbulence in toroidal magnetic fusion devices,[1] theoretical progress in describing turbulent edge and SOL transport,[2-4] and the implications of these and other empirical results for SOL and divertor physics for ITER.[5] The purpose of the present review is to specifically compare theory, simulation and experiment in the area of blob transport, as a guide for future work. Our review will cover both toroidal fusion and basic plasma devices.

Theory and simulations predict that blobs and Edge Localized Mode (ELM)[6] filaments are born as a result of the nonlinear saturation of underlying edge turbulence or coherent magnetohydrodynamic (MHD) instabilities, respectively. Experimental observations show that these coherent objects are spatially localized in the two-dimensional (2D) plane perpendicular to **B**, resembling "blobs" of enhanced density against a lower-density background. They are spatially extended along the direction of the magnetic field, appearing as field-aligned "filaments" in a three-dimensional (3D) view of the SOL (see Fig. 1). They are also referred to as "mesoscale structures" because their perpendicular scale length is intermediate between the ion gyroradius and macroscopic machine dimensions. The blobs provide a mechanism for the convective radial transport of particles, heat, momentum and parallel current in the SOL. A more precise definition of a blob will be provided in Sec. II.

The concept of blob transport has emerged from a combination of experiments, computer simulations and analytic theory. Early experiments showed that large-amplitude, intermittent turbulence governs the edge of plasma devices. Plasma density fluctuations in the SOL can be comparable to the time-averaged plasma density ($\delta n / n \sim 1$), and the fluctuations are intermittent in both space and time. The existence of apparently coherent structures (blobs) in the turbulent SOL was first observed many years ago using fast cameras[7] and 2D probe arrays.[8-10] Around the same time, flux-driven 2D turbulence simulations were carried out in which the SOL density profile was free to vary in response to turbulence driven by an imposed flux.[11] As observed experimentally, the SOL fluctuations were found to be intermittent, and nonlinear saturation of the turbulence led to the formation of coherent structures and subsequent radial transport of the plasma.[11] Statistics of the turbulent transport were compared for both a linear plasma device and a tokamak.[12] It was shown that the probability distribution function (PDF) for the density fluctuations was skewed for positive fluctuations, which is consistent with the idea of large density structures propagating radially across the SOL. Moreover, the normalized PDF was very similar in the linear and toroidal devices, perhaps implying a common origin of the convective transport in both cases, despite the very different geometry and forces in the two devices.

The importance of this convective transport in tokamaks was illustrated by the discovery of the "main chamber recycling regime"[13] in Alcator C-Mod.[14] In this regime, a particle balance analysis showed that plasma flow in the SOL was dominated by transport to the main chamber walls rather than by flow along field lines into the divertor. A few years later Krasheninnikov proposed a simple analytic model to explain the particle transport mechanism in a physical regime relevant to SOL turbulence.[15] A second paper[16] extended the "blob model" to include the transport of heat and vorticity and illustrated several possible connections with the main chamber recycling regime (e.g. two-scale density and particle flux profiles, synergy of blob transport with neutral

recycling, and a critical particle flux for ionization-sustained equilibrium). This analytic work proposed a simple, general and robust transport mechanism that is a good candidate to explain the transport observed in the open field line regions of both linear and toroidal machines.

Over the past ten years, both probe and optical diagnostics have clarified the intermittent or blob-like structure of edge turbulence in tokamaks and other plasma devices. For example, a fundamental measurement using conditional sampling of Langmuir probe fluctuations on DIII-D[17] showed that radially convecting "intermittent plasma objects" (blobs) transported roughly 50% of the particle transport in the SOL.[18,19] Imaging diagnostics, such as the gas-puff-imaging (GPI) systems[20-22] on C-Mod and NSTX,[23] provided 2D data which was used to directly visualize the motion of the blobs and study the statistics of the turbulence. A large body of more recent experimental work will be discussed in following sections and compared with blob theory and simulations.

The interest in SOL convective transport has continued to grow in recent years because of its effect on plasma interactions with the first wall and divertor. By increasing the particle flux into the far SOL, blobs can increase unwanted interactions with limiters, radiofrequency (rf) antennas, and the first wall.[15,16] Blobs and ELM filaments can also carry heat across the SOL, possibly affecting the SOL width for parallel heat flow (spreading the heat load) and increasing the interaction with the far SOL.[24,25] Increased convective heat transport near the separatrix may also be correlated with the density limit in some tokamaks.[26-29] Finally, blob momentum transport may influence the edge velocity shear layer and thus the core plasma confinement, at least in L-mode plasmas. Theory and simulations suggest that it provides a mechanism for spinning up the edge plasma without deliberate external momentum input.[30,31]

In the present paper, we will compare the results of theory, simulations and experiment to assess the state of our knowledge of SOL convective transport. To do this,

we will adopt a rather broad view of what constitutes a blob (see Sec. II.B). Obviously there is a large increase in complexity as one proceeds from analytic theory to the coherent objects in involved in 2D or even 3D turbulence simulations, and finally to the turbulent objects measured in experiment. The important question is what all of these things have in common, and whether the combination of theory, simulation and experiment will eventually provide us with a theory of SOL transport that is both quantitatively predictive and qualitatively intuitive.

In this paper we will use the terms "blob" and "filament" interchangeably, as they denote the cross-field 2D and full 3D structure of the same object. These turbulent coherently-propagating objects have acquired a number of other names in the literature, but in this paper we will refer to all such objects as blobs (or filaments), whether they arise in theory, simulations or experiment.

Finally, it should be noted that the relation of ELMs to blobs is also briefly discussed in this review. While the physics of ELM generation is beyond the scope of this paper, it is important to point out that ELMs produce filaments of plasma that propagate across the far SOL in a manner similar to blobs[19,24,32-36] (see also Sec. VI.B.2). However, there seem to be some important differences between ELM filaments and turbulence-produced blobs, as pointed out in recent experiments. An ELM filament is typically larger in cross-sectional area and its plasma is denser and hotter than in a typical blob, and it can carry substantial parallel current.[33,36] There is some evidence[33] that, unlike blobs, one or more of the ELM footpoints can remain connected to the hot, dense edge plasma as the main body of the filament begins moving outwards across the SOL. Eventually, the ELM footpoints detach from the edge and the disconnected ELM propagates outwards like a blob. Some electromagnetic (EM) aspects of ELM-blob filaments are discussed in Sec.VIII.C.

The plan of our paper is as follows. We first give the theoretical perspective, and some initial motivation from experiments, in Secs. II (overview of theory) and III (basic

blob characteristics). These sections introduce the basic concepts, and some important definitions, including a working definition of a blob. This theoretical introduction is followed by a systematic discussion of experiments in Sec. IV. The purpose is to give an overview of blob experiments and a discussion of the difficulties inherent in comparing experiments and theory. The remainder of the paper discusses the comparison of theory, simulations and experiments for a number of topics: blob structure and intermittency (Sec. V), the scaling of blob particle transport in various regimes (Sec. VI), and blob generation by turbulence (Sec. VII). These are the areas in which most work has been done to date. In Sec. VIII we consider briefly a number of other topics in which some interesting theory-experimental comparisons have been carried out. A discussion of our conclusions is given in Sec. IX. A list of abbreviations and symbols can be found in the Appendix.

Finally, we note that blob generation and transport are discussed separately. Blob generation occurs in the edge and near SOL and is best studied statistically with edge turbulence simulation codes. Blob transport occurs in the far SOL and has been extensively studied using analytical methods and seeded-blob simulations. We discuss blob transport (Sec. VI) before blob generation (Sec. VII) because it is better developed, both theoretically and experimentally, and came first historically.

Table I – Theory and simulation of blobs

Topic	References
Analytic theory	
Blob dynamics	3,4,15,16,37-46
Blob velocity scalings	3,15,16,39,47-53
Pulse shape	3,37,38,41,49,50
Holes	38,41,53-56
PDF and skewness	3,11,31,46,53,55,57-62
Statistical theories	63-66
Blob stability	37,38,41-43,67-70
Non-curvature forces	3,71-75
X-point effects and divertor blobs	3,39,40,48,51,53,73-78
Blob generation, birth zone, and effects of **E**×**B** velocity shear	3,30,31,37,46,50,53,55,58,61,62,69,79-82
Blob birth rate (waiting time, packing fraction)	15,50,53,65,83,84
Blob transport of heat, momentum and current	16,29,31,50,56,59,62,69,81,82,85,86
Electromagnetic effects	3,39,45,48,56,70,87-92
Parallel transport	73, 84,86,93-95
Simulations	
Seeded blob simulations	37,38,41,42,44,49,50,57,67-70,96
2D SOL turbulence simulations	11,46,49,50,52,53,55,61,79,82,86,93,97-102
3D SOL turbulence simulations	20,21,40,74,77,88,103,104
Kinetic simulations	103
Comparison of turbulence simulations with experimental data	20,21,46,61,74,82,86,88,93,97,100,101,102
Comparison of convective transport simulations with experimental data	54,105-108
Review papers	3,4,38,47

II. Overview of theory

This section contains a brief overview of blob theory. The reader is referred to a recent review article[3] for an in-depth discussion of the theory. Many researchers have contributed to developing the theory and implementing it in computer simulations. Table I summarizes representative theoretical papers in this area. More detailed discussions of these theoretical points and their relation to available experimental results can be found in Secs. V – VIII.

A. Blob properties

Evidence from both theory and simulations suggests that blob and ELM filaments are created by the nonlinear saturation of turbulence or MHD instabilities in the edge plasma. Thus, blob generation and transport is closely related to the underlying linear physics. In tokamaks, theory predicts that the dominant instability in the SOL is usually a curvature-driven sheath-interchange[109,110] or resistive X-point[111-113] mode localized on the low-B ("bad curvature") side. Both simulations and experiments show that the blobs are typically born on the bad curvature side at the edge of the closed field line region, where the gradients are large and the turbulence is strong. The blobs convect outwards across the SOL, carrying filaments of plasma to the wall and become the dominant source of particle transport in the low-density region near the wall (called the "far SOL").

The blob model[3,15,16,38] provides a radial transport mechanism which is simple, robust, and gives order of magnitude estimates for the radial velocity that agree with experiments. It starts with the observation that a blob filament of enhanced density becomes charge polarized under the action of a net species-summed radial force[15] $\mathbf{F}$, as illustrated in Fig. 1. The electrons and ions move in opposite directions due to the $\mathbf{F}\times\mathbf{B}$ particle drift, and a blob charge polarization occurs if $\mathbf{b}\cdot\nabla\times\mathbf{F}\neq 0$. This charge polarization creates a poloidal electric field inside the blob, and the resulting $\mathbf{E}\times\mathbf{B}$ drift

moves the density blob in the direction of the force. For example, in a tokamak the curvature and $\nabla \mathbf{B}$ forces result in $\mathbf{E} \times \mathbf{B}$ blob motion that moves the plasma down the magnetic field gradient towards larger major radius R, viz. outwards towards the wall on the low-field side of the torus.

Other examples of forces which can produce blob convection include the centrifugal force for a rapidly rotating linear plasma device, and the "neutral wind" frictional force.[71] Each of these forces can be represented by an effective gravity in carrying out the analysis.[3,38] As discussed in Sec. III, experiments have been carried out in which each of these forces has been a candidate to explain the observed blob motion.

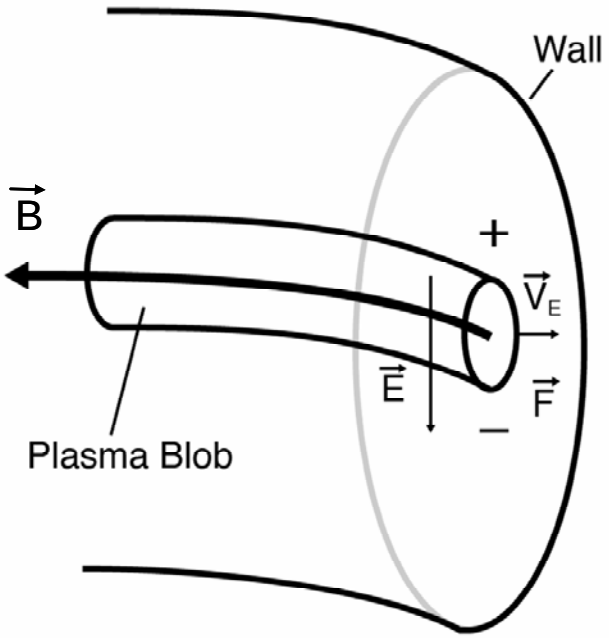

Fig. 1 Sketch of a plasma blob showing the charge polarization mechanism responsible for the radial transport.

This blob transport mechanism is a new application of an old idea. It is similar to the Rosenbluth-Longmire picture of interchange instability,[114] except that it is applied to an isolated density filament convecting across the SOL, rather than to a small sinusoidal

density perturbation oscillating around a fixed point. This is the physical basis for an analogy between the linear and nonlinear physics, and this correspondence has been used in computing various regimes of the theory. (See the discussion of the "blob correspondence principle" in Sec. VI.) Blob dynamics also have much in common with the motion of plasma clouds formed after ablation of injected pellets.[3,87,115-117]

A simplified mathematical model of blob dynamics requires two essential ingredients: the conservation of charge and density. Charge conservation $\nabla \cdot \mathbf{J} = 0$ results in the vorticity equation

$$\nabla \cdot \frac{d}{dt}\left(\frac{n m_i c^2}{B^2} \nabla_\perp \Phi \right) = \nabla_{||} J_{||} + \frac{c}{B} \mathbf{b} \cdot \nabla \times \mathbf{F} \qquad (1)$$

where the left-hand-side is the perpendicular (to **B**) current carried by the ion polarization drift, $J_{||}$ is the parallel (to **B**) current, and **F** is the charge-polarizing force. Here n is the density, m_i is the ion mass, and Φ is the electrostatic potential. Equation (1) describes the generation of the polarization potential Φ caused by the force **F** while $J_{||}$ mitigates the charge build-up through current flow. The plasma density (i.e. the blob) **E**×**B** drifts due to Φ, according to the continuity equation

$$\frac{dn}{dt} \equiv \frac{\partial n}{\partial t} + \mathbf{v}_E \cdot \nabla n = 0 \quad , \qquad (2)$$

which also defines the convective derivative d/dt used here and in Eq. (1). The **E**×**B** drift velocity is defined as $v_E = (c/B)\mathbf{b}\times\nabla\Phi$. Equation (2) can be generalized to include parallel loss terms, ionization sources, etc.

The magnitude of the **E** field induced by the external force is obtained by balancing the current source from the $\mathbf{F}\times\mathbf{B}$ drift with the parallel and perpendicular loss currents in the blob "electrical circuit".[3,48] Thus, a model for the parallel currents is needed. Different forces and parallel current regimes lead to models with different parameters and different scalings. In the tokamak SOL, the net radial $\mathbf{E}\times\mathbf{B}$ blob velocity

depends on the sheath and plasma resistivity, the magnetic geometry (parallel connection length to the divertor, presence or absence of X-points), and other parameters. This will be discussed in more detail in Sec. VI.

A number of parallel current "closure schemes" relevant to reduced 2D blob models have been discussed in the literature and are summarized in Ref.3. The simplest closure scheme appropriate to the SOL is the "sheath connected regime," which assumes that the blob parallel current is unimpeded by Spitzer resistivity along the field line, flows into the sheath, and is ultimately regulated by the sheath resistivity.[15,16] To obtain an analytic solution for the blob velocity in this regime, one assumes no background plasma and an isolated object with constant temperature and a density profile of the general form $n(x,y) = n_b(x)\ \exp[-y^2/(2\delta^2)]$, where $n_b(x)$ is an arbitrary function of x. This permits a variety of solutions encompassing both blobs and radial streamers.

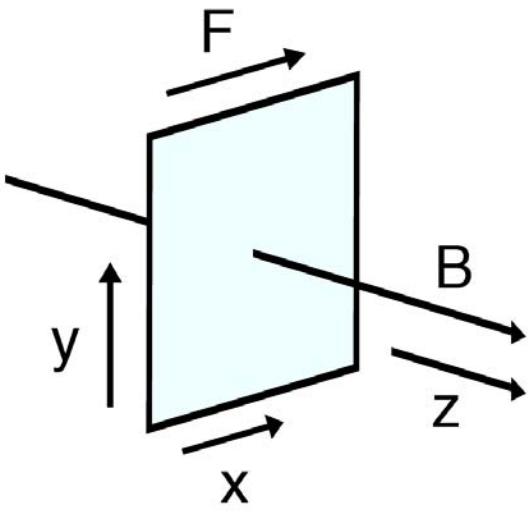

Fig. 2 Sketch of local SOL coordinates. The x coordinate is in the direction of the outwards force (typically radial). The y coordinate is in the binormal direction, $\hat{e}_y = \hat{e}_z \times \hat{e}_x$, and z is along the equilibrium magnetic field.

To facilitate the discussion of plasma devices with diverse geometries, we define here a local coordinate system for the SOL region in which the blobs propagate. We let (x,y,z) denote the local coordinates in the radial, binormal, and parallel (to **B**) directions. For example, in the SOL of a tokamak, y is approximately the poloidal direction, whereas in a linear machine it is the azimuthal direction. The x direction is in the direction of the outwards charge-polarizing force. These coordinates are illustrated in Fig. 2.

For present purposes, it is sufficient to consider a cylindrical blob with a Gaussian density profile, $n(r) = n_0 \exp[-r^2/(2\delta^2)]$, where $r^2 = x^2 + y^2$. The charge conservation (vorticity) equation can then be solved analytically for the case of the toroidal curvature and $\nabla \mathbf{B}$ forces ($\mathbf{F} \sim n m_i c_s^2 / R_c$) using the linearized sheath-connected parallel current closure, $J_{||} = ne^2 c_s \Phi / T_e$. Then, the system of equations (1) and (2) yields the solution[15,16] that the Gaussian density profile is stationary in a frame convecting with the blob velocity

$$v_x = c_s (L_{||} / R)(\rho_s / \delta)^2 . \qquad (3)$$

Here c_s and ρ_s are the sound speed and corresponding gyroradius, R_c and $L_{||}$ are the radius of curvature and sheath-to-sheath parallel connection length, and δ is the blob radius. (For elongated blobs or radial streamers, δ is the poloidal size.) The scaling of the blob velocity with δ varies from $v_x \sim \delta^{-2}$ in the sheath connected regime to $v_x \sim \delta^{1/2}$ in the inertial regime discussed in later sections.

The theory of blob transport has evolved from this simple beginning to include a number of generalizations motivated both by theoretical and experimental considerations. Some important generalizations are as follows:

- There are other forces (besides the curvature force) and closures (besides the sheath-connected limit), leading to a number of parameter regimes discussed in the literature (see Ref. 3 and Sec. VI). Some of the other regimes describe

highly collisional plasmas (interchange → ballooning or resistive-X point physics) and electromagnetic ELM filaments.

- The background density must be retained to understand the blob shape and velocity observed in experiments. (This can be done in simulations of seeded blobs, see Refs. 37 and 67 and Sec. VI.B.1).
- The effect of spatially varying temperature can be important for several reasons. For example, the blob velocity in the sheath-connected limit scales as $v_x \sim T_e^{3/2}$, suggesting that the blob velocity is smaller in the far SOL due to cooling. The slowing of blobs as they propagate into cooler regions has been observed in experiments. Also, if the sheath-connected blob has an internal temperature profile, $T_e(r)$, there will be an associated Bohm sheath potential $\Phi_B \approx 3T_e(r)$, where the electron temperature is evaluated at the sheath. The resulting radial electric field will cause the blob to spin, reducing the charge polarization and slowing the blob (see Sec. VI.E.2). Finally, if $T_i \neq 0$ the ion temperature contribution to the blob speed and dynamical evolution must also be taken into account. Note that the radial profiles of ion and electron temperature are often different in the SOL.
- The radial transport of heat, momentum and parallel currents can all be important in various contexts. This review will concentrate on the transport of particles because most experimental work has been done in that area.
- Also likely to be important is the effect of parallel variation along **B**. This has not yet been extensively studied but we suspect that a lot of the scatter obtained in comparing experimental data with 2D models is due to 3D effects.

All of these topics will be discussed in later sections of this review.

B. Blob definition

From the idealized theoretical picture of a blob described in the previous section, we can extract a definition of a blob which is general enough to encompass the objects that arise in theory, simulations and experiments. A blob is a filament of plasma which satisfies the following three properties:

(1) it has a monopole (single-peaked) density distribution with a peak value much higher than the surrounding rms fluctuations of the background plasma (typically $\geq$ 2-3 times higher);

(2) it is aligned parallel to the magnetic field **B** and its variation along **B** is much weaker than in the transverse direction, i.e. $\delta / L_{\|} << 1$;

(3) it has a dominant convective **E**×**B** velocity component in the direction of a charge-polarizing force, and an associated potential and vorticity with a dipole structure in the direction transverse to its propagation.

In trying to relate simulations and experiments to theory, a number of problems occur. Property (1) is often made quantitative by averaging over many instances of turbulent structures which satisfy a threshold in density or ion saturation current ("conditional averaging").[19,118,119] As discussed subsequently (Sec. IV.D), there are many ways to choose this threshold, and experimental and simulation results are sensitive to the choice of threshold. Property (2) is a consequence of the tendency of plasmas to spread rapidly along field lines, so that non-uniformities in the parallel direction are removed at the ion sound speed. Regarding property (3), it is easy to compute the radial component of the **E**×**B** velocity in simulations, but it is usually difficult to measure it in experiments. A proxy is used (such as the GPI image velocity of the blob), which complicates the comparison.[46] We should note here that not all of these three theoretical properties are measured in every experiment. These issues and other difficulties are discussed in Sec. IV.

C. Theoretical and simulation models

The physics described in Sec. II A has been incorporated at various levels into analytic theory and simulations. Before delving into a comparison of theoretical predictions and experimental results, it is important to understand the limitations of the various theoretical models that have been employed in the literature.

In the simplest situation of a sheath-connected blob with uniform interchange structure along **B**, Gaussian radial density profile and flat temperature profile, an *exact solution* of the coupled nonlinear vorticity and density equations exists,[15] and the blob-filament convects without distortion (i.e. it is constant in a moving frame). This case results in the blob velocity given by Eq. (3).

Analytical scalings for the blob velocity have been obtained in many other cases, as will be discussed in Sec. VI, but in all these other cases no exact analytic solutions are known. Scalings can be obtained only by rough approximations, e.g. estimating $\nabla_\perp \sim 1/\delta$. Furthermore, numerical solutions of the corresponding model equations indicate that the blob distorts as it propagates, and in some cases eventually breaks up completely. Often cold ion models neglecting T_i are employed for simplicity, even though the ion temperature is not negligible in the SOL. Thus in almost all cases, analytical estimates of the blob velocity have at best factor-of-two accuracy.

To address this difficulty, much of the recent work in blob theory has used simulation codes. Seeded blob simulations have been used to compute the blob velocity in more complicated situations.[37,41,49,51,67,69,70] (A seeded blob is an isolated density peak used to initialize a simulation run; its evolution in time and space is calculated by the simulation code.) Various fluid simulation models have been employed, differing in details of the precise form of the vorticity equation used (e.g. Boussinesq approximation and particular parallel current closures), and whether temperature is evolved as a dynamical variable or not. Most simulation work on seeded blob properties has been done

with 2D codes (in the x-y plane), although seeded blobs have also been studied using 3D models.[31,44]

In addition to seeded blob simulations, turbulence codes have been used to study the nonlinear saturation processes for the turbulence and to infer self-consistently the blob generation rate and statistics.[40,50,53,62,74,81,88] The plasma profiles due to the turbulent (blob) convection have also been compared with experiments.[46,52,93,100,102] A brief discussion of the comparison of turbulence simulations and experiments is given in Sec. VIII.D.

Finally, it should be mentioned that kinetic effects on blob dynamics are not necessarily negligible in most experiments. Blob perpendicular scales are often only a few 10's of ion Larmor radii ρ_i at the midplane, and can easily approach ρ_i in the highly sheared magnetic fields near an X-point. Also, parallel mean free paths are often not small enough to justify a Braginskii treatment of collisional transport along the magnetic field. Kinetic effects on blobs are largely unexplored theoretically, and will not be discussed further here, but we note recent application of a PIC code[103] to address this issue.

From the preceding discussion, it can be seen that both analytical and simulation models currently employed to study blob dynamics contain significant inherent inaccuracies which are rather difficult to estimate. These should be kept in mind in Secs. V – VIII, where a comparison of theory and experiment is attempted.

III. Basic blob characteristics

In this section, we expand on the basic concepts in Sec. II and discuss some areas of qualitative agreement between theory and experiment. We also introduce the subject of non-Gaussian statistics and give some definitions which provide useful background for the experimental overview in Sec. IV.

A. Blob motion

1. Charge polarization mechanism

As discussed in Sec. II, examples of forces which can produce blob convection include the curvature and $\nabla \mathbf{B}$ forces in toroidal devices, the centrifugal force for a rapidly rotating linear plasma device, and the "neutral wind" frictional force.[71] Each of these forces can be represented by an effective gravity **g** in carrying out the analysis,[3,38] i.e. $\mathbf{F} = n m_i \mathbf{g}$. Experiments have at least tentatively attributed blob motion to each of these forces. The curvature force $\mathbf{F} \sim n m_i c_s^2 / R_c$ is often the dominant convective transport drive in tokamaks, stellarators, spherical tori and simple torus devices without a rotational transform. Theory predicts that the curvature-driven (resistive ballooning) linear eigenmode will peak at the midplane on the low-field side of the torus where the curvature is unfavorable. Thus, one expects that the turbulence will be strongest, and the blob transport greatest, at the outer midplane. Such a ballooning structure (i.e. in-out asymmetry) has been observed on several machines.[21,159,160] The neutral friction force was invoked to explain the blob motion observed in the linear device LAPD,[130] and the centrifugal force is probably the dominant effect in the rotating PISCES experiment.[243] More general forces will be discussed in later sections.

2. Observation of blob / hole transport

Theory predicts that a blob with *higher* density than that of the background SOL plasma will transport particles in the direction of the charge-polarizing force; regions of *reduced* density (density holes) would travel in the opposite direction. Simulations of seeded hole transport have been carried out to illustrate this effect.[54] Measurements of blob outward transport using conditional sampling are reported in many experiments [e.g. Refs. 18,19,24,125,126,144,169 while evidence for holes moving inward can be found in Refs. 126,129,130,144,158,159,169,180. Holes can originate near the last closed flux surface (LCFS) as a consequence of the nonlinear saturation of the interchange instability: the density maxima become blobs and density minima become holes.[3,53] This

theoretical picture is supported by the skewness profiles observed on many tokamaks (discussed in Sec.V.B) and by recent measurements on JET[144] and the simple magnetized torus TORPEX,[132,202,204] e.g. see radial velocity plots in Fig. 5 in Ref. 144 and the blob/hole trajectory histogram in Fig. 4 of Ref. 202. Theory also suggests that holes created near the wall provide a mechanism for the inward transport of impurities.[54,120]

In experiments, and in computer simulations of edge turbulence, blob-filaments appear to be born near the edge of the confined plasma due to the nonlinear saturation of turbulence or MHD instabilities (Sec. VII). The turbulent objects obtained in this way are much more complicated and irregular than the idealized objects treated analytically in the blob model. Nevertheless, as noted above, blob formation and subsequent radial transport is routinely seen in experiments[18,19,21,125,130,134,135,202] and in turbulence simulations that allow full profile modification.[40,41,50,55,59,62] The scaling of the blob radial velocity with blob size and other parameters depends on the current path through the blob (Sec. VI) but in most cases the predictions for the magnitude of the radial velocity are in order-of-magnitude agreement with experiments, $v_x \sim 0.01 - 0.1\, c_s$.[3,129,130,138]

B. Non-Gaussian statistics

Another area with abundant experimental data is the statistical analysis of SOL fluctuations. The data can be compared qualitatively with some aspects of the blob model and quantitatively with turbulence simulations. An important result from the statistical analysis of SOL fluctuations is their *intermittent* and *non-Gaussian* character. This is usually expressed in terms of the probability distribution function (PDF), $P_X(x)$, which denotes the probability that a fluctuating quantity X lies between x and x + dx. Propagation of blob-filaments provides a mechanism for explaining the spatial and temporal intermittency (e.g. large positive skewness) and the non-Gaussian PDF of fluctuations observed in the SOL of edge turbulence simulations and experiments.

Examples of intermittent fluctuations from both an experiment and a simulation are shown in Figs. 3 and 4. The time history of the ion saturation current signal is plotted in Fig. 3 for three radial positions in the edge and SOL of the JET tokamak.[45] Fluctuations which are positive (compared with the mean) predominate in the far SOL [case (a)]. Roughly equal numbers of positive and negative fluctuations about the mean occur in the edge velocity shear layer [case (b)], and negative fluctuations predominate in the edge plasma inside the velocity shear layer [case (c)]. The data in Fig. 3 is qualitatively consistent with the physical picture (Sec. VII) that the interchange instability grows and saturates nonlinearly[9,121] to produce blobs [the intermittent positive bursts in Fig. 3(a)] and holes [the intermittent negative bursts in Fig. 3(c)].[53]

The emergence of intermittency is ubiquitous in simulation models using equations similar to Eqs. (1) and (2). An example with a sheath closure for $J_{||}$ and curvature drive for the force term[79] is shown in Fig 4. Other examples of simulations containing blob turbulence are discussed in Sec. VIII.D. These models all contain the physics of interchange-like instabilities in the presence of nonlinear convection of density and vorticity. The qualitative similarity of the models to the experimental edge fluctuation data is a clue that they contain at least some of the essential physics to describe the statistics of blob-induced fluctuations in experimental SOL plasmas.

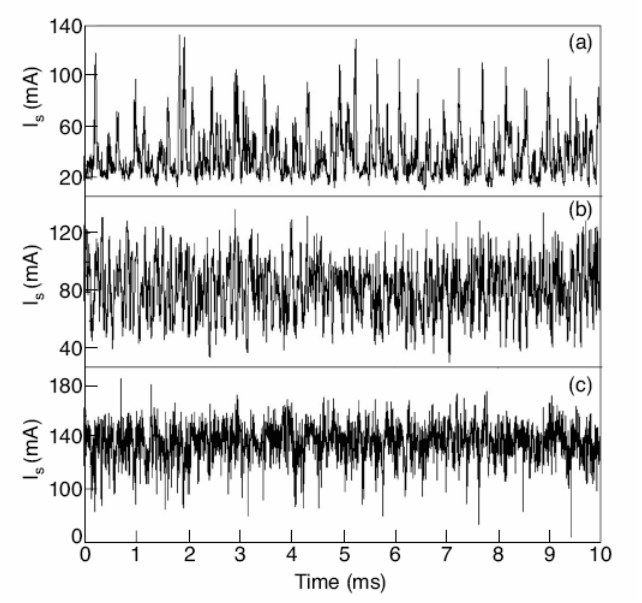

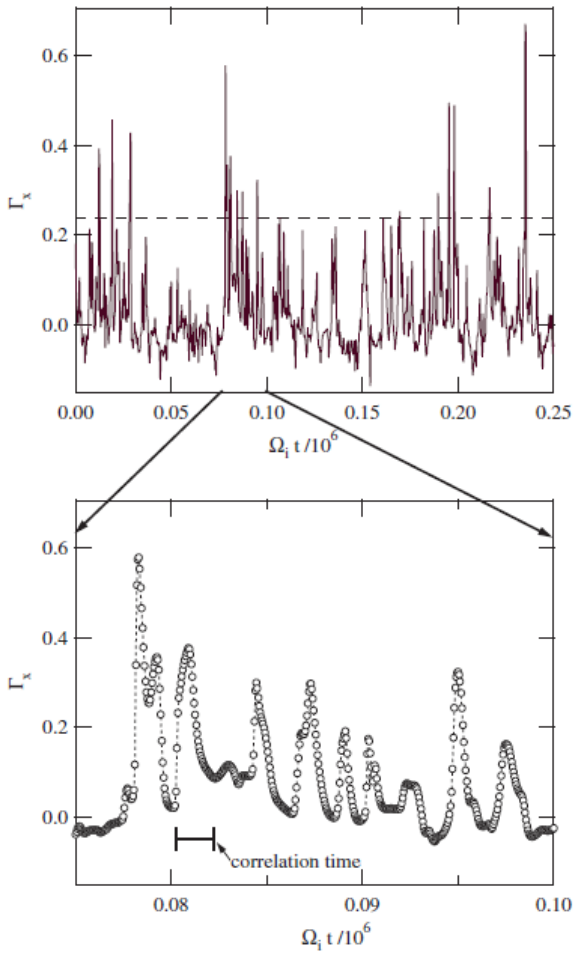

Fig. 3 (above left) Example of intermittent SOL fluctuations in the JET tokamak: time history of the raw ion saturation current I_S at three radial positions ($\Delta r \equiv r - r_{LCS}$): (a) positive bursts (relative to the mean) dominate in the SOL ($\Delta r = 28$ mm); (b) positive and negative bursts are nearly equally balanced in the edge velocity shear layer ($\Delta r = -10$ mm); and (c) negative bursts are prevailing just inside the edge velocity shear layer ($\Delta r = -18$ mm). Reprinted from Ref. 45 with permission from the American Institute of Physics.

Fig. 4 (above right) Example of intermittent fluctuations from a simulation code: time history of the particle flux for a system of equations rather similar to Eqs. (1) and (2) with sheath closure and curvature drive for the force term. Reprinted from Ref. 79 with permission from the International Atomic Energy Agency.

In most experiments, the measured fluctuations in the SOL are large ($\delta n / n \sim 0.1-1$), with significant correlation between density and potential fluctuations. Since density is a positive definite quantity, order unity density fluctuations necessarily imply positive skewness and a departure from a Gaussian PDF. Langmuir probe measurements of the fluctuating ion saturation current ($I_s \propto n_e \sqrt{T_e + T_i}$) give information on the density fluctuations, and measurements of the floating potential are used to estimate the plasma potential fluctuations. This information allows detailed statistical analysis of the turbulent SOL transport. The intermittency can be characterized [e.g. see Ref. 2] by constructing the PDF and by computing the higher central moments of the fluctuating quantities, i.e.

$$F_p(X) = N^{-1} \sum (X_j - \overline{X})^p / \sigma_X^p , \qquad (4)$$

where N is the number of data points in the time series of the variable X, the summation is over all data points, $\overline{X} = N^{-1} \sum X_j$ is the mean and $\sigma_X = \sqrt{N^{-1} \sum (X_j - \overline{X})^2}$ is the standard deviation of X. The skewness $S \equiv F_3$ measures the positive-negative asymmetry of the PDF, and the kurtosis $K \equiv F_4 - 3$ measures the "flatness" of the PDF, i.e. whether the distribution is more peaked or flatter than a normal distribution. Large K implies a long tail in the distribution. Gaussian turbulence has S = 0 = K, whereas S and K are positive in the SOL when blobs are present. A more detailed discussion of the statistical characterization of blobs is given in Sec. V; the present brief discussion of concepts and definitions will be useful in the overview of experimental results which follow.

IV. Overview of experimental results

A wide variety of measurements and experiments over the past 10-15 years have clarified the intermittent or blob-like structure of edge turbulence in both fusion and basic plasma physics experiments. Tables II and III list ~ 100 papers on ~ 40 devices on which explicit measurements of blob-like structures have been made, along with a list of the

main topics studied and references. General reviews of experimental results on edge plasma turbulence, which includes both blobs and background Gaussian turbulence, can be found in Refs. 1,10,122-124.

The qualitative definition of a blob in this experimental context is simply an unusually large positive density perturbation passing through the measurement point (important nuances are discussed in Sec. IV.C). Because the density is positive definite, sufficiently large perturbations are necessarily positive and their statistics are necessarily non-Gaussian. The significance of these blob-like structures was pointed out by measurements which showed that radially convecting blobs (or "intermittent plasma objects") caused an order unity fraction of the particle flux in the scrape-off-layers, e.g. in DIII-D,[18] TEXTOR,[125] HL-2A,[126] MAST,[127] among other devices. This suggests that the physics of blobs is important for an understanding of the heat and particle fluxes to the wall of magnetic fusion devices. The study of blobs has also been motivated by their basic plasma physics, and detailed measurements on devices such as TORPEX [see Table III] have attempted to make quantitative comparisons with the theory of blob creation and radial propagation.

Figures 5 - 11 show measurements of the 2D structure of blobs in the plane perpendicular to **B** from several different devices using different diagnostics and different analysis techniques; namely: NSTX[128] and Alcator C-Mod[21] using GPI, DIII-D using beam emission spectroscopy (BES),[129] and LAPD,[130] VTF,[131] W7-AS,[119] and TORPEX[132] using Langmuir probes. The common feature of these measurements is a localized region of unusually high density typically ~ 1-3 cm in size, which moves radially outward in this plane, typically at ~ 0.5-2 km/sec. This wide variety of structures and motions illustrates the commonality as well as the complexity of these blob structures.

This section gives an overview of the experimental measurements on blobs, while the comparison with blob theory and simulations is discussed in Secs. V - VIII.

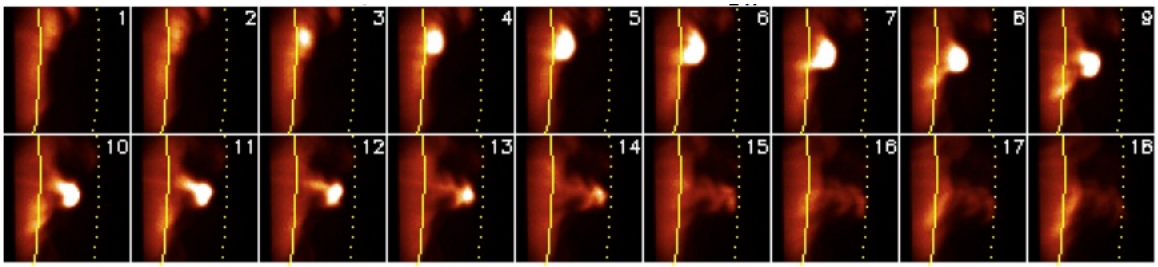

Fig. 5 (color online) Blob creation and propagation in NSTX as seen by the GPI diagnostic.[128] The image frame rate is 7.5 μs/frame and the field of view is ~25x25 cm near the outer midplane separatrix (solid line). This bright blob forms near the separatrix and moves radially outward toward the limiter shadow (dashed line) at ~ 1 km/sec. Reprinted from Ref. 128 with permission from Elsevier.

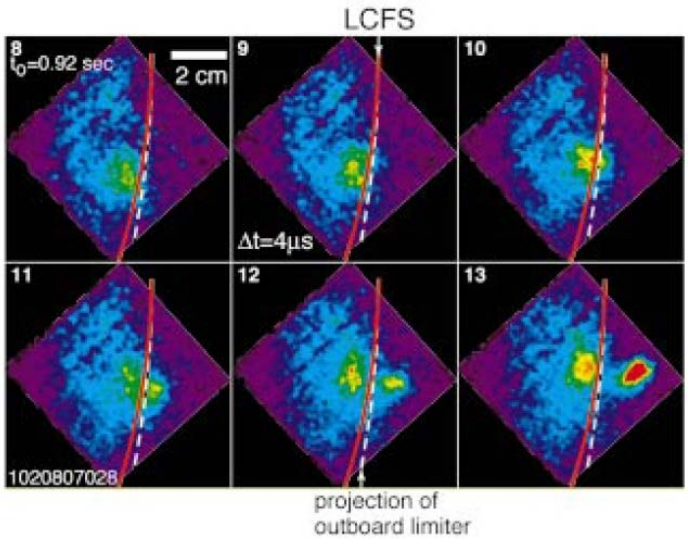

Fig. 6 (color online) Blob creation just inside the separatrix in Alcator C-Mod as seen by the GPI diagnostic.[21] The image frame rate is 4 μs/frame and the field of view is ~6x6 cm near the outer midplane separatrix (solid red line). The blob moves outward behind the toroidal projection of the outboard limiter (white dashed line) at ~ 1 km/sec. Reprinted from Ref. 21 with permission from the American Institute of Physics.

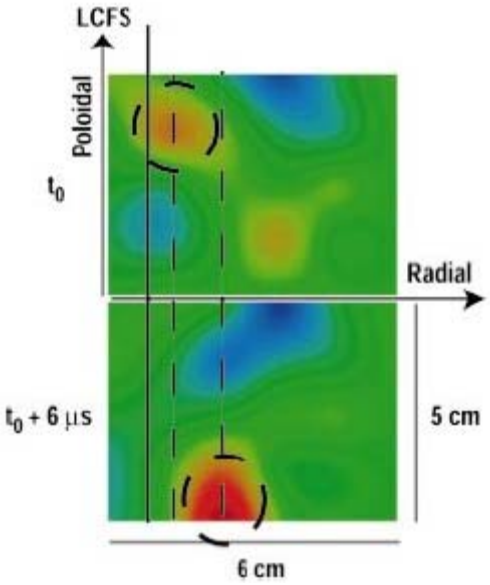

Fig. 7 (color online) Two frames of 2D density plots from the BES diagnostic of edge turbulence on DIII-D.[129] There is a time difference of 6 μs between frames. Red indicates high density and blue low density. A structure, marked with a dashed circle and shown in both frames, features poloidal and radial motion. Reprinted from Ref. 129 with permission from the American Institute of Physics.

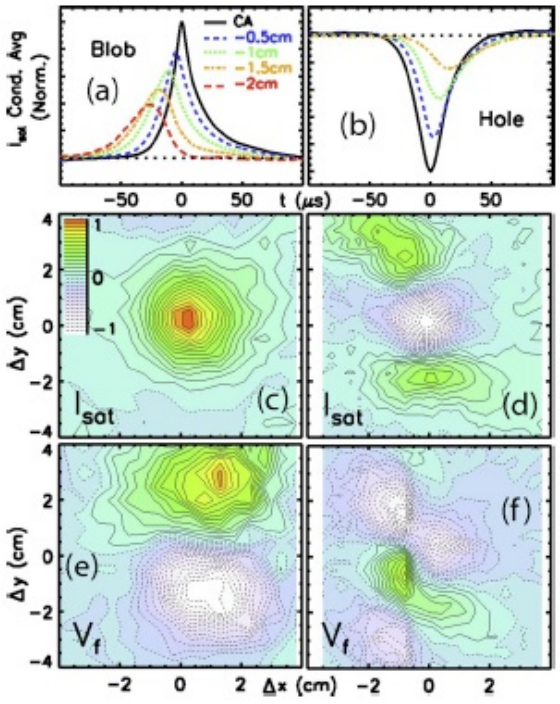

Fig. 8 (color online) Blob and hole structures in the linear device LAPD.[130] In (a) and (b) are cross-conditional averages of Isat on the linear probe array for blob and hole events (respectively), showing apparent propagation of blobs out of the plasma and holes back into the plasma. Also shown are two-dimensional cross-conditional averages of blob (c) I_{sat} and (e) V_f, and hole (d) I_{sat} and (e) V_f , over an 8 cm x 8 cm area perpendicular to **B**. All 2D conditional averages are normalized to the maximum of the absolute value of the average, and the color bar in (c) applies to all images. Reprinted from Ref. 130 with permission from the American Institute of Physics.

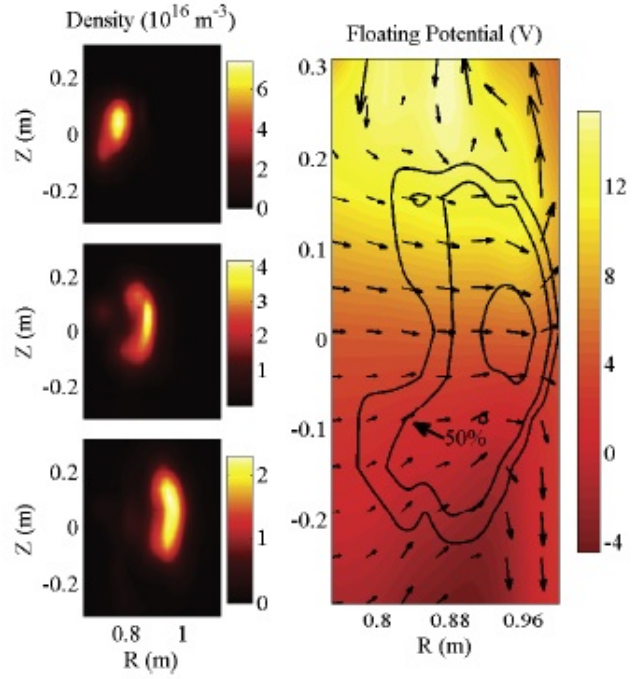

Fig. 9 (color online) Radial propagation of intentionally-created blobs in the toroidal device VTF.[131] At the left is the poloidal cross section over ~ 40 cm x 40 cm of a typical blob at 3 different times (Δt =100 μs), showing the characteristic mushroom shape. The density is calculated from ion saturation current; its decrease is consistent with the expansion of the blob. The blob propagation is consistent with the vertical electric field, which is reflected in the potential structure at right. The overlaid **E**×**B** velocity arrows show the velocity field of a vortex pair. Reprinted from Ref. 131 with permission from the American Physical Society.

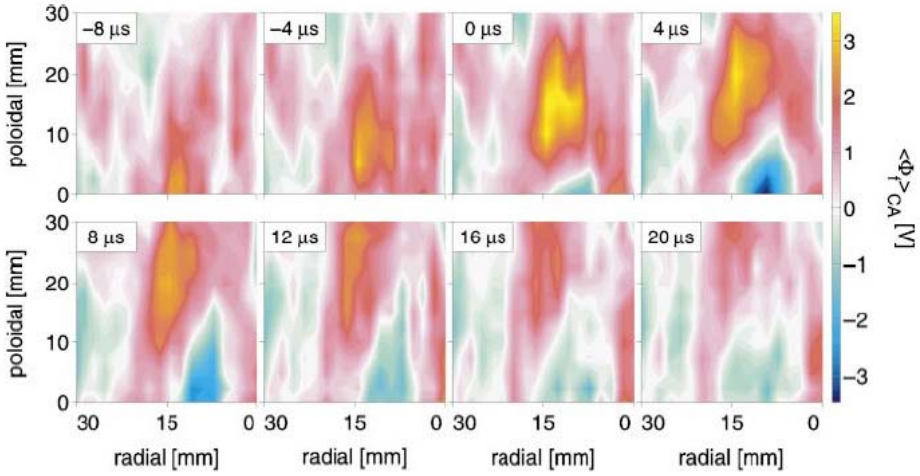

Fig. 10 (color online) Two-dimensional representation of the edge turbulence structures in W7-AS.[119] The color scale shows the results from conditional averaging of ion saturation current fluctuations for different time-lags from -8 µs to +20 µs over a 3 cm x 3 cm field of view. The radial position r=0 is the approximate position of the last closed flux surface (LCFS), and positive values are into the SOL. Reprinted from Ref. 119 with permission from the American Institute of Physics.

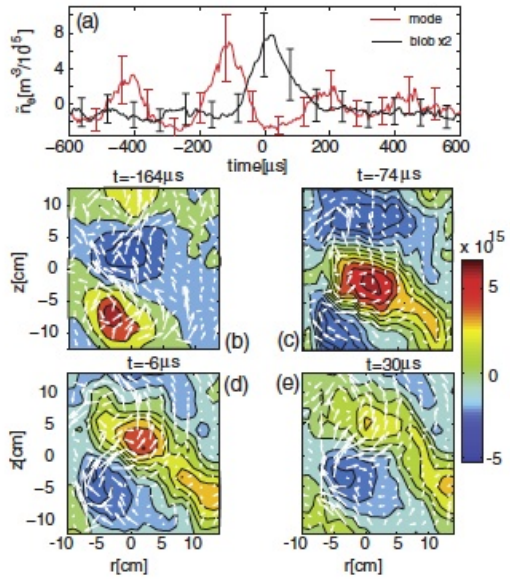

Fig. 11 (color online) Blob generation observed in the ion saturation current signals from a 20 cm × 20 cm probe array obtained from the conditional sampling technique in TORPEX.[132] In (a) is a time history of $\tilde{n}_e$, including uncertainties, in the mode region (red) at r = 1 cm and z = 5 cm, and in the source-free region (black) at r = 13 cm and z = 5 cm. Note that the latter is multiplied by two for clarity. Parts (b)–(e) show 2D profiles of $\tilde{n}_e$ at different times during blob ejection. The arrows show the instantaneous $v_{E\times B}$ profile. Reprinted from Ref. 132 with permission from the American Physical Society.

A. Experimental Tables

Table II summarizes experimental results on blobs in toroidal magnetic fusion devices, including tokamaks, stellarators, and reversed field pinches. Most of these measurements were made in the 'scrape-off layer' (SOL) of these devices, which is the region of open magnetic field lines outside the separatrix (in diverted machines) or outside the last closed flux surface (in limited machines). The average plasma temperature and density in the SOL of these machines ranges over $n \sim 10^{11}$-10^{13} cm^{-3} and $T_e \sim$ 1-100 eV. Most of these measurements were made using Langmuir probes or optical imaging techniques such as Beam Emission Spectroscopy (BES) or gas puff imaging (GPI). This table does not include measurements of blob-like structures which occur during strong MHD activity such as ELMs, which are discussed briefly in Sec. VIII.C.

Table III summarizes experimental results on blobs in basic plasma physics experiments, including linear devices and simple toroidal devices in which there are no closed magnetic field lines. Several of these measurements were made using Langmuir probe arrays across the whole plasma cross-section, which is possible due to the low average plasma density and temperature $n \sim 10^{10}$-10^{12} cm^{-3} and $T_e \sim$ 1-10 eV, so that the heat flux to the probes is tolerable.

Table II - Blobs in toroidal magnetic fusion devices

machine	skewed PDF	radial speed	blob size	birth rate	scaling	flux	References
tokamak							
DIII-D	×	×	×	×	×	×	18,19,24,129,133
NSTX	×	×	×				22,134-136
C-Mod	×	×	×	×	×		21,137-141
JET	×	×	×				142-144
TEXTOR	×	×				×	125,145-147
JT-60U	×					×	148-150
T-Supra	×	×		×			151-155
TCV	×				×		52,93,100,156,157
T-10	×	×	×	×		×	158-160
MAST	×	×			×	×	33,127,161-163
CASTOR	×	×					164-167
ASDEX-U	×			×	×		168,169
ADITYA	×	×				×	170-173
SINP	×	×	×			×	174,175
HYBTOKII	×				×		176
HL-2A	×	×	×	×		×	126
Caltech	×	×	×				8
HT-7	×		×				177
CT-6B	×		×				178
QUEST	×	×	×				179
stellarator							
LHD	×	×			×		180-182
W7-AS	×	×	×				119,183
TJ-K	×	×	×			×	60,184
TJ-II	×	×	×	×	×		185,186
Reversed - Field Pinch							
RFX	×		×		×	×	187-193
T2R	×					×	188,189,194,195
TPE-RX	×		×				196,197

Table III - Blobs in basic plasma devices

machine	skewed PDF	radial speed	blob size	birth rate	scaling	flux	References
toroidal							
TORPEX	×	×	×	×	×	×	132,198-209
VTF		×	×		×		131
Blåmann			×			×	210-212
Helimak	×		×				102
Teddi	×	×	×				213,214
Thorello	×	×	×	×			215
linear							
LAPD	×	×	×		×		130,216,217
Vineta	×	×		×		×	218,219,220,221
CSDX	×	×	×				222
PISCES	×	×		×			12,223
Mistral	×		×		×		224-226
NAGDIS II	×	×				×	227
LMD-U		×					228
Riso Q	×		×			×	118,229

The column headings of Tables II and III list various properties of blobs which have been measured for each device. The first column *'skewed PDF'* has a '×' for each device for which a positively-skewed, non-Gaussian probability distribution function was measured in the density, which is a necessary condition for the detection of intermittency or blobs (with the exception of VTF, Blåmann, and LMD-U, in which intermittent structures were detected by 2D probe arrays). The second and third columns labeled *'radial speed'* and *'blob size'* have a '×' for devices which have measured these 2D properties. Although a PDF can be obtained from a single-point measurement (such as the ion saturation current in a Langmuir probe), at least a two-point measurement is needed to determine the blob size and/or speed, and a multi-point probe array or 2D optical imaging technique is needed to track the blob trajectories in the plane perpendicular to the local magnetic field. The column *'birth rate'* refers to an estimate of the local blob birth rate, the column *'scaling'* refers to some variation in blob properties measured under differing plasma conditions, and the column *'flux'* refers to measurements of the particle or heat flux associated with blobs.

B. Diagnostics

Ideally, experiments on blobs should measure the space vs. time evolution of the local density, temperature, electrostatic potential, magnetic field, and plasma velocity in 3-D over the scales characteristic of the blob size and lifetime ($\geq$ 1 mm and $\geq$1 μsec). This is normally beyond the range of edge diagnostics in toroidal fusion devices, but can be accomplished to a good extent on basic plasma devices such as TORPEX (see Table III).

Most of the measurements of blobs in Tables II and III have been made using Langmuir probes to measure ion saturation current and floating potential with the desired space and time resolution. The local radial blob speed is often inferred from $\mathbf{V}_r = c\mathbf{E}_\perp \times \mathbf{B} / B^2$, where $\mathbf{E}_\perp$ is obtained from the difference in floating potential between

two nearby probes. Alternatively, the blob speed and average trajectory can be measured by the conditional sampling technique using one fixed probe and one movable probe (see Sec. IV.D), or by direct blob tracking using a 2D probe array. Two diagnostic issues for probes are the quantitative interpretation of their results (since the theory of probes in a magnetic field is still incomplete), and the possible perturbing effects of the probes on the plasma.[230] There are relatively few papers in which these issues are discussed in detail. Normally some checks are made that the insertion of an additional probe does not affect the results from existing probes, but it is often not clear whether the structure and motion of blobs is unaffected by these probes.

Optical diagnostics such as beam emission spectroscopy (BES) in DIII-D[129] and TEXTOR[231] and gas puff imaging (GPI) in Alcator C-Mod,[21] RFX-mod[191] and NSTX[136] have used atomic line emission from injected neutral atoms to measure the 2D structure of blobs over an extended radial vs. poloidal region with nearly ~1 mm and/or ~1 μsec resolution. These diagnostics require a local neutral source, either from a neutral beam or a neutral gas puff. Some checks have been made that the addition of such a source does not affect the local plasma or turbulence, at least up to the point when the radiation or fueling begins to affect the local edge plasma parameters, but this has not been well quantified. The global filamentary field-aligned structure of blobs has also been observed using visible light emission from electron excitation of background neutrals in MAST,[33,163] QUEST,[179] and Alcator C-Mod.[138]

Some indication of the reliability of these diagnostics can be obtained from direct comparisons of blob properties measured in two different ways. In DIII-D the blob size and radial skewness profile measured with probes was similar to that measured using BES.[18,129] In Alcator C-Mod there was a fairly high correlation coefficient between a movable probe near the X-point and GPI diodes near the outer midplane.[138,141] Measurements in NSTX have shown a good correlation between the midplane turbulence seen with GPI (i.e. D_α light) and passive measurements of divertor plate filament

structures seen with LiI light.[136] A good correlation was observed between blobs measured by optical imaging and Langmuir probes on MAST,[163] CSDX,[222] and TPE-RX.[197] A close connection between the radial speed inferred from $\mathbf{E}\times\mathbf{B}$ and blob tracking measurements was obtained in VTF[131] and QUEST.[179] The range of electron density and temperature seen in Thomson scattering measurements of the SOL in DIII-D[18] and NSTX[134] was also consistent with the presence of large positive structures, i.e. blobs. Large-scale structures in the edge of ASDEX Upgrade (ASDEX-U) have also been directly observed inside the separatrix with 2D Thomson scattering.[232]

Other types of turbulence diagnostics have seen limited use for the study of blobs. Electromagnetic diagnostics such as microwave reflectometry,[1] microwave scattering,[183] phase contrast imaging[181] generally do not have enough 2D spatial resolution to detect a localized blob. A heavy ion beam probe diagnostic has been used to identify radially-elongated streamer-like structures in JIPP T-IIU tokamaks.[233] An optical line ratio technique has recently been used to measure simultaneously the local density and electron temperature in blobs.[191]

C. Definitions

The experimental definition of a blob has varied in the literature depending on available diagnostic information, and to some extent on the theoretical context for the measurements. In general, the minimum requirement for the identification of a blob is a single-point measurement of a positively skewed, non-Gaussian probability distribution function in the plasma density, and almost all of the measurements in Tables II and III meet this requirement. A positively skewed PDF corresponds qualitatively to the presence of a large positive density perturbation passing across the measurement point. (See Sec. V.B for some important subtleties.) However, there is no quantitative skewness 'threshold' needed to meet this requirement, or any other universal experimental definition of a blob.

The reason for this ambiguity in the definition of a blob is the intrinsic variability and complexity of the blob structures observed in these experiments, as illustrated in Figs. 5 - 11. Simple blob properties such as their size and speed tend to show an order-of-unity variation even for a single location within a single device for a fixed set of external plasma parameters. Furthermore, the distinction between the non-Gaussian blob-like structures and the Gaussian 'background' turbulence is usually not sharp, since the non-Gaussian structures apparently evolve from the Gaussian background turbulence. A similar complexity and ambiguity exists in the definition of 'coherent structures' in neutral fluid turbulence and other fields.[234]

Obviously the blob birth rate, size, lifetime, and speed can be sensitive to the exact definition and analysis method used to identify and track these structures. A plasma blob is most commonly identified by some threshold in the local plasma density signal or its proxy (e.g. the ion saturation current); however, the exact criterion has varied from one experiment to another. For example, a blob (or 'intermittent plasma object') in DIII-D was defined to occur when the ion saturation current in a probe was more than 2.5 times a standard deviation (i.e. 2.5σ) above the time-averaged mean for that probe.[18,129] The criterion used to define blobs varied from 2.5σ-3σ for probe measurements on T-10[158] and TEXTOR,[125] 3σ for GPI measurements in Alcator C-Mod,[138] and was varied up to 2.5σ in JET[144] and up to 4.7σ in TORPEX.[204] In the Caltech tokamak[8] and NSTX[134] a threshold of about 0.7 times the maximum signal level was used as the main defining criterion. In contrast, some work on TORPEX applied an additional criterion which selected only structures which moved radially and maintained a consistent structure.[198] In RFX-mod[191,235] and several other devices[22,150,152] a wavelet decomposition technique allowed a continuous resolution of the blob structures in terms of their space vs. time scales.

The ambiguity in the definition of a blob should be kept in mind when trying to compare the experimental results from different devices, or experimental results with

theory. Partly for this reason, the most reliable results for 'scaling' of blob properties come from variations within a single device, or when the same definition of a blob is used in comparisons between experiment and theory.

D. Analysis techniques

After the diagnostic data has been obtained and a definition of a blob has been formulated, the blobs properties can be evaluated using appropriate data analysis, e.g. the blob speed, size, radial speed, birth rate, and radial transport effects (as listed in Tables II and III). However, there is no universal analysis technique for any of these quantities, so possible ambiguities in the analysis should also be kept in mind when comparing the results from different devices.

For example, the radial blob speed in DIII-D[129] and several other devices [see Tables II and III] has been analyzed using the local E_{pol} measured by a pair of floating probes located within a correlation length of the probe used to identify a blob based on its ion saturation current level. The resulting $\mathbf{V}_r = c\mathbf{E}_\perp \times \mathbf{B}/B^2$ speed is a good approximation to the blob radial speed, but only if the effect of electron temperature fluctuations on the floating potential is negligible, and if the probes do not have a significant perturbing effect on the blob motion. The local radial particle transport can also be derived from this analysis as $\Gamma_r = < n V_r >$, where the density fluctuations n are derived from the ion saturation current. However, fundamental uncertainties in the theory of Langmuir probes in a magnetic field imply that the density and resulting flux cannot be evaluated this way to better than about a factor-of-two. The local radial heat transport due to blobs $Q = < T_e V_r >$ can also be evaluated if the local T_e in a blob can be measured, which has only rarely been attempted.[18,129,175,205]

Another technique used to evaluate the blob radial velocity is 'conditional sampling' or 'conditional averaging', which is usually implemented by 'triggering' on a blob as detected by a fixed probe, and then recording the signal in another probe for times

close to the blob trigger in the first probe. For example, using a multi-tip probe[18,129], the electron temperature in blobs in the SOL of DIII-D was estimated this way to be T_e = 150 eV, which was almost 3 times the background temperature. If the second probe is movable, the 1D or 2D space vs. time motion of the blob can be mapped out from the time delay between the blob trigger event and the time of the maximum signal level at another location, e.g. Ref. 138. However, the conditional sampling technique assumes that the blob trajectory in space and time is reproducible over an ensemble of blob triggers, so if the blob trajectories vary significantly from one trigger event to another, this ensemble average will not be very meaningful. Some discussion of limitations and variants of this method, tests for its significance, and comparisons with other analysis methods are in Refs.[118,119,150,152,164,224,229].

Other types of analysis can be done if a full 2D set of data is available, e.g. using a 2D probe array or an imaging technique such as BES or GPI. In this case the blob can be defined by its density (or light intensity) perturbation and also by its area or shape or motion, and the blob structure and trajectory in 2D can be directly measured for each separate event. In principle, this provides a better analysis of the speed, size, and birth rate than the 0D or 1D methods described above. A detailed analysis of the 2D structure of blobs in TORPEX showed, for example, that the radial speed was mostly independent of the blob size[199], and the theoretically-predicted mushroom shape of blobs was observed in 2D in VTF.[131] Under some assumptions the particle transport $\Gamma_r = < n V_r >$ can be estimated from such 2D data.[199,205,236]

More sophisticated statistical analysis techniques have been implemented to characterize the structure and motion of blobs. Wavelet analysis has been used to evaluate the blob size, lifetime, local intermittency measure, packing fraction, linear density of structures, and bicoherence in various devices.[22,126,144,150,152,164,171,177,178,180,189,191,218] Statistical analyses have searched for self-organized criticality or 'avalanche'-like behavior using techniques such as the

waiting time distribution, self-similarity, and Hurst exponents. [125,151,173,187,226,237] The fractal structure was investigated in HYBTOK-II, T-10, LHD, and NAGDIS-II,[178,238,239] and the singular value (or proper or biorthogonal) decomposition technique was used to identify blob structures.[97,177,227] The time dependence of the blob density signal at a single point has often been noted to be asymmetrical, with a sharp rise and a more gradual fall,[19,24,86,100,118,129,130,150,158,182] (e.g. see Fig. 17 in Sec. V.A), and the shapes of the density PDFs have been fit with various statistical models[66,156,162,182,187,190,200,201] (Sec. V.D).

The lifetime of blobs in CASTOR was shown to be longer than the 'eddy turnover' time associated with the local blob potential[165], but in W7-AS these lifetimes were comparable[119]. Thus it is not clear that blobs are always long-lived 'coherent structures' which retain their identity for times long compared with the local autocorrelation time.

In all these analyses described above, there is usually an implicit assumption that the blob structure is essentially 2D, so that the parallel flow along B is negligible, i.e. $f >> V_{||} / 2\pi L_{||}$, where $V_{||}$ is the parallel ion flow velocity, f is a characteristic turbulence frequency and $L_{||}$ is the parallel correlation length. If this were not the case then the structures observed at a given point along **B** could appear or disappear due to parallel flow rather than perpendicular $\mathbf{E}\times\mathbf{B}$ flow. However, this assumption is reasonable in most cases if the parallel correlation length of a blob is comparable to the size of the device, e.g. for $V_{||} \sim 10$ km/sec and $L_{||} \sim 100$ cm, then $f >> 2$ kHz. However, this should be checked on a case-by-case basis, and for each case there will be some characteristic blob frequency below which this assumption will be inappropriate.

E. Location and structure

In most fusion devices the skewness of the density PDF at the outer midplane (i.e. on the low-B-field side) increases with plasma radius into the SOL,[93,125,126,129,139,144,

[150,154,155,160,169] and a similar trend has been obtained to some extent in basic plasma devices.[200,202,215] Thus positive density blobs are usually dominant near the outer wall of these devices, and nearly absent inside the last closed flux surface where the skewness is usually close to zero. In some cases the skewness becomes negative farther toward the plasma center, e.g. in DIII-D,[129] ASDEX-U,[169] SINP,[174] HL-2A,[126] T-10,[159] and LAPD,[130] where negative skewness defines lower-than-average density 'holes' rather than blobs. In most cases these holes were observed to move radially inward[129,130,159] rather than radially outward.

The absolute amplitude of the blobs in DIII-D decayed rapidly with radius,[129] along with their electron temperature and radial velocity (see Fig. 13).[24] The background density and temperature also typically decrease rapidly with radius (e.g. see Fig. 9 in Ref. 129) leading to the characteristic increase of skewness with radius.

These trends are not too surprising given the theoretical picture of blob birth and outward propagation, as discussed in Secs. III and VII. From this picture we would expect that blobs are small, ill-defined and difficult to detect near where they are born, and relatively large and dominant in regions into which they convect, e.g. near the outer wall. If holes move inward, as expected from simple blob theory, then negative skewness should be dominant inside the blob birth zone. A more detailed discussion of blob generation in the edge plasma is given in Sec. VII.A.

In toroidal devices there is a strong asymmetry due to the magnetic curvature and resulting 1/R toroidal field. When the PDF of edge turbulence was measured as a function of poloidal angle in toroidal devices, the relative amplitude and skewness of the turbulence was highest on the outer midplane (i.e. low-field side), lower in the top/bottom and divertor regions, and lowest on the inner midplane (i.e. high-field side), e.g. in Alcator C-Mod,[21] JT-60U,[149,150] MAST,[161] and T-10.[160] This has been attributed to the stabilizing effect of magnetic curvature on the high-field ("good curvature") side (Sec. II.A). It is somewhat unclear whether blobs exist on the high-field side, and if they do,

whether they move inward or outward; this may depend on their connection to the low-field side blobs, as discussed in Sec. VI.A. It has been shown that blobs on the low-field side maintain their outward motion when the toroidal field direction is reversed,[18] as expected from the $\mathbf{E}\times\mathbf{B}$ drift model of blob theory.

There are relatively few experimental results describing the dependence of blobs on the shape of the edge magnetic geometry or on the presence of X-points in toroidal devices. In Alcator C-Mod the blob structure in the radial vs. poloidal plane followed the flux surface shape as mapped from the outer midplane, i.e. the blobs were radially extended near the X-point.[140] There have been measurements of positive skewness in turbulence at the divertor plates of tokamaks or stellarators by probes[150,161,182] and optical imaging.[136] Thus there is evidence to suggest that blobs extend many meters along B from the outer midplane to the divertor plate. There is some evidence that the presence of a divertor plate or limiter affects the blob structure or motion,[184,216] but so far an experiment in TORPEX has found no effect on the blob velocity as the angle of incidence of the magnetic field on the limiting structure is varied.[209]

In linear devices the effect of magnetic curvature is absent yet some characteristics of blobs seem to be at least qualitatively similar to toroidal devices.[12,130,222] In some cases rotating plasma columns may provide centrifugal forces that mimic magnetic curvature effects. Although blobs are seen in poloidally-symmetric linear devices, the introduction of a limiter into the plasma can also increase the intensity of blobs in its shadow.[130] A spiral structure of blob-like perturbations was observed in a rapidly rotating plasma in the Mistral linear device,[224,225] and large-scale potential structures in the 2D potential were observed in the Riso Q machine.[118,229] Blobs were shown to originate near the maximum density gradient region of VINETA, where they peeled-off from an m=1 drift wave and propagated radially at ~0.1 c_s,[219] and a similar result was obtained on CSDX.[222] Evidence for a periodic modulation of blobs (or 'avaloids') was observed in the SOL of PISCES,[223] which may also be related to a

periodic drift, interchange or rotational instability in the core plasma. Evidence for a radially extended streamer-like structure was observed in the Large Mirror Device Upgrade.[228]

Blobs in the toroidal device TORPEX originated from a coherent drift-interchange mode in which an increase of the local pressure gradient caused a radial elongation and subsequent breaking of the wave crests, in part due to $\mathbf{E}\times\mathbf{B}$ shearing.[132,202,204,206,207] After their formation, the blobs propagated radially and were the dominant radial transport mechanism on the low-B field side of the device.[205] A k-space analysis of blob dynamics in TORPEX showed that their energy is supplied by the local shear flow in some cases.[203] Blobs in the torsatron TJ-K were generated near the separatrix between closed and open field lines, where drift-wave turbulence in the closed region begins to be affected by the shear flow generated by the presence of the limiter in the SOL.[184] The effect of sheared flow on the blob birth zone is discussed in Sec. VII .A.

The blobs in almost all the experiments of Tables II and III have been self-generated by the plasma without any direct external drive or control. An exception is VTF, in which blobs were created on the high-field side of a simple torus using pulsed ECH heating.[131] This allowed the radial motion and shape evolution of the blobs to be measured with relatively good accuracy and reproducibility, as shown in Fig. 9. Somewhat similar localized blob-like temperature filaments have been created in the linear plasma device LAPD.[217] Such external control of blobs has not been possible in fusion devices, mainly due to the large energy and particle flux already existing in normal conditions in these devices.

Relatively few measurements have been made of the parallel structure of blobs along B; so, for example, it is not yet clear whether blobs are initially created at the outer midplane of toroidal devices, or simultaneously all along **B**. The parallel correlation of edge turbulence as a whole was recently measured in TJ-K,[240] NSTX,[136] Alcator C-Mod,[141] and in several previous experiments,[1] and the correlation lengths were typically

many meters along the magnetic field and only a few cm across **B**; however, these measurements did not clearly distinguish the correlation of large-amplitude blobs from that due to background (i.e. Gaussian PDF) turbulence, so the parallel correlation length of blobs remains somewhat uncertain. Passive optical imaging of the 3-D structure of blobs has been done in MAST,[33,163] but it is not clear that the observed structures are aligned exactly along **B**.

F. Potential and magnetic field

Up to now this experimental overview has focused on the density perturbation as the defining characteristic of blobs, but there have also been many measurements of other plasma properties of blobs. This section reviews those measurements, some of which are important for comparing experiment with theory in later sections.

The electrostatic potential perturbation and poloidal electric fields associated with blobs have been measured using the floating potential of Langmuir probes in DIII-D,[18] C-Mod,[138] JET,[144] TEXTOR,[125] JT-60,[150] CASTOR,[167] RFX-mod[188,189,192,193] T2R[188] and TPE-RX.[197] Both positive and negative blob potentials have been observed, corresponding to positive and negative vortices, along with both monopolar and dipolar potential structures. Two dimensional spatial maps of the vortex-like potential structure of blobs have been made in W7-AS,[119] ADITYA,[172] SINP,[174] TORPEX,[132,204] TJ-K,[184] the Riso Q machine,[226] and THORELLO.[215] The relationship between the observed monopole and/or dipole potential structures and the theory of blobs is discussed in Sec. V.A.

Magnetic field perturbations were correlated with the blob size in the reversed-field pinch RFX-mod,[191] and a direct measurement of the magnetic field and parallel current density associated with blobs was recently made in that device.[192,193] The pressure peak of the blob was associated with a current filament aligned along B and

moving with the $\mathbf{E}\times\mathbf{B}$ flow. Somewhat similar results were obtained on the MST field-reversed pinch.[241]

G. Scalings

The comparisons between experiment and theory in Sec. VI focus on the scaling of various blob properties with plasma parameters such as the collisionality or relative size of the gyroradius to plasma size. Ideally these scalings would be consistent across all devices, but such universal trends are not yet clear from the existing experimental database.

Perhaps the most studied property of blobs is their radial velocity, which is an important parameter in analytic theory and blob-induced radial transport. Figure 12 shows published data on blob size vs. speed for nine tokamaks from Table II. This plot gives an overview of the existing tokamak data without any attempt to distinguish between different definitions of a blob or different analysis procedures. It is clear from Fig. 12 that there is a wide variation in blob size vs. radial speed and that there is no simple relationship between these two quantities. Part of this variation is due to differing definitions of a blob and different analysis techniques; for example, the initial analysis of NSTX GPI data showed individual blob velocities which were sometimes inward,[134] while a later analysis (with a more restrictive definition of a blob) showed only outward radial velocities.[135] A discussion of the comparison of some of these results with theory and simulation is given in Secs. V and VI.

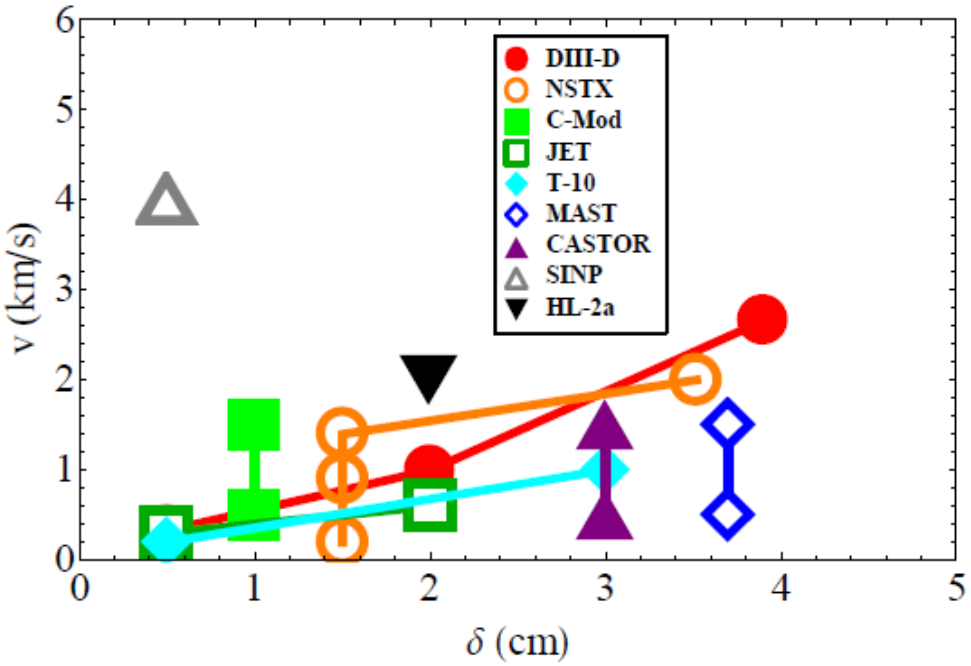

Fig. 12 (color online) Outward radial blob speed v in km/s vs. blob size δ in cm for tokamaks, as reported in the literature from Table II. No attempt has been made to make the definitions and analysis of blobs the same for all experiments. The blob data was taken from the following references: DIII-D,[18] NSTX,[135] C-Mod,[138] JET,[144] T-10,[160] MAST,[163] CASTOR,[167] SINP,[175] HL-2a.[126]

The variation of blob parameters with plasma density and current for DIII-D is shown in Fig. 13.[24] Here, conditional averaging of reciprocating probe data was used to obtain the radial profiles of the blob peak density, temperature, and radial velocity in the SOL (the radial velocity was determined from the poloidal electric field). Four values of the Greenwald fraction $f_{GW} \equiv \bar{n}/n_G$ and two values of plasma current I_p are compared at constant B field. Here $n_G \equiv I_p(\mathrm{MA})/[\pi\, a(\mathrm{m})^2]$ denotes the Greenwald density limit[26] in units of 10^{20} m^{-3}, and a(m) denotes the minor radius in meters. The peak blob density and temperature fall monotonically with radius in the SOL for all cases, presumably due to parallel transport of particles and heat to the walls and divertor plates (the yellow

region is the "limiter SOL" and the blue region is the "outer wall shadow"). The blob peak density increases with the discharge density, but neither the blob temperature nor the radial velocity shows a clear dependence on the discharge density.

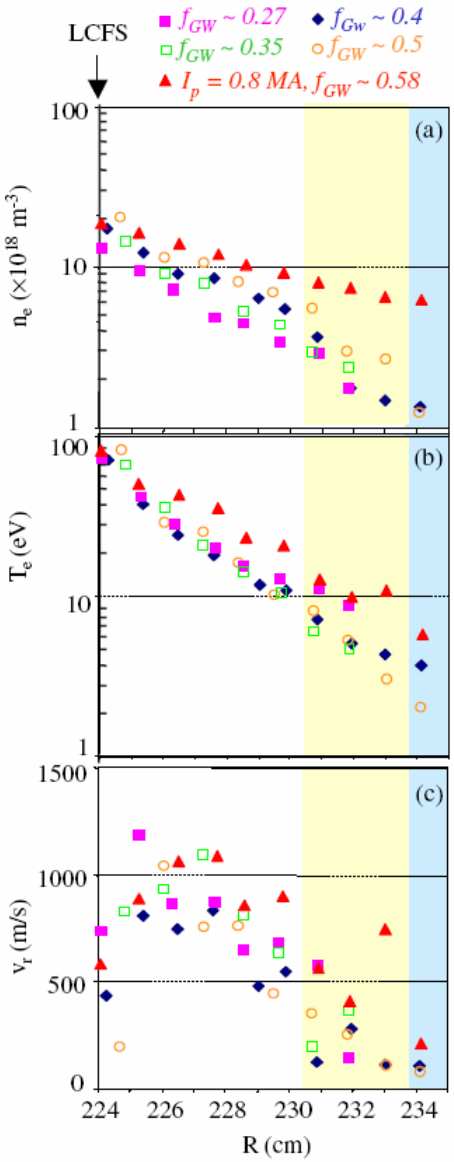

Fig. 13 (color online) Radial profiles of the density, electron temperature and radial velocity of blobs in the DIII-D SOL, inferred from a conditional averaging analysis of reciprocating probe data. Four values of Greenwald fraction and two values of the plasma current are compared. (I_p = 0.8 MA for the red triangles and I_p = 1.0 MA for the other data.) Reprinted from Ref. 24 with permission from the International Atomic Energy Agency.

The collisionality (or density) dependence of blobs has been studied in TCV,[93] where the skewness of the density PDF in the SOL of TCV was independent of the local average density, although the magnitude of the turbulent transport increased with collisionality.[52] The blob's relative contribution to the local density was constant as a function of radius and plasma density in DIII-D.[129] The fraction of turbulent radial particle transport from blobs was found to be ~ 50% for all radii measured in the SOL of in DIII-D,[18] TEXTOR,[125] HL-2A,[126] MAST,[127] among other devices. The collisionality dependence of blob transport is discussed further in Sec. VI.C.

An increase in blob transport with increasing edge safety factor $q(r=a) \equiv aB/(RB_\theta)$ was reported in TEXTOR,[146] and longer blob duration and larger skewness was observed near the X-point divertor detachment in JT-60U.[149] The number of blobs increases above a density 0.3 n_G in T-10,[158] while the radial blob speed peaked at about 0.4 n_G and the blob size increased with density up to 0.7 n_G in MAST.[127]

Blobs in DIII-D were highly reduced in amplitude in H-mode plasmas compared with L-mode plasmas, but still contributed ~50% to the radial particle transport in both cases.[18] Blobs in NSTX also appeared less frequently in H-mode plasmas than L-mode plasmas, but they have a similar amplitude in L-mode and H-mode, and increase in frequency with increased NBI power in H-mode.[136] The statistical properties of edge turbulence including the density PDF were similar in H-mode and L-mode in ASDEX-U.[168]

An inverse scaling of blob speed with background gas pressure was observed in VTF and was explained in terms of the drag force due to ion-neutral collisions,[131] and ion-neutral collisions also became the dominant damping term for blob velocity in some conditions in TORPEX.[208] Blobby transport was observed to increase under detached plasma conditions in the linear NAGDIS-II divertor simulator.[227] Variation of the ion mass in TORPEX allowed a study of the scaling of blob size with radial speed,[208] which is discussed further in Sec. VI.B (see Fig. 26). The blob radial scale length was related to

the local electron pressure gradient scale length in RFX-Mod,[191] suggesting the pressure gradient as a potential source for the blob generation (also see Ref. 204).

There have been relatively few methods of external control over the process of blob formation within edge turbulence. A reduction of blob size and radial velocity within the ergodic layer of the Dynamic Ergodic Divertor in TEXTOR,[145-147] and a rotating helical magnetic field had a frequency-selective effect on blobs in HYBTOK-II.[176] A reduction in the number of blobs was observed during electrode biasing in TJ-II[186] and CASTOR.[242]

H. Comparisons of different devices

Comparative studies of blobs in various fusion and basic plasma devices have been attempted in the papers cited in Table IV. This work includes the use of advanced analysis techniques such as multifractals and biorthogonal decomposition (BD) and attempts to relate blob physics to the paradigm of Self Organized Criticality (SOC). The normalized shapes of the density PDF often appear to be similar in different devices,[66,243] but this cannot be a 'universal' property of blobs since the shapes of the PDF also vary systematically with radius. It would be more correct to say that the PDF of density *in the far SOL* can be nearly invariant over a wide range of parameters when suitably normalized (see Sec. V.C). An interesting parabolic relationship between the skewness and kurtosis of the PDFs was found in various devices,[66,200,201,244] which has been interpreted theoretically,[64] as discussed in Sec. V.D. Other attempts have been made to find more subtle statistical regularities of blobs, e.g. their fractal dimensionality.[239] An attempt to compare the blob size and speed for various devices produced a wide scatter,[5] similar to Fig. 12 here. (We will see in Fig. 27 that this scatter persists, even when physically meaningful dimensionless quantities are compared across devices.)

In general, blobs are not quite the same in fusion devices and basic plasma devices. Blobs usually have a relatively large size-scale in basic plasma devices (≥ 0.1

times the plasma radius), while in fusion devices the blobs are always an edge or SOL phenomenon with a size-scale ≤ 0.1 times the plasma radius. The creation of blobs in basic fusion devices is often linked to wave-like interchange or drift instabilities,[210,211] whereas in fusion devices the blobs appear to be created by turbulence. Radial transport is not dominated by blobs in linear open-field line devices, as it is in toroidal fusion devices, since the parallel losses are so large. Radial blob transport is still a small fraction of the total transport at the edge of simple helical devices, e.g. TORPEX.[205] The fundamental polarization processes for blobs are clearly different in linear devices without curvature, helical devices without closed field lines, and fusion devices with closed field lines. (They can all be treated theoretically by introducing an effective gravity $\mathbf{g}$, as discussed in Sec. III, but the detailed scaling of $\mathbf{g}$ is different in each case.). Ion-neutral collisions can be a dominant factor in the blob dynamics in low temperature basic plasma devices[131,208] but it is not known whether this affects blobs in fusion devices. Therefore it is unlikely that there is a single theoretical model (i.e. a single scaling law) which can explain the blob properties in all the devices of Tables II and III. The existence of multiple theoretical scaling laws for blob velocity is discussed in Sec. VI.

Table IV: Comparative studies of blobs properties in different devices

Devices compared	*topic of comparison*	*Reference*
TEDDI, KIWI, W7-AS, MIRABELLE	large scale structure	214
TORPEX and CSDX	blob formation	207
Alcator C-Mod, MAST, PISCES, Tore-Supra	PDF	66,243
T-10, HYBTOK-II, LHD, and NAGDIS-II	multifractals	238,239
TJ-1, JET, TJ-1U,W7-AS, ATF	SOC	245
ADITYA and ASDEX	BD analysis	97
CASTOR and Tore-Supra	blob time bursts	242
RFX-mod, TPE_RX, NSTX, Alcator C-Mod	GPI statistics	244
C-Mod, T-10,DIII-D,NSTX,MAST,PISCES, LAPD	blob speed vs. size	5
NSTX,VINETA,CSDX, CASTOR,TEDDI, TORPEX	coherent structures	246

I. Summary of experimental overview

Experiments in over 40 toroidal magnetic fusion and basic plasma devices have measured the presence of large, intermittent positive density perturbations called 'blobs', most commonly in the edge regions of these plasmas. These blobs generally move outward toward the wall of these devices and carry plasma particles and heat with them. In fusion devices this process contributes an order unity fraction of the particle transport in the far scrape-off layer, and so can be a significant factor in the design of a magnetic fusion reactor.

In most of these devices there is a broad and continuous distribution of blob sizes, shapes, and speeds, as seen in the ubiquitous positively-skewed, non-Gaussian tail of the PDF of density measured at a single point. This broad distribution has made a precise definition of a blob difficult, and so the distinction between blobs and 'background

turbulence' has been somewhat arbitrary. Although each individual blob is subject to the same forces and fields described in Sec. II, the ensemble of blobs in a real device is best described statistically rather than deterministically, due to the complex nonlinear interactions between the blobs and the background plasma and among the blobs themselves.

Given this experimental situation, comparisons of blob experiments with theory are most easily done within a single device, preferably using the same definitions and analysis techniques for both experiment and theory. These comparisons should be considered as qualitative unless the uncertainties in both the experiments and the theories are examined explicitly. It is clear from this experimental overview that the description of blob dynamics in existing devices is still incomplete, and a quantitative and/or predictive understanding of blob structure, motion, and transport is a challenging task..

V. Blob structure and intermittency

Having surveyed the theoretical picture of blobs in Secs. II and III, and the experimental picture of blobs in Sec. IV, we turn now to the comparison of the experimental data with theoretical and simulation results. We begin with some fundamental aspects of blobs: their internal structure and their statistical description. Most of the experimental work on blobs has been devoted to these topics.

A. Density and potential structure and pulse shape

Blob theory, and computer simulations of seeded blobs, predict a characteristic blob structure in time and space. The characteristic blob structure in the x-y plane (perpendicular to **B**), and the characteristic pulse shape in radius (or time, for a stationary observer such as a probe), can be compared with experimental data, as discussed in this section.

In order to understand this structure, we need to extend the theory to include the effect of a background density. By assumption, a blob has a *monopole* poloidal distribution of density, usually taken to be a Gaussian distribution $\delta n(y)$, superimposed on a constant background density n_b. The charge polarization process results in a *dipole* distribution of charge, vorticity and potential (see Fig. 1). In a toroidal device, the driving term for the charge polarization in Eq. (1) has the form $\mathbf{b}\cdot\nabla\times\mathbf{F} \sim -(\kappa/n)\nabla_y P$, where n is the density, P = nT is the pressure, $\kappa \sim 1/R_c$ is the curvature, and y is the binormal coordinate (approximately poloidal in a tokamak). In either the sheath-connected regime (where $J_{||} = ne^2 c_s \Phi / T_e$) or the inertial regime (where the left-hand-side of Eq. (1) dominates $J_{||}$) the density dependence of the sheath or inertial terms ensures that the potential Φ is a function of $(\kappa/n)\nabla_y P$. In the constant temperature limit, this curvature drive term scales as $(\kappa T/n)\,(dn/dy) \sim (\kappa T/\delta_b)(\delta n/n)$ where $n = n_b + \delta n$ and δ_b is the poloidal blob size. Because the dependence on the density profile is of the form $(n_b+\delta n)^{-1}\, d(\delta n)/dy$, the presence of a constant background density n_b reduces the drive for the blob velocity and alters the structure $\delta n(x, y)$ of the blob.

This interaction with the background density has been studied in simulations of seeded blobs propagating across a constant background density[37,41,49,57,67] and the effect of a background density gradient has also been considered.[247] As shown in Fig. 14 for the case of constant background density, the monopole density and dipole potential pattern predicted by simple theory[3,15,16] is obtained in this simulation. The interaction of the blob with the background density produces a sheared flow pattern (weaker force, and thus weaker flow, at large |y|), which leads to the formation of a steep leading edge and trailing wake. The sheared flow pattern shown in Fig. 14 also affects the blob stability (Sec. VI.E).

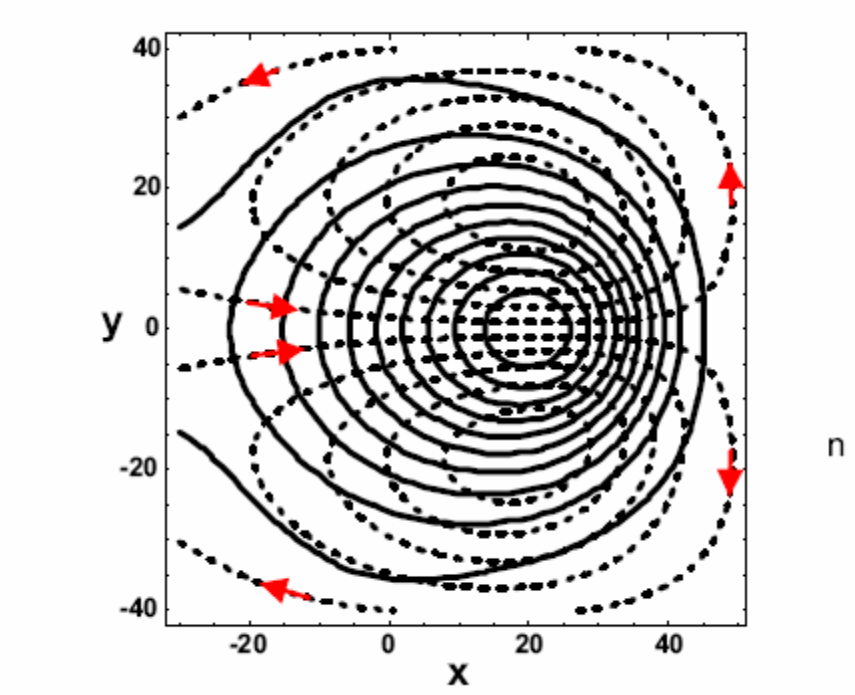

Fig. 14 Seeded blob simulation results: contours of density (solid) and potential (dashed) in the lab frame for an isolated blob propagating through a constant background density equal to half the peak blob density. The dashed lines are also the streamlines of the $\mathbf{E}\times\mathbf{B}$ flow, with the direction indicated by the arrow. Note the characteristic pattern of monopole density and dipole potential. The interaction with the background density produces the sheared flow pattern, which in turn gives a characteristic pulse shape in time. A probe located at the symmetry plane (y = 0) sees a steep leading edge and long trailing wake. Reprinted from Ref. 38 with permission from Wiley-VCH.

Experimentally, the existence of coherent propagating objects with a dipole potential structure has been verified using probe arrays in a wide variety of plasma devices including linear machines,[130] stellarators,[119] tokamaks,[138,167] reversed-field pinches[197] and other small toroidal machines.[131] An example of a another kind of measurement of the blob density and potential structure on C-Mod[138] is shown in

Fig. 15. Here, two diagnostics are used to calculate the correlation functions. The D_α fluctuations of a GPI imaging system provides a reference signal, assumed to be proportional to $\tilde{n}$, and the time-series of $(\tilde{n},\tilde{\Phi})$ is obtained from a reciprocating Langmuir probe moving through the same flux tube viewed by the GPI system so that both diagnostics sample the same field-aligned structure. The correlations between diode and probe signals $C(\tilde{n},\tilde{n})$ and $C(\tilde{n},\tilde{\Phi})$ are plotted in Fig. 15. Thus, the predictions of the blob model are confirmed: the density has a single peak and the potential has a dipole structure (positive and negative peaks displaced poloidally around the density maximum).

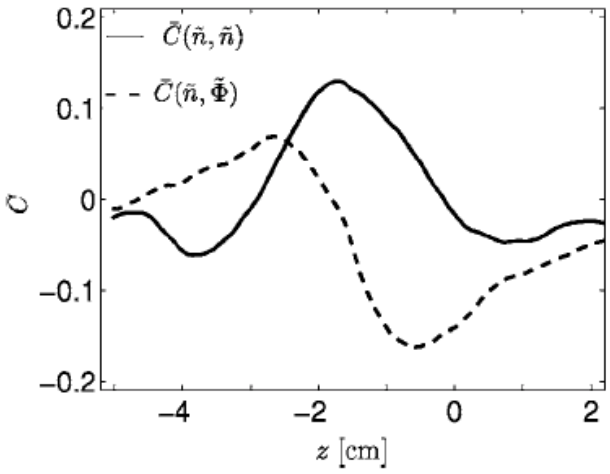

Fig. 15 Experimental measurement of the monopole density structure and dipole potential structure of a blob on C-Mod as a function of the vertical probe position z (cm) in the SOL, based on the correlation between the probe and the GPI diagnostic. The solid line shows the density correlation amplitudes $C(\tilde{n},\tilde{n})$ and the dashed line shows the potential correlation amplitude $C(\tilde{n},\tilde{\Phi})$, averaged over the correlation time lag interval τ = [-25 μs, 50μs]. Reprinted from Ref. 138 with permission from the American Institute of Physics.

Seeded blob simulations of blobs propagating on top of a small background density predict a characteristic pulse shape. An example of the typical radial blob pulse

shape on the symmetry plane (y = 0) at a fixed instant of time is shown in Fig. 16. Note that the blob has a steep leading edge and gentle trailing wake.

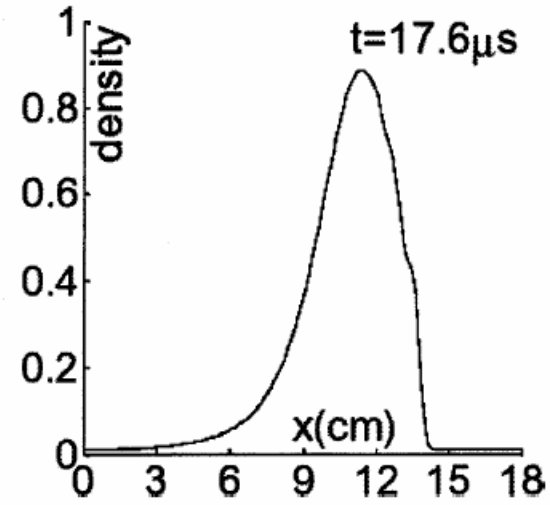

Fig. 16 Simulation of blob pulse shape showing the steepening of the density profile in the direction of propagation for a large blob, $\delta_x = \delta_y = 1.8\ \mathrm{cm} \approx \delta_*$, where δ_* is the most stable blob size defined in Eq. (8) and discussed in Sec. VI.E. The ratio of blob to background density is 100 in this simulation. Reprinted from Ref. 37 with permission from the American Institute of Physics.

Blob pulse shapes qualitatively similar to those of the simulation are obtained experimentally by "conditional averaging"[19,118,119] of Langmuir probe data. In this analysis, only peaks above some threshold are retained (typically greater than 2.5 standard deviations above the average); the peaks are aligned in time and averaged over all events. This procedure averages out the turbulent fluctuations and averages over different impact parameters between the blobs and the probe. The result is a plot of the average blob pulse shape in time. An example is shown in Fig. 17 for a fixed radial position in the far SOL in TCV. The figure shows that the shape is similar for a wide range of line-averaged densities on this tokamak.[4,52,93] Note the steep rise and slow

decay of the signal in time, which is qualitatively consistent with the simulated blob shape shown in Fig. 16. The exact shape depends on the ratio of the blob density to that of the background plasma. Also, note that Fig. 17 shows the result of conditionally averaging the data from an ESEL 2D turbulence simulation in the inertial regime (gray solid curve), which corresponds to the high-density limit (red solid curve); the pulse shapes obtained from the simulation and from the experimental data show good agreement.

The pulse shape shown in Figs. 16 and 17 is an important signature of blob transport and has been seen in a number of experiments, including tokamaks,[19,24,86,100,125, 129,150,158] stellarators[182] and linear machines.[118,130]

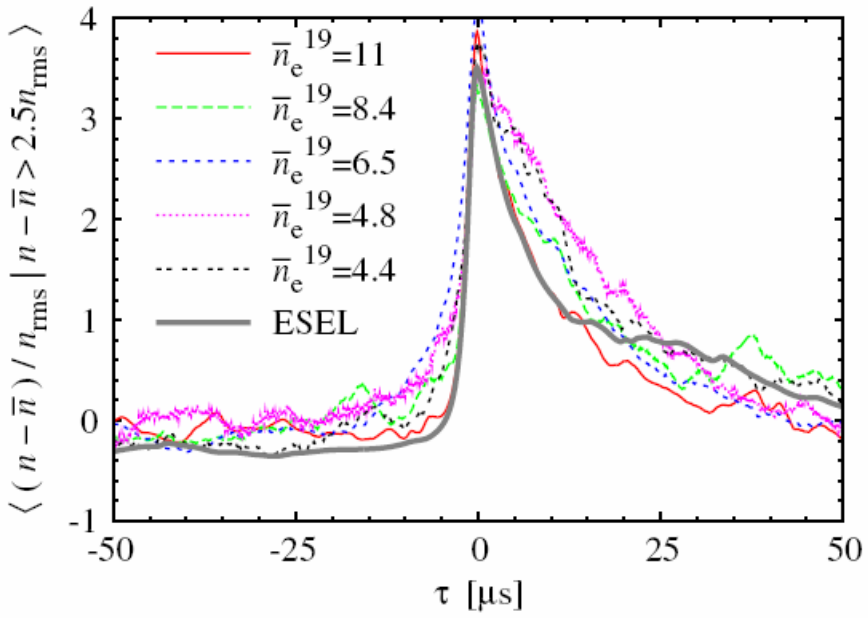

Fig. 17 (color online) Experimental results on blob pulse shape: conditionally-averaged particle density fluctuations at the wall radius in the TCV tokamak for scans in line-averaged core plasma density $\bar{n}_e$ at fixed magnetic field and plasma current. The density $\bar{n}_e$ is given in units of 10^{19} m−3. Reprinted from Ref. 93 with permission from the International Atomic Energy Agency.

In summary, the blob characteristics discussed in this section (monopole-dipole structure, steep leading edge and gentle trailing wake) are routinely observed in edge turbulence simulations of blobs propagating through a low-density background[37,40,41,49,57] and have been observed in a variety of experiments. This is an important area of agreement between analytic theory, simulation and experiment.

B. Skewness and Kurtosis

Another important area for comparison between blob simulations and experiments is their statistical description, a topic introduced in Sec. III.B. As shown in Fig. 3, blobs (holes) contribute large positive (negative) bursts to the time series of the particle density fluctuations about its mean value, and this gives a positive (negative) contribution to the skewness of the PDF. The radial skewness profile tends to be negative in the edge plasma where holes dominate, zero in the blob birth zone (where blobs and holes are formed in equal numbers) and positive in the SOL where the blobs dominate the statistics (typically $S > 1$ in the far SOL). The existence of large skewness for fluctuations in the far SOL is observed in simulations,[53,59,61,93,100] experiments on tokamaks[93,100,126,129,144,169] and experiments on a variety of other machines.[182,197,201,202,229]

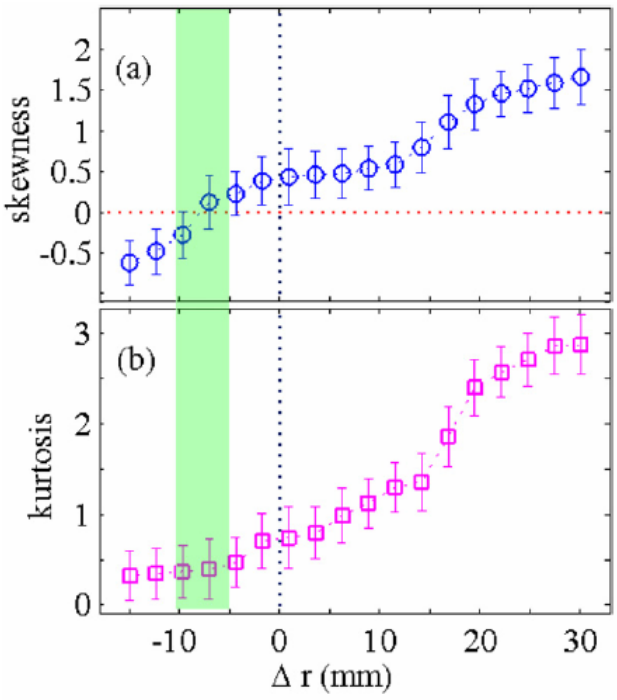

Fig. 18 (color online) Radial profiles of skewness (S) and kurtosis (K) of the PDF of density fluctuations on the HL-2A tokamak. The error bars give the standard deviation from the mean, averaged over ten discharges. The vertical dotted line denotes the position of the LCFS with an error of ±5 mm. Note that the skewness changes sign in the shaded region. Reprinted from Ref. 126 with permission from the Institute of Physics.

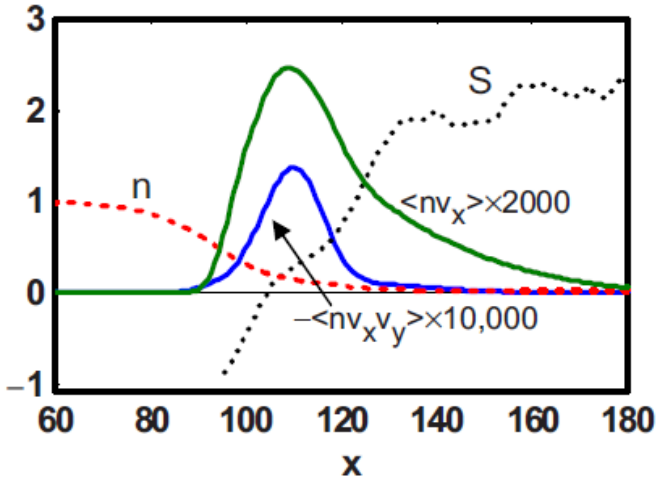

Fig. 19 (color online) Radial profiles of mean density n, skewness (S), particle flux $\Gamma = \langle nv_x \rangle$ and momentum flux $\langle nv_x v_y \rangle$ from a simulation of turbulent blob transport with the 2D SOLT turbulence code. Reprinted from Ref. 31 with permission from the American Institute of Physics.

An example of an experimental measurement of the radial skewness and kurtosis profiles is shown in Fig. 18. Here, S(x) and K(x) are plotted for density fluctuation data on the HL-2A tokamak. Note the qualitative agreement between this small-tokamak data and the JET data in Fig. 3. In both cases, the data supports the physical picture of holes (negative density fluctuations) inside a critical radius called the "blob birth zone" and blobs (positive density fluctuations) dominating the statistics outside that radius. Theoretical considerations, confirmed by simulations, predict that the blob birth zone is located near S = 0 (see Sec. VII), which is supported by the data in Fig. 18. A similar plot of S(x) using reciprocating probe data on NSTX was shown in Ref. 248. This is an important point of qualitative agreement between theory and experiment. Finally, note that the kurtosis is large in the far SOL (K > 1) and increases with radius. The relation of K and S will be discussed further in Sec. V.D.

While the qualitative features of S(x) are intuitive from the above arguments on blob and hole formation, the exact spatial structure of S(x) is difficult to calculate analytically. Simulations enable a more quantitative verification of the processes. An example from Ref. 31 is shown in Fig. 19, where again the simulation model is only slightly more complicated than Eqs. (1) and (2), but importantly defines particle source and sink regions to maintain a localized birth zone near the maximum of the logarithmic density (pressure) gradient. Note also that the zero of S(x) is near the radial maximum of the particle flux, further demarcating the blob birth zone. (The role of the momentum flux will be considered in Sec. VIII.A.) Other similar results may be found in the literature, and in some cases comparisons of simulated S(x) with experimental data have been made and show good agreement. [93,129]

C. Probability distribution function

Another way of characterizing the intermittency is to plot the probability distribution function (PDF). Let $P_X(x)$ denote the probability that a fluctuating quantity X lies between x and x + dx. It is useful to plot a version of the PDF in which the fluctuations are normalized to the mean. One defines the normalized form $\overline{P}_X(y)$ by

$$\overline{P}_X(y) = \sigma_X \; P_X(x) \tag{5}$$

where $y = (x - \overline{X})/\sigma_X$. As discussed in Ref. 2, the normalized PDFs $\overline{P}_X(y)$ for turbulence in the far SOL tend to be non-Gaussian and independent of the specific plasma conditions in a given machine.[4,243,249] However, the PDF does depend on the radial location, varying from Gaussian near the LCFS to highly skewed near the wall (e.g. see Fig. 3 of Ref. 142 and Fig. 3 of Ref. 126). This variation of the PDF shape causes a radially increasing skewness profile S(x), as shown in Fig. 18.

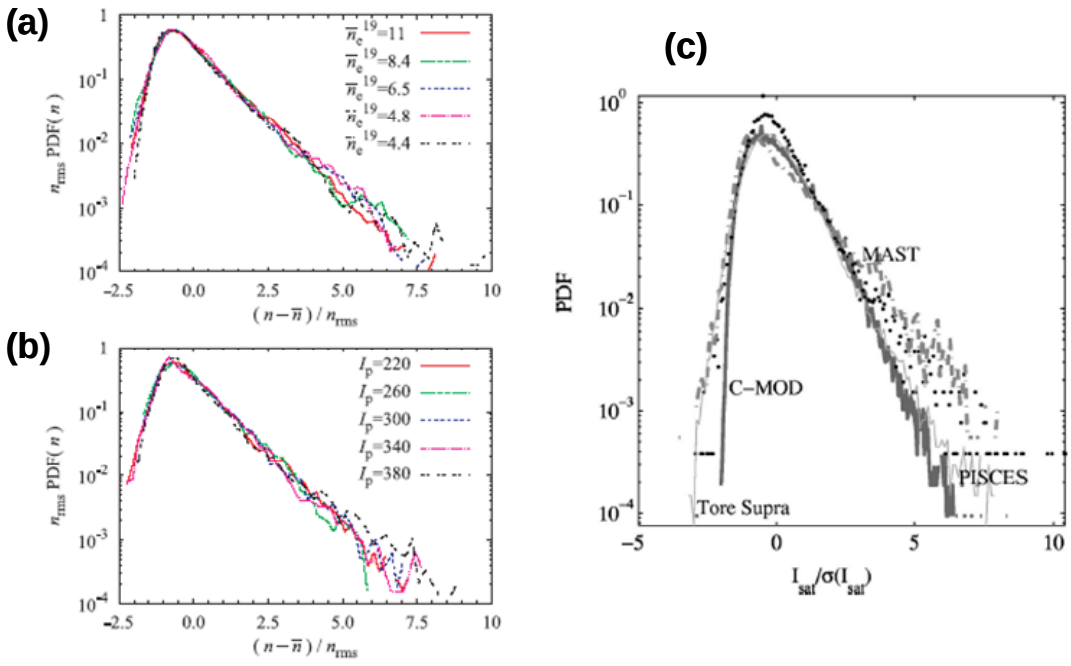

Fig. 20 (color online) Rescaled probability distribution functions for density fluctuations in the far SOL in the TCV tokamak for scans in (a) line-averaged density and (b) plasma current. Shown in (c) is a superposition of the PDF of the ion saturation current in four machines: Tore Supra, Alcator C-Mod, MAST and PISCES. The ion saturation current was normalized to its standard deviation, and the integral of each PDF was set equal to 1. Figures (a) and (b) are reprinted from Ref. 4 with permission from the Japan Society of Plasma Science and Nuclear Fusion Research (JSPF); figure (c) is reprinted from Ref. 243 with permission from the American Institute of Physics.

If a region exists in the far SOL where blob propagation is purely ballistic, then the PDFs may be expected to be roughly independent of position with properties that relate back to their production. Figure 20 illustrates the behavior of the PDF of fluctuations in the far SOL. It is remarkable (and unexpected from the preceding discussion) that these PDFs tend to show a "universal" character, independent not only of position in the far SOL, but also apparently independent of machine and parameters. The data in Figs. 20(a) and (b) were taken on a field line in the far SOL that maps from the probe position to the wall at the midplane in TCV. The data in Fig. 20(c) was taken at

different radii on the four machines but far enough into the SOL that the turbulence is bursty (intermittent). The PDFs are rescaled as in Eq. (5), with the signals normalized to their standard deviations, and in part (c) the PDFs are normalized so that the integral under each curve is equal to 1.

This figure illustrates the sense in which the blobby turbulence is "invariant" across different parameters and even different machines. Figures 20(a) and (b) show that the normalized PDF of density fluctuations in the far SOL of TCV is strikingly similar over a wide range of parameters.[4] The PDF is independent of both the line-averaged density [Fig. 20(a)] and the plasma current [Fig. 20(b)] on TCV.[4] Similar independence of the normalized PDF from parameters was observed in the computer simulations reported in Ref. 53, where both the magnetic geometry and the plasma resistivity were varied. Second, Fig. 20(c) shows that similar PDFs of ion saturation current are obtained in four very different plasma devices: two tokamaks (Tore Supra, Alcator C-Mod), the spherical torus MAST, and the linear device PISCES. However, it should also be noted that despite this similarity, the underlying physical forces driving the motion, and current closures determining the blob speed, vary significantly in the different plasma devices.

The characteristics of the PDF described in this section are commonly observed in fluctuations of the ion saturation current, density or particle flux in the far SOL when blobs are dominant. Each PDF has a positive tail indicating the contribution of propagating large-amplitude structures. This behavior has been observed in many plasma devices.[12,22,93,100,102,125,130,135,146,156,182,201,223]

Skewed PDFs of the type shown in Fig. 20 are just as ubiquitous in edge and SOL simulations as they are in experiments. An example is shown in Fig. 21, which is a companion figure to Fig. 4. The structure of the PDF depends on the quantity being characterized; thus, the flux PDF is not directly comparable to the density PDF. Generally, when comparing lower-order quantities with higher-order nonlinear products (e.g. n vs nv_x), one finds that the higher-order products exhibit more pronounced PDF

tails. In particular, the flux PDF will generally be non-Gaussian, even if the density and velocity PDFs are Gaussian. Furthermore, because the density and velocity fluctuations are typically correlated, the resulting non-Gaussian PDF will be skewed.[250] For this reason, tails in the flux PDF are consistent with, but not a proof of, blob activity. The characteristics of PDF tails in various edge turbulence models, and some of the subtleties in their interpretation, are discussed further in Ref. 251.

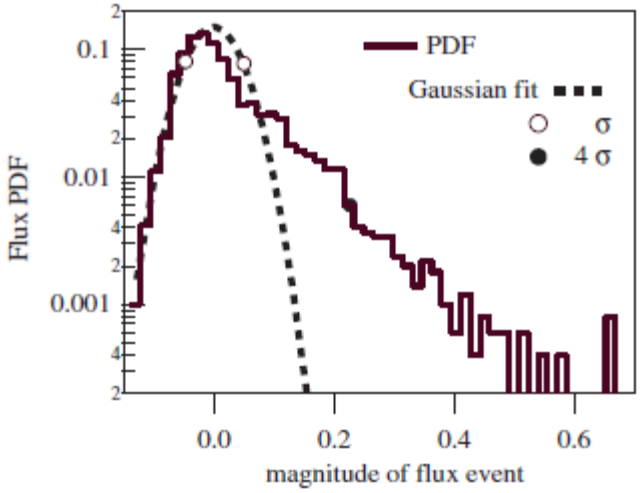

Fig. 21 (color online) PDF of the particle flux for the same turbulence simulation as in Fig 4. Also shown is the deviation from Gaussian statistics. Reprinted from Ref. 79 with permission from the International Atomic Energy Agency.

Finally, note that the normalization of the PDF must be "undone" to obtain the expected values of dimensional quantities such as the density or the particle flux. Thus, even when the normalized PDFs display similar statistics (as in Fig. 20), the level of the saturated turbulence, and the time-averaged values of the SOL density and radial particle flux, change significantly with experimental control parameters (density, plasma current, etc.), e.g. see Figs. 3 and 10 in Ref. 93 and Fig. 4 of Ref. 53.

D. Statistical theories

In previous sections, we have presented several examples from both simulation and experiment of PDFs with non-Gaussian extended tails which exhibit significant skewness. Indeed this feature is rather generic and is an expected consequence of intermittent blob activity. The key question is what physics (and characteristics of the simulation models) gives rise to these features, and what insights can be gained from them about the underlying nonlinear dynamics.

A possible clue that has been explored in several papers is the relationship between skewness $S = \left\langle \tilde{\xi}^3 \right\rangle / \sigma_\xi^3$ and kurtosis $K = \left\langle \tilde{\xi}^4 \right\rangle / \sigma_\xi^4 - 3$ for a quantity ξ with fluctuation level $\sigma_\xi^2 = \left\langle \tilde{\xi}^2 \right\rangle$. (Here $\langle Q \rangle \equiv \overline{Q}$ denotes the average of Q over the data set and the fluctuation about the mean is given by $\tilde{Q} = Q - \overline{Q}$.) In Ref. 156 it was shown that a gamma distributed random variable characterized the PDF of density fluctuations in the SOL for L-mode data on the TCV tokamak under a wide variety of conditions. A calculation of the higher moments yielded a parabolic relation between K and S, viz. $K = 1.5\, S^2 + 3$. In Refs. 200 and 201, TORPEX probe data containing both drift-interchange turbulence and blobs was shown to exhibit a similar unique parabolic relationship between K and S over many thousands of shots and a wide variety of experimental conditions, viz. $K \sim 1.5\, S^2 + 2.8$. It was noted that similar parabolic relations for S and K hold for a wide variety of physical systems. It was also pointed out in Ref. 200 that the gamma distribution used in Ref. 156 does not allow negative values of skewness, but can be generalized to a beta distribution which allows $S < 0$. In either case, the parabolic K-S relation is obtained. Similar experimental studies on other machines using GPI data were reported in Ref. 244. Data was found to align along parabolic curves, but different best-fit parameters were obtained, depending on both the machine and operating conditions (in particular, L and H mode in NSTX). A linear term is the K-S parabolic relation was also needed in general.

The similarity between TORPEX data and studies of sea-surface temperature fluctuations was noted in Ref. 64 where a Langevin-type model (originally developed for the sea-surface work) was adapted to include linear finite frequency modes. This model was able to yield an analytical result $K = a\,S^2 + b$ where a and b depend on the frequency and forcing strength, with maximum values of S and K limited by the frequency parameter in the model. A somewhat different approach was taken in Ref. 66. This model combines a Gaussian random variable with its square (to model quadratic nonlinearities) and results in a analytical description of S and K which depends on a single nonlinear coupling parameter. The result $K = 1.5\ S^2$ emerges in the strongly nonlinear limit. Furthermore, for quadratic nonlinearities, the theory predicts maximum values $S_{max} = 2.83$ and $K_{max} = 16$, similar to those observed in blob turbulence simulations and experiments. The success of these rather simple (compared to plasma turbulence) theoretical models helps to explain the generic nature of the experimental observations. However, as a result of this simplicity, it seem unlikely that information on blob-specific dynamics can be deduced from S and K alone. A similar conclusion was reached in Ref. 252.

In addition to the K-S studies, a theoretical statistical approach to intermittency in turbulence has been advanced by examining the structure of the PDF tails using the instanton method.[63,253] It was shown that the PDF tails scale as $P(\xi) \sim \exp(-C\xi^s)$ where C is a constant, $s = (n+1)/m$, n is the order of nonlinear interaction ($n = 2$ for quadratic nonlinearities), and m is the order of the quantity ξ (where $m = 1$ for density n_e, $m = 2$ for Reynolds stress $v_x v_y$, etc). Present theories only take into account the highest order nonlinear term, which is the one that asymptotically dominates the PDF tails. Qualitative similarities with simulations and experiments were noted in these papers.

As this brief section is meant to indicate, statistical theories of intermittent turbulence are very difficult, and typically have a rather loose connection to the details of

the underlying dynamical equations that lead to blob formation. Nevertheless, interesting correspondences with some aspects of experimental data have been achieved.

Numerical simulations, which include both turbulence and the blob structures generated by that turbulence, show many of the characteristics discussed here, viz. non-Gaussian statistics that produces bursty signals like that of Fig. 3 with skewed PDFs and radial variation of the skewness profile S(x) consistent with the opposite propagation directions of blobs and holes. Simulations will be discussed further in Secs. VII and VIII.D.

VI. Scaling of ballistic motion and blob particle transport

Because blobs are radially convecting structures, they will transport all plasma properties, including particles,[15] heat,[16,29] momentum[30,31] and parallel current.[56] Most of the theoretical and experimental work has been devoted to blob particle transport, because it is the easiest to calculate and measure, and its effect extends farther into the SOL than higher moments like the electron energy. (Note that the parallel loss time for particles is based on the sound speed, and is much slower than the electron-dominated parallel losses of temperature and vorticity. Thus, the ratio of perpendicular blob transport to classical parallel transport is larger for particles than for heat or vorticity.) Here, we will discuss blob particle transport for the case where the external force **F** can be expressed as an "effective gravity" term. An important special case is that of the curvature and $\nabla\mathbf{B}$ forces in toroidal devices such as the tokamak.

A. Theory of blob transport

One of the useful results of blob theory is a prediction for the radial velocity of the blob-filaments, which depends on both the driving force and the parallel current

closure. Here, we give a short summary of the basic ideas; the reader is referred to Ref. 3 for a more detailed discussion.

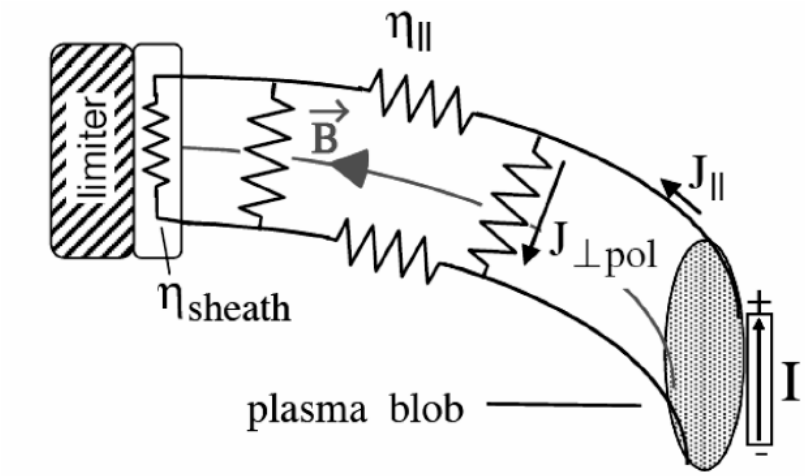

Fig. 22 Sketch of equivalent circuit with possible current paths for the blob shown in Fig. 1. The charge polarization from the effective gravity acts as a current source I and produces a parallel current with a dipole structure. Possible closures of the current loop are discussed in the text, including closure at the sheath (controlled by the effective sheath resistivity η_{sheath}) and closure by perpendicular ion polarization currents $J_{\perp pol}$ when the plasma resistivity $\eta_{||}$ is high or the driving force is uniform along B. Reprinted from Ref. 3 with permission from Cambridge Journals.

1. Blob equivalent circuit

A simple way to visualize the parallel current closure is to consider the equivalent electrical circuit[3,48] formed by the blob and the axial bounding surface (limiter or divertor plates), as sketched in Fig. 22. The charge polarization (from the effective gravity and resulting $\mathbf{g}\times\mathbf{B}$ drifts) acts as a constant current source for the blob and results in a dipole structure of the parallel current. At fixed current, the effective resistivity of the circuit determines the vertical potential difference Φ across the blob and the resulting radial $\mathbf{E}\times\mathbf{B}$ velocity, $v_x \propto d\Phi/dy$.

The effective resistivity depends on the current loops shown in Fig. 22. First, consider a simple tokamak with a limiter, where the effective gravity current source varies along the magnetic field and peaks at the outboard midplane. Then, assuming low plasma resistivity $\eta_{||}$, the current flows unimpeded along the field lines from the midplane to the sheath at the end plate, and the blob velocity is determined by the sheath resistivity, as discussed in Refs. 15 and 16. If $\eta_{||}$ is high enough, theory predicts that the path of least resistance is perpendicular to the field lines and the circuit closes in the divertor region.[43,48,121]

In diverted tokamaks, where the main plasma is bounded by a separatrix, the X-point can disconnect both the linear perturbations,[111,254] and the current flow for the nonlinear blobs,[39,40,48,73] from the divertor region. The disconnection occurs because a blob (flux tube) that has a circular cross-section at the midplane is stretched into a thin ellipse (even approaching an ion gyroradius in thickness) near the X-point by the magnetic field line mapping.[39,254] Consequently, a perpendicular current can easily flow across the thin dimension of the flux tube, dropping the effective resistance of the blob circuit as depicted in Fig. 22. (The elliptical distortion of the blob cross-section has been observed on C-Mod by GPI imaging at the X-point.[140]) Theory predicts that the blob current loop can be closed at the X-point by the perpendicular ion polarization current[40,48] or by collisional electron currents.[74] In other (non-tokamak) devices, the same competition between current paths manifests itself in different ways depending on the geometry and the distribution of the drive (e.g. curvature) along the field line.

For each of these current paths, blob theory allows one to estimate the radial blob velocity v_x, and it has a different scaling with blob size (and other parameters) for each current path in Fig. 22. To estimate the scalings, one can use the current conservation equation, $\nabla \cdot \mathbf{J} = 0$, or equivalently, the vorticity equation, Eq. (1). Balancing the effective gravity drive term with different current-closure terms in the vorticity equation gives different expressions for the radial velocity.[3,48] For example, if $J_{||}$ is proportional to Φ by

some effective conductivity parameter, $J_{||} \propto \sigma_{||eff}\,\Phi$, then the resulting potential will scale as $\Phi \propto F/\sigma$ where σ would include both $\sigma_{||eff}$ and a perpendicular conductivity due to the ion polarization drift term.

2. Blob correspondence principle

Another way of obtaining the scalings is to solve for the linear dispersion relation from a model drift-resistive ballooning equation and apply the "*blob correspondence principle*".[48] This principle states that the blob velocity can be obtained from the linear dispersion relation by means of the following substitutions:

$$\gamma \rightarrow \frac{v_x}{\delta_b},\ k_\perp \rightarrow \frac{1}{\delta_b},\ L_n \rightarrow \delta_b,\ k_{||} \rightarrow \frac{1}{L_{||}} \quad . \tag{6}$$

Here, $\gamma = \mathrm{Im}[\omega]$ is the growth rate of the linear instability, $k_\perp$ is the perpendicular wavenumber, L_n is the density gradient scale length, δ_b is the poloidal dimension of the blob, and $L_{||}$ is the length of the blob along the magnetic field. That nonlinear properties of turbulent transport can be inferred from linear ones was noted in Ref. 9 for sheath-interchange modes; Eq. (6) makes the correspondence explicit and generalizes it to include the collisional regimes. Note that the rule $\gamma \rightarrow v_x/\delta_b$, obtained by balancing $\partial/\partial t$ with $\mathbf{v}_{E\times B}\cdot\nabla$, is consistent with the notion of a coherently convecting object for which $d/dt \equiv \partial/\partial t + \mathbf{v}_{E\times B}\cdot\nabla \approx 0$. Scalings obtained from the correspondence principle show factor of 2 agreement with the results of seeded blob simulations.

3. Analytic blob velocity scalings

The correspondence principle has been used to derive analytic scalings for two physical models. In the first model,[48] the analysis uses a WKB approach to solve the drift-resistive ballooning equation and includes electromagnetic (EM) physics. This model implements the X-point BC used in Refs. 39 and 76 to include X-point effects on the parallel current closure.

The second study[51] uses a two-region (midplane-X-point) model to study the physics of disconnection along the field line in the electrostatic limit including X-point effects. The model permits studying the effect of collisionality and magnetic geometry on both turbulence and blob transport. This "two-region model"[51] employs a two-point approximation to the variation along **B** in a diverted tokamak**.** The coupled vorticity and continuity equations for each region (midplane or X-point) are solved in the radial-poloidal plane. The effects of magnetic field fanning and the magnetic shear near X-points are taken into account by means of a geometric mapping of the coordinates from one region to the other. An invariant scaling analysis of the model equations shows that the physics in this model can be characterized by four parameters:

- a *collisionality* parameter $\Lambda = \nu_{ei} L_{||} / (\Omega_e \rho_s)$;
- a *blob size* parameter $\Theta = \hat{\delta}^{5/2}$;
- a *magnetic field line fanning* parameter ε_x;
- a *scaled blob velocity* $\hat{v}$.

Here, ν_{ei} is the ion-electron collision frequency and $L_{||}$ the parallel scale length in the X-point region, $\hat{\delta} = \delta_b / \delta_*$ is a dimensionless blob size with $\delta_* \equiv \rho_s^{4/5} L_{||}^{2/5} / R^{1/5}$ and $\hat{v} = v_x / v_*$ is a dimensionless blob velocity with $v_* \equiv c_s (\delta_* / R)^{1/2}$. The parameter Λ is proportional to the resistivity impeding parallel current flow to the divertor region and is also a measure of the ratio of the plasma volume resistivity to the effective sheath resistivity. Λ is related to the SOL electron collisionality parameter ν_{*e} introduced by some authors as $\nu_{*e} = L_{||} / \lambda_{ei} = \Lambda (m_i / m_e)^{1/2}$, where λ_{ei} is the electron mean free path for collisions with ions. The parameter ε_x is inversely proportional to the local field line length and has a scaling with the elliptical fanning f of the flux tubes near the X-point, defined such that $\varepsilon_x << 1$ in typical X-point geometry.

A number of transport regimes are identified by this analysis,[51] as shown in Fig. 23: (i) the connected ideal-interchange (C_i) regime, which balances the curvature drive term in the midplane region with fanning-enhanced inertia in the X-point-divertor

region;[48] (ii) the sheath-connected (C_s) regime, balancing the curvature drive at the midplane with parallel current flow to the sheaths (limited by the sheath resistivity);[15,16] (iii) the resistive X-point (RX) regime, balancing the curvature drive at the midplane with parallel currents in the divertor region (limited by plasma resistivity $\eta_{||}$ or Λ); and (iv) the resistive ballooning (RB) or inertial[121] regime, which balances curvature drive with inertia in the midplane region. Thus, the model incorporates all of the current loops sketched in Fig. 22 which are electrostatic in origin.

In each parameter regime, the blob velocity has the scaling with poloidal blob size indicated in Fig. 23, and these solutions are continuous across the boundaries between regimes. An important feature of this model is that it retains the nonlinearity of the ion polarization drift convective term $[\mathbf{v}\cdot\nabla(\nabla^2\mathbf{v})]$ and allows one to study the transition between blobs which are electrically connected and disconnected to the sheaths. (For example, see the discussion of the effect of collisionality in Sec. VI C.) Finally, note that the terminology has been chosen to emphasize the close connection between the blob physics and the underlying linear instability physics.

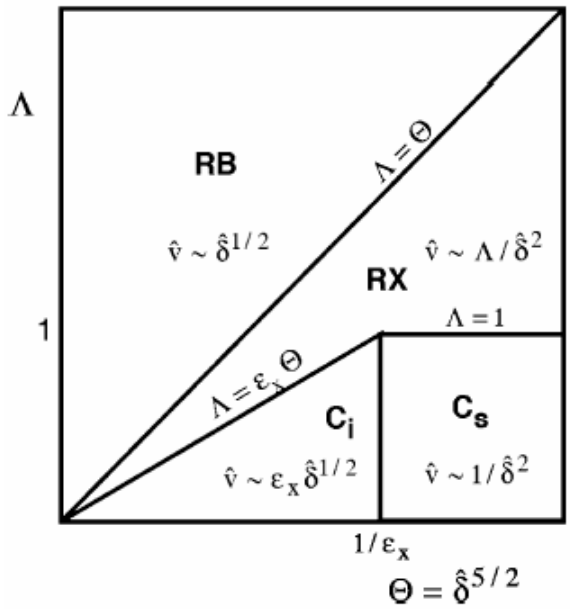

Fig. 23 Regime diagram for the electrostatic two-region model in the space of normalized collisionality Λ and scale size Θ. The scaling of the normalized blob velocity $\hat{v} = v_x / v_*$ with poloidal blob size $\hat{\delta} = \delta_b / \delta_*$ is shown in the figure for each regime. The normalization is explained in the text. Reprinted from Ref. 51 with permission from the American Institute of Physics.

Some results from seeded blob simulations using the two-region model equations are shown in Fig. 24. The measured blob velocities in the simulation (dots) agree reasonably well with the analytic blob dispersion relation (solid curves) obtained using the correspondence principle. (The analytic and numerical results for v_x agree to within a factor of 2.) These results support the validity of the correspondence principle and the velocity scalings obtained from it. In Fig. 24, for a given blob size, the analytic curve for v_x is approximately independent of Λ at both low and high collisionality and is proportional to Λ for intermediate collisionality. Noting that $\Theta > 1$ for both curves, this figure illustrates the transition between the C_s, RX and RB regimes in Fig. 23 as Λ increases. The observed increase in the convection velocity with collisionality is due to electrical disconnection from the sheaths.

Also, note the dependence on blob size in Fig. 24. For large blobs, the parallel current to the sheaths dominates over the inertial (vorticity) term and there is a large increase in blob velocity with collisionality Λ. For small blobs, the inertial term is dominant, and the path of least resistance uses predominantly cross-field currents. There is a weak dependence of the small-blob case on the parallel current (and thus collisionality) for the parameters used in this figure.

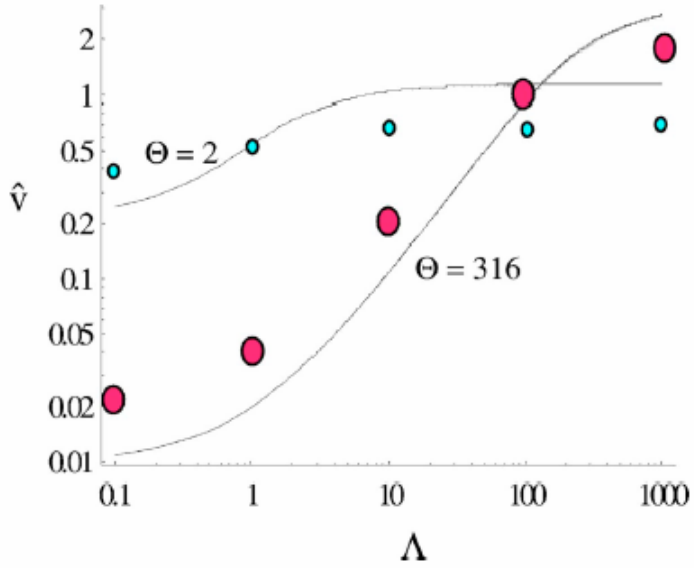

Fig. 24 (color online) Plot of normalized radial blob velocity as a function of collisionality parameter Λ for blobs of two different sizes: $\Theta = 2$ ($\hat{\delta} = 1.3$, small dots) and $\Theta = 316$ ($\hat{\delta} = 10$, large dots). The dots were obtained by measuring the blob velocities in the numerical simulation. The solid curves are from the analytic blob dispersion relation. Reprinted from Ref. 51 with permission from the American Institute of Physics.

The sheath-connected (C_s) and resistive ballooning (RB) regimes provide theoretical bounds on the scaling of v_x as a function of blob scale size. Both the WKB analysis of Ref. 48 and the electrostatic two-region model analysis in Ref. 51 predict that for a diverted tokamak geometry

$$\frac{1}{\hat{\delta}^2} < \hat{v} < \hat{\delta}^{1/2} \tag{7}$$

where

$$\hat{v} = v_x / v_*, \quad v_* = c_s(\delta_* / R)^{1/2}, \quad \hat{\delta} = \delta_b / \delta_*, \quad \delta_* = \rho_s^{4/5} L_{\|}^{2/5} / R^{1/5}. \tag{8}$$

It is important to emphasize that the inequality in Eq. (7) results from varying the collisionality parameter Λ, with the C_s regime applying at low collisionality and the RB

regime at large collisionality. Another derivation of these two regimes and a discussion of seeded blob simulations in both regimes is given in Ref. 49.

A number of additional closures are possible by including other physical effects in the vorticity equation. A comprehensive discussion of the closures is given in Ref. 3 and some other examples are discussed in subsequent sections of this review.

B. Experimental tests of theoretical scalings with blob size

1. Blobs

The velocity bounds obtained from the blob regime analysis are useful for comparison with experiment. In Refs. 30 and 135, gas puff imaging (GPI) data from an L-mode shot on NSTX was used to construct a blob database. The data was compared with the theoretical blob models, as shown in Fig. 25. Here, the He I 587.6 nm emission S_I was analyzed using the coronal radiation model relationship $S_I = n_0 F(n_e, T_e)$ together with the convective ansatz that $T_e = T_e(n_e)$, i.e. that the blob convects density and temperature together. The inferred density and temperature for each blob were used to evaluate the scale factors (c_s, ρ_s, etc.) used in the normalization. Finally, a restricted blob dataset was constructed based on several subjective criteria: brightness, image quality, symmetry, coherence, longevity and isolation from the frame edges and other blobs.[135] Thus, structures that most resembled the theoretical definition of a blob were selected. Even with this selectivity, there was a large variation in the radial velocity among the blobs (e.g. see Fig. 4 in Ref. 135), underscoring the difficulty of doing a detailed comparison between experimental data and analytic theory. However, in Fig. 25, the inferred blob velocities fall roughly within the theoretical bounds in Eq. (7), shown as the solid lines in the region $\hat{\delta} > 1$. Note that the experimentally observed blobs lie closer to the sheath connected regime than to the inertial/RB regime, and in fact seem to be bounded by $\hat{v} < 1$. An upper bound on $\hat{v}$ independent of $\hat{\delta}$ may be an indication that electromagnetic physics is playing a role.[30] In the region $\hat{\delta} < 1$, blobs are expected to be

unstable to Kelvin-Helmholtz instabilities (see Sec. VI.E), which preclude long-lived coherent objects, and in fact none are found in the restricted dataset.

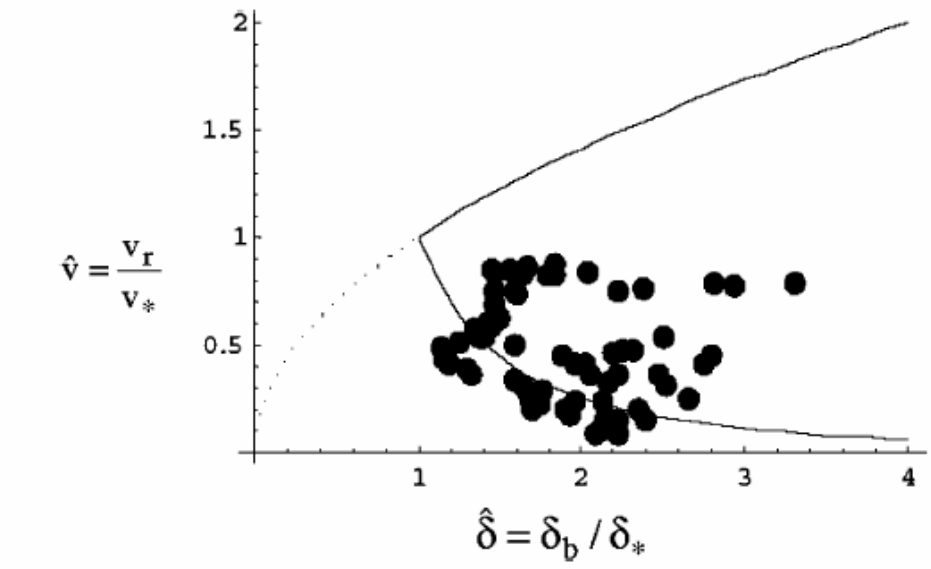

Fig. 25 Observed radial blob velocities on NSTX (filled circles) in the dimensionless parameter space of velocity and blob scale size. The data is approximately bounded by a theoretically predicted minimum and maximum (solid lines). Reprinted from Ref. 30 with permission from the International Atomic Energy Agency.

While this comparison between theory and experiment shows some areas of agreement, there are also some problems. An attempt to verify the detailed scaling laws for the sheath-connected and inertial regimes was not successful.[30,135] While the overall bounds were satisfied, there was a great deal of scatter. Some of the blob-to-blob variation was systematic and some was random. For example, one source of possible systematic error is the $L_{\|}(x)$ dependence of the blob-filament in X-point magnetic geometry, which was not measured; instead the estimate $L_{\|} \sim R$ was used for all x. The fact that the GPI blobs were turbulent objects introduces other sources of random variation, such as the initial amount of internal spin (monopole vorticity) that the blob is

created with; this vorticity slows down the blob's radial motion by reducing the charge polarization[40,69](discussed in Sec. VI.E.2). Also, $L_{||}$ itself may have statistical variations due to 3D turbulence effects in the blob formation process. Thus, it is rather difficult to make a detailed scaling comparison between experimental structures and theoretical blob models.

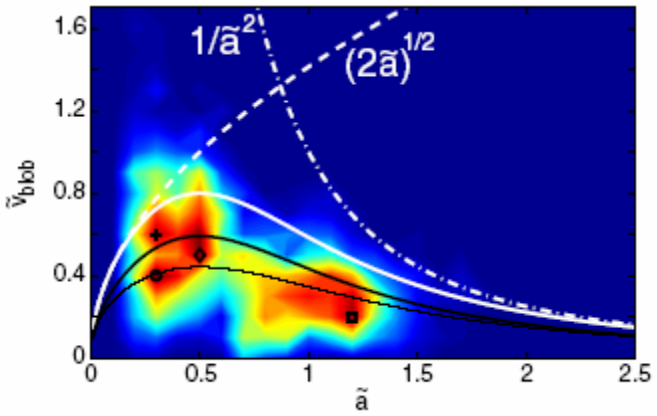

Fig. 26 (color online) Experimental evaluation of the distribution of $\tilde{v}_{blob}$ versus $\tilde{a}$ in TORPEX. The sheath-connected scaling (dot-dashed curve) and inertial scaling (dashed curve) are shown for comparison. The symbols indicate the peak of each distribution (H2, He, Ne, Ar). The other curves are described in the text. Reprinted from Ref. 208 with permission from the American Physical Society.

Another experimental study of blob velocity scaling[208] was carried out on the simple magnetized torus TORPEX.[198] This toroidal device has a simple open magnetic field line geometry with constant curvature along the field lines; the field lines terminate on metal plates at both ends of the machine. Cross-field blob sizes and velocities are obtained for a large number of blobs from a 2D array of Langmuir probes using pattern recognition. By varying the ion mass (H_2, He, Ne, Ar), the normalized vertical blob size $\tilde{a}$ was varied over the range $0.15 < \tilde{a} < 1.75$. A selected database of experimental blobs

was obtained by requiring that the blobs propagate radially and maintain their structure (no splitting or merging). The velocity of an individual blob was defined to be the mean velocity over its trajectory. The distribution of experimentally-inferred blobs having normalized velocity $\tilde{v}_{blob}$ and size $\tilde{a}$ is shown in Fig. 26 along with the theoretical curves for the sheath-connected and inertial/RB regimes in Eq. (7). In terms of the definitions in Eq. (8), $\tilde{a} \equiv \hat{\delta}$ and $\tilde{v}_{blob} \equiv \hat{v}$ to within factors of order unity. The figure shows that the blob velocity lies below the inertial regime boundary for $\tilde{a} < 1$ and below the sheath-connected boundary when $\tilde{a} > 1$. We will show that these results agree with theoretical expectations subsequently and contrast them with the tokamak case.

The other curves in Fig. 26 show the influence of two other factors on the blob propagation speed: a constant background density[67] and ion-neutral collisional damping.[131] The dependence on the background density was shown to be important in earlier seeded blob simulations, e.g. Refs. 37 and 67, and was discussed in Sec. V.A. The dependence of the blob velocity on the background density follows from the curvature term, $(\kappa / n)\,(dn/dy) \sim (\kappa/\delta_b)(\delta n / n)$. For large blobs, the sheath-connected result for the dimensionless velocity, taking into account the background density, is $\hat{v} = (\delta n / n)/\hat{\delta}^2$, whereas for small blobs the inertial scaling becomes $\hat{v} = (\delta n / n)^{1/2}\hat{\delta}^{1/2}$. [In Eq. (7) the factor $\delta n / n$ was set to unity but it is retained subsequently in Eq. (9).] The ion-neutral collisional damping dependence is also included in Fig. 26. When ion-neutral damping balances the curvature drive,[131,208] one finds that $\hat{v} \propto c_s /(\nu_{in}\rho_s)$.

The white curve in Fig. 26 shows the analytic result for the blob velocity with no background density and no neutral damping. The effect of an order unity background density is shown in the thick black curve, and the effect of adding ion-neutral damping is shown in the thin black curve. Figure 26 suggests that taking into account the background density (and hence the radial position where the blob was detected) is important in making this comparison, but that the neutral damping is weak in this experiment. An experiment in which the ion-neutral collisional damping was important is described in

Ref. 131. There it was shown that the blob velocity in the Versatile Toroidal Facility (VTF) is inversely proportional to the neutral pressure and is independent of the blob size, as expected theoretically.

Returning to the main theme of this sub-section, it is necessary to explain an apparent contradiction in the previous two figure, viz. why do the data points lie *between* the two theoretical curves in Fig. 25 but lie *below* both curves in Fig. 26? This is a subtle point which requires some discussion. An analysis shows that the difference lies in the two factors: the existence of electrical disconnection parallel to the magnetic field, and the role of electron-ion collisionality Λ (or equivalently, resistivity), which can play an important role in NSTX but is negligible in TORPEX for the parameters used in Ref. 208.

In a toroidal device with X-points, increasing Λ causes the blobs to disconnect the midplane region (where the curvature drive is strongest) from the X-point and divertor regions.[29,51] From the theory (Fig. 23) we see that finite collisionality leads to the scaling $\hat{v} = \Lambda / \hat{\delta}^2$, which lies between the two limiting cases, $\hat{v}_1 = 1/\hat{\delta}^2$ (sheath-connected) and $\hat{v}_2 = \hat{\delta}^{1/2}$ (disconnected). Thus, finite collisionality of the blobs in NSTX leads to data points between the two curves, $\hat{v}_1 < \hat{v} < \hat{v}_2$, and represents the physics of resistive ballooning, which localizes perturbations to the region of strongest curvature drive. On the other hand, in TORPEX the collisionality is low, the instability and blob velocity drive is uniform along the field line, and the physics involves a local competition between the two current paths corresponding to $\hat{v}_1$ and $\hat{v}_2$. This situation can be described analytically by considering the vorticity equation in a single region model (interchange limit), keeping the inertial, curvature and sheath terms. It can be shown that the solution of the blob dispersion relation has the property that $\hat{v} < \mathrm{Min}(\hat{v}_1, \hat{v}_2)$ in agreement with the TORPEX measurements in Fig. 26. An approximate blob dispersion relation (valid in the two asymptotic limiting cases of small and large $\hat{\delta}$) is $1/\hat{v} = 1/\hat{v}_1 + 1/\hat{v}_2$, which gives

$$\hat{v} = \frac{\hat{v}_1 \hat{v}_2}{\hat{v}_1 + \hat{v}_2} = \frac{(\delta n / n)\, \hat{\delta}^{1/2}}{(\delta n / n)^{1/2} + \hat{\delta}^{5/2}} \ , \qquad (9)$$

In Eq. (9) we have restored the background density dependence for future use.

Thus, in comparing the NSTX and TORPEX blob data, the differences in how the theoretical blob scalings bound the data appear to be due to their respective geometries and parameters, and in both cases the data are consistent with the theoretical expectations.

2. ELM filaments

Recently, there has been a great deal of interest in studying the formation and propagation of ELM filaments. A detailed discussion of the ELM literature is outside the scope of the present review, and the reader is referred to earlier review articles[6,255-257] for general background. Although we will not discuss the *formation* of ELMs, we point out that the nonlinear saturation of electromagnetic ballooning and/or peeling-ballooning modes near the pedestal can form ELM filaments (see Fig. 8 in Ref. 256) just as the nonlinear saturation of electrostatic edge turbulence near the separatrix forms blob filaments. In each case, the initial density and temperature of the filaments is characteristic of their birth location, so that ELM filaments (born at the top of the pedestal) have higher density and temperature than blobs (born near the separatrix).

It has been noted in many experiments that the radial propagation of ELMs is similar to that of blobs.[19,24,32-36] Here, we would like to mention one example that is very relevant to the present discussion of velocity scaling: an experimental study of the scaling of the radial velocity of ELM filaments with filament size and filament density was carried out on ASDEX-U.[258] The radial velocity was measured with a filament probe consisting of four radially separated pins located near the separatrix; the filament size was obtained by time delay measurements, and the filament density was inferred from the maximum ion saturation current for each filament. The main conclusion was

that large or dense filaments move faster than smaller or lower density ones. The database of filaments was analyzed to obtain the scaling $v_x \propto n_f^{1/2}\delta_x^{1/2}$, where n_f is the peak filament density and δ_x is the *radial* filament size (not the *poloidal* scale length, which enters the theory). If one assumes that $\delta_y \propto \delta_x$, the experimental scaling agrees with the RB/inertial scaling rather than the sheath-connected one.[258] However, one must be careful in comparing ELMs with electrostatic theory regimes. ELMs are electromagnetic (EM) in nature, at least at times near their creation, and should be compared with EM blob regimes (see Sec. VIII.D). In the limit of strong ballooning, an EM treatment[48] yields the observed scaling $v_x \propto \delta^{1/2}$, but there are also other relevant EM regimes.[39,48] Further analysis is needed to determine if this experiment is consistent with theory.

3. Inter-machine comparison

To summarize this section, in comparing analytic blob models with experiments, it is important to realize that there are several regimes with different blob velocity scalings. While there is some experimental and simulation support for the analytic scalings of blob velocity vs. blob size, the comparison is made difficult by turbulent fluctuations in the experimental blobs. Examples of unknown turbulent parameters would be the parallel structure of the blob and the blob azimuthal spin imparted by the turbulent birth process, which are very hard to measure. In spite of these difficulties, we can say that the blobs observed in most experiments lie between the theoretically-predicted bounds, as shown in Fig. 27 for the same set of tokamak data shown previously in Fig. 12.

Figure 27 carries with it the same caveats as Fig. 12: no attempt has been made to make the definitions and analysis of blobs the same for all experiments. The point here is that in an order of magnitude sense, observed blob properties are consistent with theoretical estimates. This is no small coincidence, as there are huge differences in

parameters between machines, e.g. a factor of almost 20 in (outboard midplane) magnetic field between C-Mod and NSTX.

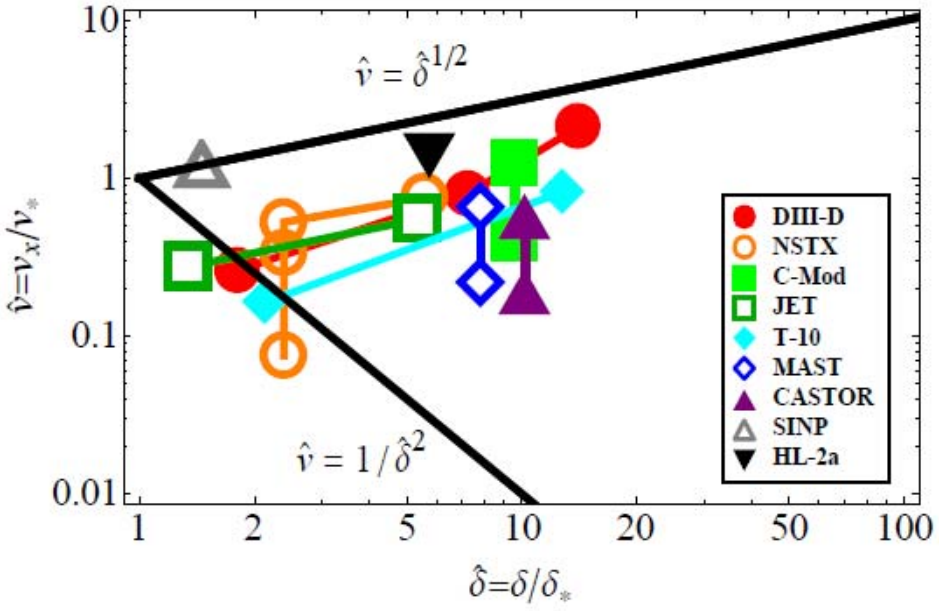

Fig. 27 (color online) Inter-machine comparison in the dimensionless blob parameter space defined in Eqs. (7) and (8): normalized blob velocity $\hat{v}$ vs. normalized blob size $\hat{\delta}$. Theory predicts that the blobs will lie between the two black lines, corresponding to the sheath-connected and inertial scalings, which is in reasonable agreement with the experimental data. This figure uses the same blob database as Fig. 12 but scales the velocity and blob size by v_* and δ_*, respectively. The references for the blob data are listed in the figure caption of Fig. 12.

C. Scaling of blob velocity with collisionality and magnetic geometry

1. Theoretical predictions

The blob radial velocity scalings in Sec.VI.A predict that in certain parameter regimes v_x has a dependence on both plasma collisionality and magnetic geometry (e.g. the parallel connection length $L_{||}$ and the presence or absence of X-points). In Sec.VI.B, this collisionality dependence was used to understand the experimental blob velocity data

in Fig. 25. In the present section, we elaborate on the theory and discuss whether other experimental trends support the theory.

In the resistive X-point (RX) regime, the two-region model (see Figs. 23 and 24) predicts that the convective transport in the SOL *increases* with collisionality (for fixed magnetic geometry, see Fig. 24), and it *decreases* with X-point fanning (at fixed collisionality). These trends can be understood in terms of the circuit picture in Fig. 22. For definiteness, we consider the case of diverted tokamak magnetic geometry and note the following points:

(a) for fixed X-point geometry, increasing the collisionality in the X-point region gives larger $\eta_{||}$ and thus *increases* the effective resistivity R_{eff} for the blob circuit, which in turn increases the blob velocity. The parallel currents are hindered by the high collisionality, and the blobs become electrically disconnected from the sheaths. (In the limit of complete disconnection, the blob enters the resistive-ballooning-inertial regime.)

(b) at fixed collisionality, proximity to an X-point has the opposite effect on the blob velocity: increasing the ellipticity of the fanned flux tube (blob) makes it easier for cross-field currents to flow across the thin part of the fan and thus *decreases* the effective resistivity of the current loop and reduces v_x. These cross-field currents cause the current loops to close before reaching the sheath, thereby also disconnecting them from the sheaths.

(c) both effects (collisionality, X-point magnetic shear) cause the blob to disconnect electrically from the sheaths, but the disconnection happens in different ways and has *opposite* effects on the blob velocity.

The cross-field currents at the X-point can be either ion polarization currents[40,48,51,259] or collisional currents.[39,47,76] The mathematical description of the X-point fanning effect is carried out by means of an X-point BC analogous to one originally used in linear theory.[111,112,254] A generalized BC that includes both types of cross-field currents has also been discussed.[74]

These theoretically predicted trends (collisionality and X-point effects) have been seen in seeded blob simulations[51] and full turbulence simulations[53] using the electrostatic two-region model. But the trend of increased turbulent transport with higher collisionality is far broader in scope than this particular model. It stems from basic resistive ballooning physics, and is qualitatively consistent with results from both electrostatic 2D[52,53,93] and electromagnetic 3D[40,260-263] turbulence codes. Ref. 28 gives a detailed discussion of the collisionality scaling of the cross-field particle and heat convection in the SOL of Alcator C-Mod. Finally, 3D BOUT code simulations show evidence of disconnection of the midplane turbulence from the divertor region.[40,74]

2. Experimental evidence for collisionality dependence

We now turn to the experimental side. There are at least two ways to test the theory: (i) investigate whether the blob velocity (or average convective velocity $v_{eff} = \Gamma / n_e$) increases with collisionality $\Lambda = (m_e / m_i)^{1/2} \nu_{*e}$, and (ii) look for lack of correlation between midplane and divertor turbulence, indicating blob disconnection from the sheaths. The relevant collisionality for disconnection is usually that of the SOL plasma in the X-point region. This type of experiment would be an important test of the basic theory, especially of the blob correspondence principle, which is based on the analogy between linear theory and blob physics.

Until recently, there has not been much data on measuring the collisionality dependence of the blob velocity. Several experiments have shown evidence of density profile flattening at high Greenwald fraction, $f_G \equiv \bar{n} / n_G$, or low plasma current I_p. These include C-Mod,[27,28,264] DIII-D[24,264] and TCV.[52,93] In each case, the density profile becomes increasingly flat, and the density at the wall increases, as a function of f_G or $1/I_p$. This is suggestive of a collisionality dependence because the collisionality scales as $\Lambda \propto n_e B a^2 / (I_p T_e^2)$. However, increased density in the far SOL is not necessarily caused by an increased blob velocity. It can also be due to increased neutral recycling at

the wall, as in the C-Mod main chamber recycling regime.[13,265] For example, in Ref. 27 the far SOL density increase with f_G was accompanied by a comparable increase in the inferred ionization source.

There is some other experimental evidence to support a collisionality dependence of SOL particle and heat transport on Alcator C-Mod, but it is hard to translate into direct comparisons with analytic blob models. In Ref. 27 it was shown that convective *particle* transport in the near SOL increased strongly with collisionality on C-Mod. Also, the region of strong convective *heat* transport ($Q_\perp > Q_\parallel$) grew broader with f_G, spreading from the far SOL to the near SOL[27] and crossing the separatrix into the edge plasma near the density limit,[137] e.g. see Fig. 6 in Sec. IV of this review. Reference 28 also discusses the collisionality scaling of the cross-field particle and heat convection just outside the separatrix of C-Mod, showing that $v_{eff} = \Gamma / n_e$ and the ratio of the heat fluxes parallel and perpendicular to the magnetic field, $Q_\perp / Q_\parallel$, increase with collisionality. In this study, the PDF of the turbulent D_α light intensity fluctuations changed from almost Gaussian near the separatrix to strongly non-Gaussian with a significant skewness in the far SOL, indicating that the turbulence near the wall is highly intermittent (due to blobby transport). All of these features are qualitatively consistent with the theoretical blob regime transition $C_s \rightarrow RX \rightarrow RB$ in the near SOL as the collisionality increases (see Fig. 23). However, direct comparisons with the theory are not yet available.

One attempt to carry out such a comparison is described in Ref. 29. In Refs. 26-28, it was reported that the L-mode density limit on Alcator C-Mod occurs at the collisionality where $Q_\perp > Q_\parallel$, e.g. see Fig. 18 in Ref. 28. Here, the Q's are power fluxes (normalized to the total input power) on a field line just outside the separatrix. These experimentally-inferred quantities were defined in Ref. 28 as follows: $Q_\parallel$ is the power conducted along field lines to the divertor based on $T_e^{7/2}$ integration across the SOL, and $Q_\perp$ is the power convected across the separatrix based on particle balance. It was found on C-Mod that $Q_\perp$ increased with collisionality.[26-28] The limiting condition suggests

that the density limit, or perhaps the trigger for the density limit, involves thermal collapse of the SOL due to the large turbulence level and resulting cross-field (blobby) heat transport at high collisionality. A model of this process was constructed,[29] assuming that the blobs were in the RX regime.

In this model, cooling of the X-point region increases the collisionality, which increases the blob heat transport, leading to further cooling, so that it yields a thermal transport catastrophe. If it is assumed that the collapse of the SOL temperature would lead to modification of the temperature and parallel current profiles inside the edge plasma (and thus trigger MHD activity), one has a plausible mechanism for a turbulent-transport-driven density limit. The analysis showed that there was a loss of thermal equilibrium in the SOL just beyond the critical collisionality where $Q_{\perp} > Q_{\parallel}$, which agreed qualitatively with the accessible parameter space in the experiment (compare Fig. 3 of Ref. 29 with Fig. 18 of Ref. 28). However, the agreement must not be overstated. The model used a number of assumptions that limit its generality. Moreover, the rapid increase in turbulent transport with collisionality is fairly general: it occurs in the edge plasma in a variety of 3D turbulence simulations and has been invoked to explain the density limit without recourse to blob physics.[260-263] Nevertheless, whether blobs cause the density limit or result from it, they are important objects to understand, if only as a diagnostic of the edge turbulence in these high $\bar{n}/n_G$ plasmas.

More generally, the conditions under which propagating blob convection dominates cross-field heat transport in the SOL are not well understood, and are also not universal. For example, a recent study[82] of the near-SOL heat flux width in H-mode plasmas suggests that the dominant contribution in that case comes from separatrix-spanning convective cells, which can be thought of as shear-layer-trapped (as opposed to emitted) blob structures.

Returning to the experimental results on collisionality scaling, it is important to distinguish between behavior in the near SOL and far SOL. Ref. 264 describes a series of

dimensionless scaling experiments on C-Mod and DIII-D showing that the SOL transport is very similar in the two machines. When profiles of $v_{eff}(x)$ were plotted for collisionalities spanning an order of magnitude on C-Mod, it was found that v_{eff} increased with collisionality near the separatrix, consistent with earlier work,[28,265] but was insensitive to collisionality near the wall. The v_{eff} profile on DIII-D was insensitive to collisionality everywhere, but the collisionality was not varied over as wide a range.

A more direct comparison was carried out in Ref. 24 for DIII-D data. Conditional averaging of reciprocating probe data was used to obtain the radial profiles of the blob density, temperature, and radial velocity in the SOL. Four values of the Greenwald fraction $f_{GW} \equiv \bar{n}/n_G$ and two values of plasma current were compared at constant B field, in an effort to directly measure the collisionality dependence of the blob velocity. This data was shown in Fig. 13 in Sec. IV.G. The radial decay of blob density and electron temperature is due to parallel losses, which are much faster for electron temperature. For comparison with theory, the most interesting result in this figure is that the blob velocity is independent of the line-averaged density (and corresponding changes in the far-SOL density and temperature), but increases with $L_{||} \propto 1/I_p$. This dependence on parallel connection length is consistent with both the sheath-connected ($v_x \propto L_{||}$) and the resistive X-point collisional ($v_x \propto L_{||}^2$) blob regimes. One cannot tell which regime describes the data best without knowing the scaling of the poloidal blob size δ with $L_{||}$, which was not reported in this paper. The parameters in the far SOL suggest $\Lambda \sim 1$ for this experiment, near the boundary of sheath connection and disconnection.

Another issue that may be important on DIII-D and other tokamaks is the effect of finite ion temperature ($T_i > T_e$) on the scalings of the blob velocity in the far SOL. This effect is briefly discussed in Sec. VIII.F.

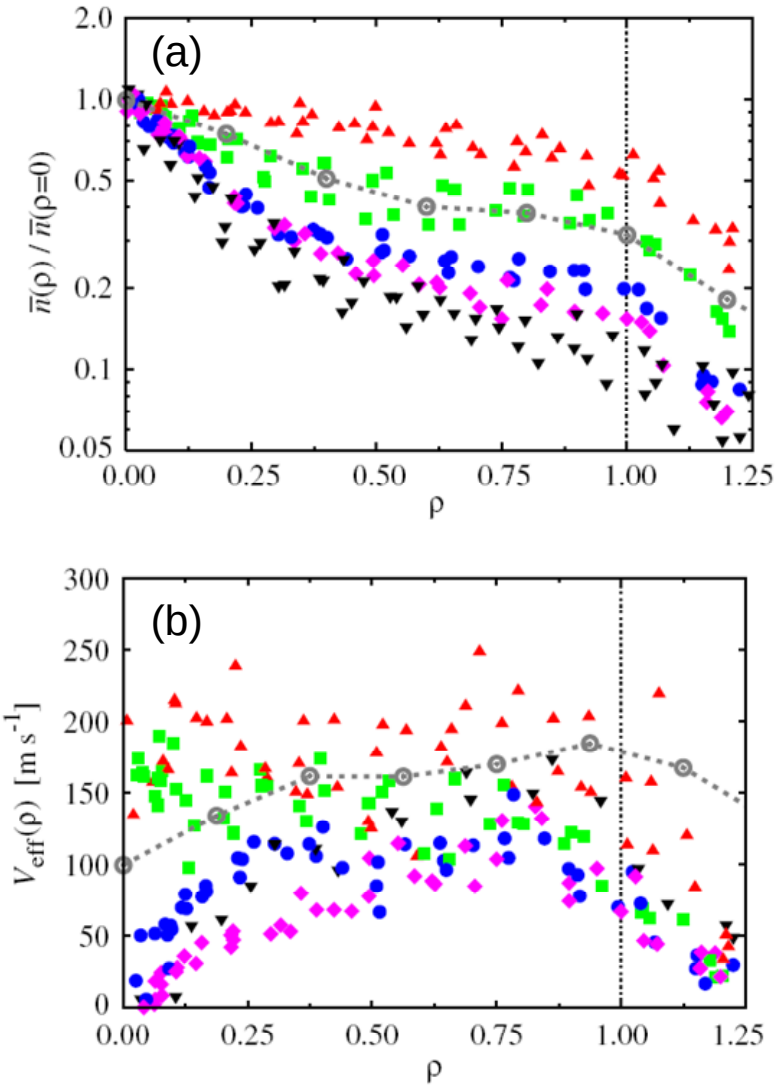

Fig. 28 (color online) Radial profile of (a) the time-averaged particle density in the SOL, normalized to its value at the separatrix ($\rho = 0$), and (b) $v_{eff} = \Gamma / n_e$ for a density scan in TCV. (The vertical dotted line at $\rho = 1$ denotes the position of the flux surface that maps from the probe position to the wall at the midplane in TCV.) The line-averaged core density $\bar{n}_e$ was varied from $\bar{n}_e = 4.4\times10^{13}\,\mathrm{cm}^{-3}$ (black triangle) to $1.1\times10^{14}\,\mathrm{cm}^{-3}$ (red triangles), which is near the density limit on TCV. The grey dashed curve is the result of the ESEL interchange turbulence code simulation. Note the logarithmic scale of the vertical axis. Reprinted from Ref. 93 with permission from the International Atomic Energy Agency.

Another recent series of papers[52,93,100] reported evidence that plasma fluctuations and radial transport increased with plasma collisionality in TCV. A scan in the line-averaged core density $\bar{n}_e$ was carried out at fixed plasma current I_p in Ref. 93, as well as a scan of plasma current I_p at fixed $\bar{n}_e$ in Ref. 52. The SOL turbulence properties for a high density case were compared with simulations using the ESEL interchange turbulence code (which uses the highly collisional inertial regime model). In these experiments, the collisionality parameter $\nu_e^* \equiv L_{||} / \lambda_{ei} \propto \bar{n}_e / I_p$ was varied over the range 10 to 100. This corresponds to a range in the parameter $\Lambda \equiv (m_e / m_i)^{1/2} \nu_e^*$ defined in Sec. VI.A (Fig. 23) of 0.2 to 2.3.

The time-averaged SOL particle density in TCV is plotted in Fig. 28 for the runs which scanned $\bar{n}_e$. The density profile is nearly flat out to the wall at the highest core densities, similar to the main chamber recycling regime on Alcator C-Mod. The effective convective velocity $v_{eff}(\rho)$ is also shown. In contrast to the DIII-D result in Fig. 13, there appears to be a density dependence in TCV, although there is a lot of scatter in the data points. This is particularly true near the separatrix at $\rho = 0$, where $L_{||}$ is the largest and disconnection is easiest. Also, in TCV[93,52] the time-averaged density $\bar{n}(\rho = 1)$ and radial particle flux density $\bar{\Gamma}(\rho = 1)$ at the wall increased proportional to $\bar{n}_e^{1.8} / I_p$, which may also indicate a collisionality dependence of the SOL transport. The role of neutrals and recycling was not addressed in these papers.

The results of a series of 2D turbulence simulations using the ESEL code are compared with the TCV data in these papers[52,93,100] as shown by Figs. 17, 20 and 28 in the present review. The simulations were done in the disconnected (resistive ballooning or inertial) regime and thus should be compared with the highest-density experimental case. The radial profiles from the simulations agree reasonably well with the data (Fig. 28), as do the simulated turbulence statistics at the wall such as the conditionally averaged pulse shape (see Fig. 17), the PDF of density fluctuations (see Fig. 20), the skewness, etc. (see also Sec. VIII.D.)

A tentative conclusion from this section is that there is mixed experimental evidence for and against a collisionality dependence of blob transport. More work would need to be done to make possible a quantitative comparison with blob theory or simulations. In particular, the possible collisionality dependences of the blob generation rate (i.e. packing fraction, see Sec. VII.B.1) and of the blob velocity would need to be disentangled. Quantitative evaluation of the blob regimes for these experiments is also needed. On the experimental side, this will require measurement of both midplane and X-point/divertor plasma parameters. On the modeling side, the use of theoretical tools that take into account realistic magnetic divertor geometry to assess disconnection is needed. At present, the BOUT turbulence code[40,74] and the newly developed edge eigenvalue code 2DX[266] are representative of two possible approaches. Some progress along these lines is discussed in the next section.

3. Experimental evidence for blob disconnection

There has been some recent experimental work on looking for more direct evidence of blob disconnection. In Ref. 140 gas puff imaging and fast framing cameras on C-Mod were used to view both the region just outboard of the X-point as well as the midplane. It was shown that a circular blob cross-section at the midplane maps to a highly elongated ellipse or "finger" that points mostly in the radial direction. A 3D BOUT turbulence simulation showed good agreement with many of the spatial features observed in the experiment. The observed elliptical distortion is a necessary ingredient for applicability of the X-point BC[39,76] that leads to blob disconnection in the theory. In more recent work,[267] it was shown by a cross-correlation analysis that blobs remain connected to the divertor at sufficiently large distances from the separatrix. But there is preliminary evidence to support disconnection close to the separatrix. First, the level of turbulence in the X-point is reduced on those field lines. Second, the turbulence statistics

are different and have different scalings with density in the two regions (midplane and X-point). The degree of connection has also been studied on NSTX for blob filaments.[136] In this experiment, using a new visible light imaging system, plasma filaments are observed on the lower divertor target plates, and both their motion and statistics (skewness and kurtosis) are found to be correlated with the filaments at the midplane, except in a small region close to the outer divertor strike point. These observations are consistent with the idea of blob disconnection by X-point magnetic shear near the separatrix.

To summarize Sec. VI.C, several experiments give evidence of strong collisionality dependence of the turbulent radial transport in the SOL, but these results do not necessarily imply a collisionality dependence of the blob velocity, although this is a clear prediction of theory and turbulence simulations. Among other things, the role of neutrals and main chamber recycling needs to be clarified. Recent experimental progress has been made in observing blob disconnection from the X-point region; this occurs on field lines sufficiently close to the region of high magnetic shear. These observations agree with predictions of the analytic blob models and simulations, e.g. see Fig. 3 in Ref. 40 and Figs. 9 – 11 of Ref. 74.

D. More general convective transport

So far in this paper, we have discussed the theory of blobs (as defined in Sec. II.B) whose motion is driven by an effective gravity term at the outer midplane. This model is relevant for both toroidal and linear machines. (See Ref. 3 for more details.) In tokamaks, blob-filaments can extend along field lines all the way to the sheaths ("sheath-connected") or be disconnected by X-point or collisional effects. In this section, we briefly mention a number of other blob theories which differ in the assumed forces, the shapes of the density perturbation, or in the location of the transport.

1. Other forces

First, there are nonlinear, coherently-propagating structures whose radial motion is driven by forces which do not have the form of an effective gravity. Two examples considered in Refs. 47 and 72 were radial convection driven by ∇T_e and by parallel shear of the $\mathbf{E}\times\mathbf{B}$ velocity. The corresponding linear instabilities are described in Refs. 268-270 for the ∇T_e instability and in Ref. 271 for the $\mathbf{E}\times\mathbf{B}$ parallel shear instability. In Refs. 47 and 72, a self-similar solution to the nonlinear equations is obtained for both instabilities, and the nonlinear structure has the form of an enhanced density "wedge" with a radial velocity in the range of $0.03 - 0.1\, c_s$ for typical parameters. In the nonlinear regime both modes are driven by strong nonlinear $\mathbf{E}\times\mathbf{B}$ drifts and the propagating solutions have the property that the $\mathbf{E}\times\mathbf{B}$ nonlinearity is balanced against dissipation (outgoing Alfvén waves in the case of the $\mathbf{E}\times\mathbf{B}$ parallel shear modes and by sheath dissipation in the case of the ∇T_e modes).

In related work, the convection of large-amplitude coherent structures in contact with divertor or limiter surfaces and driven by negative sheath impedance was considered in Refs. 43, 74 and 75. These blobs are the nonlinear limit of the conducting-wall temperature-gradient modes described in Refs. 269 and 270 and the physics is similar to the ∇T_e drive discussed in Refs. 47 and 72.

2. X-point effects, divertor leg blobs and plate tilt

Another novel approach to convective transport is the work on X-point effects, divertor-localized blobs and the enhancement of sheath effects by divertor plate tilt discussed in a series of papers.[73-76,78] The latter two effects may be useful for using blob convective transport to spread the heat load across the divertor plates.

In the previous section, we noted that theory predicts that X-point geometry can cause electrical disconnection of the midplane and divertor leg regions, at least on flux surfaces close enough to the separatrix. This disconnection causes a decorrelation of the

turbulence in the two regions, as observed in turbulence simulations.[40,53,74,77] Midplane blobs that are disconnected by X-point effects in the near SOL may eventually transition to the sheath-connected state farther out in the SOL. It was pointed out[74] that this occurs by sonic flow along the field lines as the blob moves radially; the blob slows down to the sheath-connected velocity when it re-establishes electrical contact with the divertor plate. This paper also presents a "heuristic BC" for taking into account all of the X-point effects (ion polarization and collisional currents, ion shear viscosity) on the moving blob.

If X-point effects are strong, there is also the possibility of instabilities generating blobs that are confined to the divertor legs.[73-76,78] These are bounded at one end by the X-point and at the other end by the sheath at the divertor plate. The divertor-leg blobs can be driven by the effects of local curvature, sheath impedance or by the effect of divertor plate tilt.[73,75] The latter effect occurs when the normal to the plate is not parallel to the poloidal magnetic field. The drive can be put into the form of an effective gravity g_{div} in the divertor region of the form[73]

$$g_{div} = c_s^2\left(\frac{1}{R} + \frac{\tan\alpha}{2L_{||}}\right) \tag{10}$$

where R is the radius of curvature of the field line, $L_{||}$ is the length of the field lines between the plates and the X-point, and α is the angle between the normal to the plate (facing outwards towards the plasma) and the *poloidal* magnetic field. It is important to note that the angle α can have either sign: positive (negative) when the normal is directed outwards (inwards) from the poloidal field line. Thus, the plate tilt effect can either increase or decrease the blob acceleration. Finally, various geometric effects on the motion of midplane and divertor blobs were treated analytically in Refs. 43,75.

The theoretical work makes two important predictions. The first is that increased collisionality in the divertor region should lead to increased convective radial transport in the midplane. This prediction is indirectly supported by experimental data (see Sec.

VI.C). The second prediction is that X-point geometry should cause the decorrelation of blobs (and thus of turbulent convective transport) between the midplane and the divertor region. There are practical reasons for studying this point. Strong convection in the divertor region, but not in the midplane, would be an ideal situation, spreading the heat load on the divertor plate while not increasing the particle and heat flux to the first wall. The idea of X-point disconnection has been observed in turbulence simulations[40,53,74,77] and more recently in experiments,[136,267] as discussed in Sec.VI.C.

E. Blob stability

The subject of blob motion would not be complete without a discussion of the question of blob stability, which determines the effective range of the convective radial transport. In order to transport plasma across the SOL, blobs must maintain their structural integrity during transit. However, the blobs observed in fusion devices do not seem to retain their size or structure as they propagate across the SOL [see Fig. 5]. To understand this, it is important to realize that blobs are subject to a number of internal (secondary) instabilities which affect their motion, their shape and their coherence. This is another consequence of the charge-polarizing force driving the blob motion. For example, in a tokamak the toroidal curvature and ∇B forces play three roles: (i) the curvature drives the linear ("primary") instability that develops into edge turbulence; (ii) the curvature drives the blob motion down the magnetic field gradient; and (iii) the curvature drives ("secondary") instabilities in the blob itself which can tear it apart. For the simplest case of isothermal blobs driven by an effective-gravity force in the sheath-connected regime, simulations have shown that there is a most stable blob size, and this sets a characteristic poloidal scale. In fact, this characteristic blob size δ_* turns out to be the same one that appeared in Eq. (8), defining the dimensionless blob size, $\hat{\delta}$.

1. Most stable blob size

There have been a number of seeded blob simulations which studied density blob stability as a function of the poloidal blob size δ_b.[37,41,49,57,67] The variation of blob stability with blob size can also be formulated as a dependence on the Rayleigh number $\mathrm{Ra} \propto \delta_b^3$.[49] These simulations show that some blobs are unstable, but others can propagate as coherent structures over large distances, depending on the dimensionless blob size $\hat{\delta}$ defined in Eq. (8). The stability of small blobs ($\hat{\delta} < 1$) is determined mainly by the Kelvin-Helmholtz (KH) instability,[37,121] whereas the stability of larger blobs ($\hat{\delta} > 1$) is determined primarily by curvature-driven instabilities.[37,67] [This is because the vorticity advection term arising from the left-hand-side of Eq. (1) is dominant for small scales, while the sheath conductivity ($J_{||}$) and curvature terms are dominant at large scales.] Blobs with $\hat{\delta} \sim 1$ are the most stable and propagate radially with the most coherence (see Fig. 29).[37]

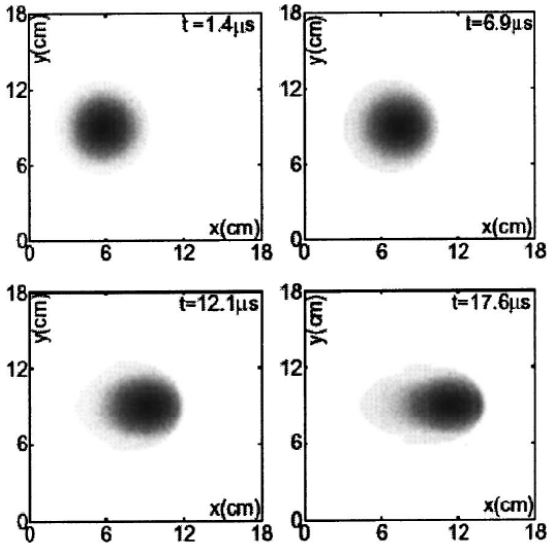

Fig. 29 Plot showing the evolution of a radially propagating density blob with $\hat{\delta} \sim 1$ in the x-y plane. This case is the most stable (to a combination of Kelvin-Helmholtz and interchange modes), and the blob propagates with a minimum of distortion. Reprinted from Ref. 37 with permission from the American Institute of Physics.

Thus, seeded electrostatic simulations in 2D slab geometry for blobs driven by an effective-gravity force in the sheath-connected regime predict that blobs of the optimal size $\hat{\delta} \sim 1$ can propagate across the SOL before being destroyed by secondary instabilities. The existence of an optimal blob size is a possible point of comparison with experimental data. If we assume that the very small and very large blobs die out quickly, we would expect that the blobs observed in an appropriate experiment would cluster around the optimal size. Figures 25 - 27 are consistent with this notion only to within an order of magnitude. A more careful study is needed to take into account the different widths of the SOL in various experiments, and the appropriate collisionality and geometry regimes. Experiments with narrow SOLs may allow a larger spread in the observable blob sizes. Of course, the k-spectrum of the instabilities responsible for blob formation will also play an important role. Further complicating the issue of blob stability, is the role of blob spin, discussed in the next subsection.

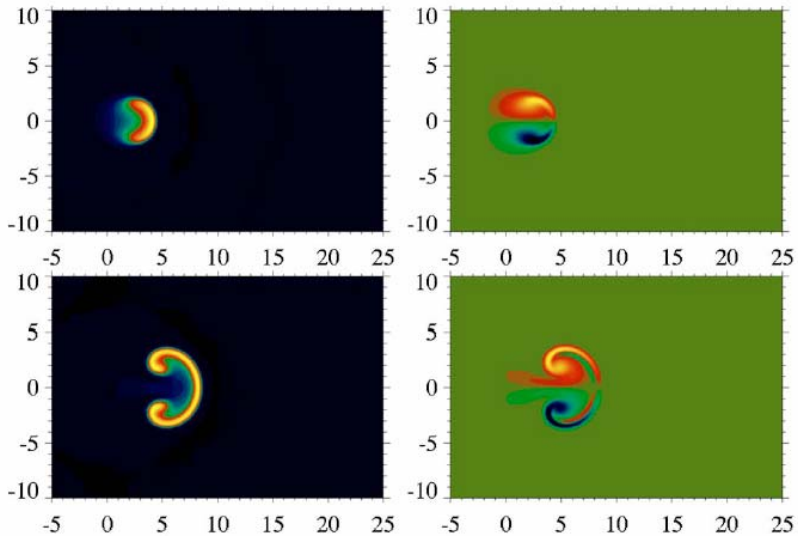

Fig. 30 Evolution of a small blob subject to the Kelvin-Helmholtz (KH) instability for Rayleigh number Ra = 10^4 and Prandtl number Pr = 1 (see the original paper for definitions). The time history of the density (vorticity) is shown in the left (right) column for t = 5 (first row) and 10 (second row). Here the spatial scale is normalized to the initial blob radius and the time is normalized to the ideal interchange time. Note the initial monopole structure of the density and the dipole structure of the vorticity, and the development of the characteristic "mushroom" shape of the velocity shear-driven KH instability in each lobe, as seen experimentally e.g. in Fig. 9. Reprinted from Ref. 49 with permission from the American Institute of Physics.

We conclude this section with a brief discussion of several points for which there is theoretical work but not much experimental data. Another potential point of comparison with experiments is the shape of the blob deformation. This shape is related to the secondary instability mechanism: smaller blobs tend to deform into a mushroom shape characteristic of the KH instability[37,41,49,57] (see Fig. 30), whereas large blobs break up into Rayleigh-Taylor lobes or fingers.[37,41,57,67] The degree of deformation is proportional to the growth rate of the secondary instabilities. According to theory, examples of factors which slow down the growth rate of secondary instabilities and

enhance blob cohesiveness include: higher background density,[67] larger sheath resistivity,[37,57,67] and larger viscosity.[41,43,49] In Ref. 43 the condition $\delta < \left(\eta^2 R / c_s^2\right)^{1/3}$ was given for the size limit of a sheath-connected blob stabilized by viscosity η.

2. Effects of internal spin and external sheared flow

So far in this section, we have discussed the theory of "cold" blobs with no internal temperature profile. For example, this applies to blobs in the far SOL which have equilibrated in temperature with the surrounding plasma because of rapid parallel heat loss. But "hot" blobs (or ELM filaments, which carry substantial amounts of heat) can have an internal temperature profile that decreases monotonically from the center of the blob to its edge. (Recent measurements[193,272] suggest that the temperature profile can sometimes be more complicated, having a dip in the center, but we restrict discussion here to the simplest case.) If these blobs are electrically connected to sheaths at the end plates, they will acquire an internal radial electric field from the Bohm sheath potential, $\Phi_B(r) = 3T(r)$, and thus will rotate or spin azimuthally.[68,69]

The blob spin is important because it tends to neutralize the blob charge polarization by mixing positive and negative charges (see Fig. 1), thereby increasing blob coherence and slowing down the radial $\mathbf{E}\times\mathbf{B}$ motion.[69] The blob temperature decays more rapidly than the density (this is predicted in theory[16] and observed experimentally[129,175,273]), but during this initial phase the hot blob will spin and its radial velocity will be reduced or suppressed.

If the blob spin is too rapid, it can cause another kind of secondary instability, a rotational mode driven by the centrifugal and Coriolis forces but stabilized by sheath conductivity.[68] The most unstable mode has an azimuthal mode number m = 2, which produces a characteristic "pinwheel" shape that could possibly be observed in 2D imaging data. However, so far there are no reported observations of this in experimental

data. The typical growth time for this secondary instability is short compared to the typical blob transport time, and the rotational mode can be the fastest secondary instability for larger blobs.

Another mechanism for generating blob spin is that turbulence can create a blob with a non-zero injection of (monopole) vorticity. This vorticity typically decays on a faster time scale than the density,[16] and the density blob is then free to move radially. This was observed in a BOUT turbulence simulation (see Fig. 2 of Ref. 40).

A third factor influencing blob stability is the effect of an externally-imposed sheared flow, $v_y(x)$, e.g. due to external biasing of the potential.[37,69,79] For non-spinning blobs, sheared flow was shown to inhibit radial transport,[16,37] but for spinning blobs the effect depends on the direction of the sheared flow relative to that of the blob spin.[69] In theory, sheared flow also affects the rate of blob formation by controlling the strength of the edge turbulence (see Sec. VII.A).

This section has summarized a number of blob properties related to the internal stability of the blob, which could be tested experimentally. So far little experimental work has been done in this area.

VII. Blob generation by turbulence

In previous sections, we discussed the dynamics of blob motion across the SOL, but now we turn to the subject of blob generation in the edge plasma. So far it has not been possible to understand blob generation quantitatively by analytical methods. Analysis of computer simulations and experimental data is required to make progress.

As discussed in previous sections, it was observed already in early experiments[8,97,118,229] and simulations,[11] and confirmed in a rapidly growing body of work comprising hundreds of papers, that intermittent turbulence occurs near the plasma boundary, characterized by large positive skewness and propagating coherent structures (blobs and ELMs). Recent theoretical work has supported the idea that blob and ELM

filaments are generated as part of the *nonlinear saturation process* of edge instabilities. These include rotational[223] or drift-wave[274] instabilities of cylindrical plasmas, broadband turbulence arising from drift-resistive interchange instabilities in tokamaks and other toroidal plasma experiments,[1] and peeling-ballooning instabilities driving ELMs in the tokamak H-mode.[275] The nonlinear saturation processes are not well understood and remain a subject of active research. Thus, they are outside the scope of this review. However, there is encouraging qualitative agreement between experiments and simulations on several relevant points. In this section, we illustrate some progress in understanding turbulent blob creation and the resulting intermittency of particle transport in toroidal plasmas.

A. Blob birth zone: role of gradients and sheared zonal flows

A consistent physical picture of blob formation is beginning to emerge from theory and simulations. The details depend on whether mean sheared flows are present, i.e. flows with $d\bar{v}_y / dx \neq 0$. Throughout this section, we will use the phrase "sheared-flows" to denote sheared **E**×**B** flows in the binormal (approximately poloidal) direction, either mean (zero frequency) or finite frequency sheared zonal flows. Weak sheared flows are often obtained in the tokamak L-mode regime or in experiments with large damping (e.g. due to ion-neutral collisions). Sheared flows can arise from momentum transport by Reynold's stress and momentum transport by blobs, even in the absence of external momentum input,[31] or by transport barrier formation, e.g. strong sheared flows in the edge are characteristic of the tokamak H-mode regime.

1. Sheared flow regimes

Theoretically, the role of sheared flows in edge turbulence is similar to that in core turbulence: turbulence generates zonal flows which act back on the turbulence and saturate the turbulent radial transport. There are some differences in the edge turbulence picture, viz. the dominant linear instabilities are different than in the core, fluctuations

relative to the background are much larger (order unity), and blobs contribute to the radial transport of particles, heat and momentum, carrying momentum across the separatrix where it is lost, thereby acting back on the sheared flows. A number of simulations have explored the physics of turbulence saturation and sheared flow generation in edge physics[11,31,55,61,62,81,88,100,276] but a detailed discussion of these simulations is outside the scope of this review.

The simplest way to describe the physics of blob formation is to contrast three regimes observed in simulations (and to some extent in experiments): (i) no sheared flow; (ii) weak sheared flow (modeling L-mode); and (iii) strong sheared flow (modeling H-mode). In regime (i) the coherent structures are radially extended (i.e. radial streamers rather than isotropic blobs). Streamers have been observed experimentally in both toroidal[233,242] and linear[277] machines. In regime (ii), the sheared flow is strong enough to break up the radial streamers into blobs, but not strong enough to suppress them. Finally, in regime (iii) the sheared flow can become so strong that it suppresses the turbulence locally by reducing the linear growth rate and tearing apart the coherent structures. In simulations the blobs are essentially confined inside of the sheared flow layer; in experiments, the number of blobs generated is greatly reduced (as discussed subsequently).

An experimental example of the possible variation of blob statistics with these regimes was described in Ref. 128 for NSTX. The number of blobs observed per unit time was higher in L-mode than in H-mode, but also increased with increasing power in H-mode, and decreased in low-powered Ohmic plasmas; however, a direct correlation of blob frequency with the measured shearing rate was not attempted. In the L-mode regime, blobs are often emitted into the SOL in bunches, and bursts of blobs are widely separated in time. “Quiet periods” before the L-H transition have also been observed on NSTX.[278] It is an open question whether the emission of blobs just before the L-H transition and during the H-mode is due to a periodic instability of the sheared flow layer

or due to some external perturbation from the core. This is a topic needing further study. The frequency of the blob bursts observed in experimental GPI time sequences decreases, and the waiting time between bursts increases, in moving from regime (i) to (iii).

We now turn to the physical picture of blob formation in each regime as deduced from simulations.

2. No sheared flows: radial streamers

In the absence of sheared flows, the physical picture of blob generation was described in Ref. 53 for the case of curvature-driven interchange modes. The present discussion is adapted from that reference. In the simulations, curvature-driven blobs tend to arise near the maximum of the linear growth rate, or equivalently, of the logarithmic pressure gradient, $1/L_p \equiv -\nabla_x(\ln p)$. This defines the "birth zone" of the blobs in the absence of velocity shear. The small initial positive and negative density perturbations of the interchange mode grow and eventually disconnect as part of the turbulent saturation process, forming blobs and holes, respectively. At this point the Rosenbluth-Longmuir charge-polarization mechanism, which was driving the linear instability, causes the coherent objects to move: the positive-density blobs move outwards and the negative-density holes move inwards (see Fig. 3). This preponderance of positive (negative) events outside (inside) the birth zone is reflected in the radial variation of statistical moments such as the skewness S. (see Figs. 18 and 31).

A statistical analysis of the turbulent fluctuations in the simulations shown in Fig. 31 supports this picture. In each of the four cases, we find that S(x) changes sign near the point of maximum linear growth rate: S = 0 in the birth zone (reflecting the equal number of blobs and holes created by the interchange nature of the underlying instability), S < 0 in the direction of hole propagation (up the magnetic field and density gradients), and S > 0 in the direction of blob propagation (down the magnetic field and density gradients). In these simulations, the $n_e(x)$ and $T_e(x)$ profiles are fixed in the core

(acting as particle and heat sources for the simulation) but are free to fully evolve in the SOL. Thus, in Fig. 31(a) the density profile is flattened where the blob convective transport is dominant, and the left boundary of this region is the blob birth zone. We see that the blob birth zone is identified by S = 0 and (in the absence of sheared flows) coincides with the maximum logarithmic derivative of the density profile and thus with the maximum growth rate. These features of the birth zone and its relation to the pressure and skewness profiles are general and apply to the case of streamers (no sheared flow) as well as blobs (sheared flow). We will return to this point subsequently.

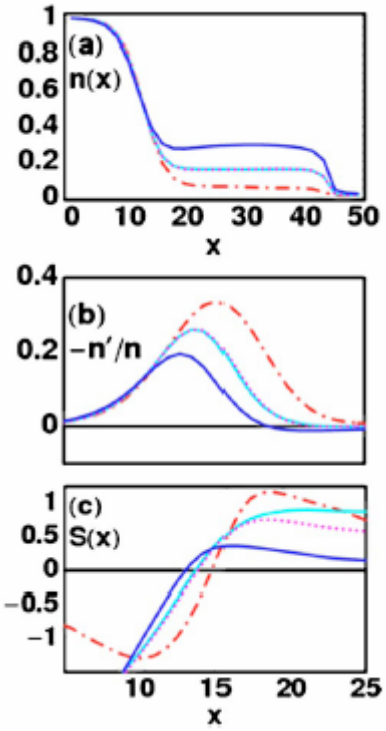

Fig. 31 (color online) Radial profiles from a 2D turbulence simulation without sheared flows: (a) poloidally and temporally averaged density n(x); (b) logarithmic pressure gradient $1/L_p = -d(\ln p)/dx$; and (c) skewness of density fluctuations S(x). The four simulations differ in magnetic geometry and collisionality, as described in Ref. 53. Reprinted from Ref. 53 with permission from the American Institute of Physics.

Finally, an interesting aside: changes in the collisionality and geometry leading to the different curves in Fig. 31 suggest a violation of the far-SOL universality discussed in Secs. IV.H and V.C. However, in the case of the streamer-dominated simulations in Fig. 31, one cannot really define a far-SOL region. In contrast to the ballistic propagation of blobs, which are isolated from their birth region in the far SOL, streamers, by definition, always connect back to the birth zone.

Next, we consider the case with sheared flows in which streamers are broken up into blobs.

3. Weak sheared flows: blobs (L-mode)

Based on 2D simulations, a condition for sheared flow to break up streamers into blobs was given in Ref. 61. The streamer break-up condition is that the time τ_s for shearing the radial streamer must be shorter than the radial convection time τ_x, where $\tau_s = \delta_y / \Delta v_y$, $\tau_x = \delta_x / v_x$, $\Delta v_y = (\partial v_y / dx)\, \delta_x \equiv v'_y \delta_x$, and δ_x, δ_y are the blob dimensions in x and y. These results can be combined to give the following condition for streamer break-up:[55,61]

$$v'_y \delta_x^2 > v_x \delta_y \ . \tag{11}$$

In the limit of isotropic blobs ($\delta_x \sim \delta_y \equiv \delta$), the condition for blobs to form is $v'_y \delta > v_x$. The blob correspondence principle[48] discussed in Sec.VI.A gives the relation $v_x = \gamma\, \delta$, where γ is the growth rate of the underlying linear instability producing the turbulence. Combining these results, we obtain the following condition for streamer breakup[81]

$$v'_y > \gamma \ . \tag{12}$$

A recent study of turbulence saturation using the SOLT 2D turbulence code found that Eq. (12) is the condition for sheared-flow turbulence saturation to win out over wave-breaking (profile flattening).[81] In other words, Eq. (12) is the condition to move from regime (i) to (ii).

Even in the weak-sheared flow regime, the pressure gradient is important in determining the location of blob generation in experiments. In NSTX, the birth of blobs at the location of the maximum $1/L_p$ gradient was confirmed by blob tracking (see Fig. 8 in Ref. 135) for a low-power L-mode shot. An analysis of data for an Ohmic shot in the HL-2A tokamak[126] also shows the role of the pressure profile. The radial profile of $-d(\ln p)/dx$ has a maximum just inside the separatrix, where the skewness is close to zero, and conditional averaging reveals that the density holes and blobs are born at this location (see Figs. 4, 6 and 7 in Ref. 126). Finally, a series of L-mode shots on Alcator C-Mod[137] showed that the blob birth zone moved inwards as the normalized density (n_e/n_G) was increased, where n_G is the Greenwald density limit. For $n_e/n_G > 0.6$ the blob birth zone moved inside the separatrix and both the gradients and fluctuation levels inside the separatrix were observed to increase. Visual evidence for blob birth inside the separatrix was provided by gas-puff imaging (see Fig. 6, which is Fig. 5 of Ref. 137). It was concluded that the blob birth zone was associated with the gradients rather than with the transition from open to closed field lines. In these experiments the sheared flows were evidently sufficiently weak that they did not determine the location of blob generation (e.g. through shifting of the location of the maximum linear growth rate of instabilities).

Similar conclusions were obtained by the analyses of turbulence data from TORPEX.[132,202,204,206] This experiment has no limiter and no open-to-closed field line boundary, so every helical field line terminates on metal plates at the two ends. Despite the simplicity of the configuration, blob formation is observed; the blobs transport plasma from the source region to the wall. It was shown in these papers that the blobs originate from the crests of interchange waves and are correlated with the maximum gradients (e.g. the steepening of ∇p precedes blob emission in the time history). It was also suggested[202] that the turbulence saturates, and blobs form, by wave-breaking, which is similar to recent simulation results obtained in the limit of weak sheared flows.[81] However, sheared flows may have played a role in this experiment, as the velocity

shearing time was comparable to the blob transit time.[132,204] We will return to this point below.

4. Strong sheared flows: blobs (H-mode)

The effect of strong sheared-flow layers (produced by biasing) was studied by theory, simulations and experiments in several papers;[37,69,79,216] this work gives a qualitative picture of the effect of the self-generated flows in the H-mode. These simulations show that the effect of sheared poloidal flows is to strongly suppress the blob transport across the shear layer. The blobs are either trapped inside the sheared-flow layer or they are torn apart by the shear, depending on parameters. Recently, 2D simulations of SOL turbulence were carried out[82] for some NSTX H-mode shots using the SOLT code. These simulations show evidence of blob trapping by the strong sheared-flow layer, and the same qualitative behavior is seen in the experimental GPI time sequences.

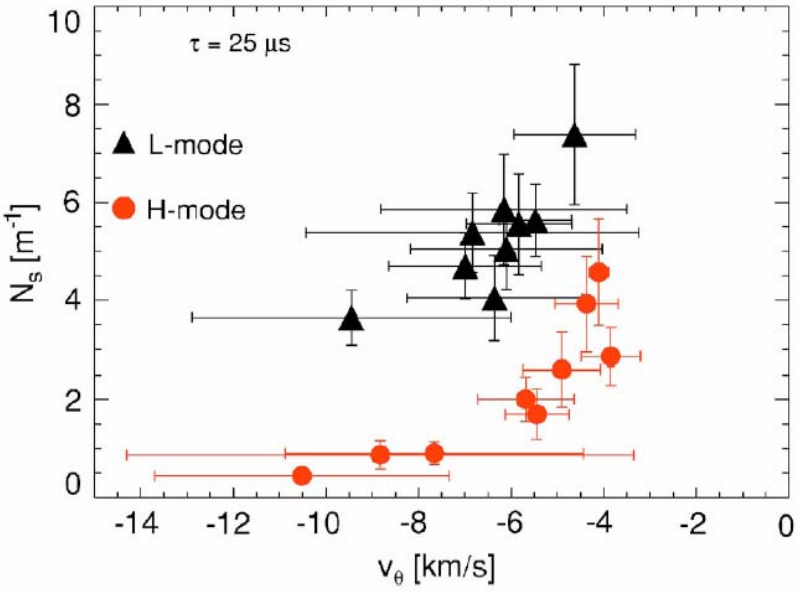

Fig. 32 (color online) Linear spatial density of (blob) structures (N_S) in NSTX with characteristic time scale $\tau = 25\,\mu s$ at a radial position 1 – 2 cm outside the separatrix. N_S is plotted as a function of the poloidal velocity for the L-mode (triangles) and H-mode (circles). Each point refers to a different shot. Negative v_θ corresponds to the ion diamagnetic direction. Reprinted from Ref. 22 with permission from the American Institute of Physics.

There is some experimental evidence to support the role of sheared flow in blob generation. In Ohmic plasma experiments on JET[144] and ASDEX-U[169] it was shown that the blobs are born in the vicinity of the sheared flow layer. In Ref. 22, NSTX data from a radial and poloidal GPI array of photomultiplier tubes (PMT) was analyzed to compute the linear spatial density of structures (blobs), $N_s = \Delta N_\tau / (v_\theta \, \Delta t)$, as a function of the poloidal velocity v_θ for both L- and H-modes (see Fig. 32). Here, ΔN_τ is the average number of events with characteristic time scale $\tau = 25$ μs in the time interval Δt. This number density is normalized to the poloidal velocity, because the number of structures that cross the PMT chord is proportional to v_θ. Figure 32 shows that the linear density of bursts in H-mode is smaller than that in L-mode, even at the same poloidal velocity. This suggests that the increased velocity shear in H-mode reduces the blob production. Also, N_s decreases as v_θ increases (in either L- or H-mode). If the poloidal velocity *shear* scales in the same way as the velocity itself, this could be interpreted as evidence of blob suppression or trapping by the velocity shear.

A recent study in TORPEX[132,204] also lends some experimental support to the role of sheared flows in generating blobs. It is shown that the blobs form during the nonlinear saturation of an interchange mode, resulting in radially-elongated structures. The elongated structure is convected by the $\mathbf{E}\times\mathbf{B}$ flow and is eventually sheared off, forming a blob on the low field side (e.g. see Fig. 5 in Ref. 204). Consistent with this picture, the calculated velocity shearing time is of the same order as the blob transit time, so that condition (12) is satisfied.

5. Blobs due to drift waves

We have seen that the strength of the sheared flows is an important parameter controlling the blob generation. Another important parameter is the nature of the linear instability driving the blob creation. So far we have discussed the case where the

dominant instability inside the LCFS and in the SOL is the curvature-driven interchange mode (at low collisionality) or the resistive ballooning mode (at high collisionality). In this case the blobs are born near the location of the maximum linear growth rate, whether that is inside or outside of the LCFS.[137] The change of magnetic topology from closed to open field lines can either play a role or not in determining the maximum growth rate, depending on the regime. In the interchange regime, the mode extends far along the field line, effectively performing a weighted average over the curvature (of the flux surface, or of the SOL field line).[112] In this case, the topology change is important. Conversely, in the resistive ballooning regime, where the mode is essentially confined to the outboard midplane, the topology change is unimportant.

In some devices the dominant instability is the drift wave, and radially propagating blobs are not observed.[222] In some intermediate cases, the dominant instability is the drift wave inside the LCFS and the interchange mode outside the LCFS. This is a direct result of the topology change: the closed surfaces with rotational transform do not allow $k_{||} = 0$ except on rational surfaces, and thus favor the finite $k_{||}$ drift-Alfvén modes; the open field lines permit $k_{||} = 0$ interchange modes.[279] In this situation, the phase shift between density and potential changes across the LCFS, and radially propagating blobs are typically born just outside the LCFS where the interchange mode is dominant and the phase shift is $\pi/2$ (e.g. see Figs. 3 and 4 in Ref. 144). Examples of experiments in which blob formation involves drift waves include the TJ-K stellarator[184] and the linear experiments VINETA[219] and CSDX[222].

6. Other nonlinear effects on blob formation

Another theory of blob generation in L-mode examines the nonlinear effects of Reynolds stress and inverse cascade of drift wave turbulence on the interchange-ballooning instability.[80] The basic idea is that finite amplitude perturbations can seed the ballooning instability even when it is subcritical, because the meso-scale perturbations

associated with the inverse cascade of drift turbulence at the outboard side of the torus cause locally steep density gradients, leading to blob formation. The calculation yields a meso-scale structure size of order $\Delta_m \sim (\rho_s^2 R)^{1/3}$ and a critical plasma beta for ballooning instability at this scale of $\beta_{crit} \sim (1/q^2)(\rho_s/R)^{2/3}$. It is pointed out that some aspects of this theory are consistent with experiments, e.g. (i) the observation on TORPEX[132,204] that a strong increase of local plasma pressure gradient occurs just before blob formation, and (ii) the observation on Alcator C-Mod[28] that the strong increase in turbulent flux associated with the density limit on that machine occurs for $\beta >$ const. / q^2, similar to the size and scaling of β_{crit}.

B. Blob generation rate

Experimental and simulation data on SOL turbulence show that blobs are relatively rare events, even in cases like the tokamak L-mode where the turbulence is strong and the sheared flow is weak. In this section, we estimate the blob generation rate and discuss how to quantify this aspect of intermittency using the concepts of "waiting time" and "packing fraction."

1. Estimates of blob birth rate and packing fraction

The blob generation rate was estimated for Alcator C-Mod as follows.[15] For typical parameters, blobs having a perpendicular scale $\delta_b \sim 1$ cm can propagate radially a distance of 10 cm at a typical speed of $v_x \sim 10^5$ cm s^{-1}, where a parallel connection length $L_{||} \sim 5\times10^2$ cm was assumed. For a blob density of $n_b \sim 10^{13}$ cm^{-3} (local density near the separatrix, where the blob was born), the blob carries approximately $N_b \approx (\pi\delta_b^2)L_{||} \sim 10^{16}$ particles. With this particle content, and assuming a typical particle flux across the separatrix of $\Phi_p \sim 10^{22}$ s^{-1}, the blob formation rate is $F_b = \Phi_p / N_b \sim 10^6$ s^{-1}. Finally, if the blob formation is spread over a poloidal distance of $L_\theta \sim 50$ cm, then the frequency of plasma oscillations producing the blobs can be

estimated as $\omega_b \sim F_b(\delta_b / L_\theta) \sim 10^4\ s^{-1}$, which is in the range of typical edge instabilities.

This highly intermittent transport is characterized by large skewness of the PDF (see Sec.V.B) and by a small value of the "packing fraction," $0 < f_p < 1$. The packing fraction for the density is defined by[22,53,189]

$$f_{pn} \equiv \frac{\bar{n}_e}{n_b} = \frac{2\delta_b}{\Delta x} = \frac{\tau_b}{\tau_w} \quad , \tag{13}$$

where $\bar{n}_e$ is the time- and y-averaged electron density, $n_b = \bar{n}_e(x_b)$ is the average blob electron density at the birth location $x = x_b$, and $\Delta x = v_{xb}\tau_w$ is the spacing between consecutive density blobs. In the last form of Eq. (13), the packing fraction is expressed as the ratio of the waiting time τ_w between two consecutive blobs and the time $\tau_b = 2\delta_b / v_{xb}$ for a blob to pass by a given point. In the idealized model of a train of equally-spaced identical square-pulse blobs, one can compute both the packing fraction and the skewness analytically.[83] In the highly intermittent limit ($f_p << 1$ and $S >> 1$) one finds that $f_p \sim 1/S^2$. Thus, large skewness implies small packing fractions and long waiting times. A typical value for the skewness *of density fluctuations* in the far SOL is S ~ 2, but the skewness of other quantities (e.g. nonlinear products like pressure or flux) is usually higher.

2. Experimental data

Experimental data on packing fractions, waiting times and/or "quiet times"[280] can be found for tokamaks and spherical tori,[22,166,242,280] stellarators,[280] RFPs[189] and a simple magnetized torus.[202] Radial profiles of the packing fraction are also reported.[22,204,242]

As already discussed, the GPI data on NSTX[22] shows that the number of blobs entering the SOL drops as the sheared flows increase (see Fig. 32). This suggests that the packing fraction should decrease (skewness increase) in moving from the weak to the

strong sheared flow regimes. For several different L-mode shots in this experiment, Fig. 6 in Ref. 22 shows that the skewness of the NSTX GPI intensity is in the range S = 4-10 in the far SOL, and Fig. 8 in Ref. 22 shows that the packing fraction $f_p \equiv \sum_\tau \tau N_\tau / \Delta t < 0.2$ throughout the SOL.

VIII. Ongoing and future work

In previous sections, we reviewed blob particle transport with occasional comments about heat and momentum transport. There are other topics which could be considered but are not yet fully developed or are outside the scope of this paper. These include blob transport of heat, momentum, parallel flows and parallel current; a fully electromagnetic theory of blobs and ELMs; experimental modeling with 2D and 3D turbulence codes; the inclusion of blob effects in 2D SOL transport modeling; and inclusion of finite ion temperature effects. In this section, we give brief discussions of some of these issues that may be important areas for future work.

A. Blob-generated sheared flows

In Sec. VII, we discussed the theory of how the radial electric field shear (or poloidal velocity shear) regulates the turbulence and contributes to the formation of coherent, isolated blob structures. There is theoretical and simulation evidence that blobby turbulence also affect the flows, resulting in a coupled self-regulating system, as is argued for other turbulent systems.[281] The spontaneous self-consistent generation of binormal (y) or approximately poloidal, zonally-averaged flows in edge turbulence simulations is commonly seen together with the dynamics of blob formation and ejection.[31,61,62,81,282] The radial structure of the flows $v_y(x)$ typically gives rise to a flow shear layer near the blob "birth zone" which also is located approximately where the logarithmic pressure gradient maximizes (see Sec.VII.A). These zonally-averaged flows typically exhibit both a steady time-independent part, and a time-fluctuating part. The

latter is linked to relaxation oscillations associated with turbulent bursts that release the blobs.[62,81]

The underlying mechanism for flow generation is the Reynolds stress $\langle v_x v_y \rangle$. In edge plasmas, it is often best to treat flow generation from the momentum conservation equation, using the total momentum flux $\langle n v_x v_y \rangle \approx \langle n \rangle \langle v_x v_y \rangle + \langle n v_x \rangle \langle v_y \rangle$. Noting that n and v_x are in phase for a blob structure, the last term will be recognized as a "passive" flux corresponding to the fact that the blob carries $\langle v_y \rangle$ with it as it transports particles. This term cannot *generate* flows and is usually responsible for edge flow dissipation by transport of y-momentum into the SOL. The first term is the usual Reynolds stress term weighted by the mean density. In the absence of momentum sources and sinks, steady state momentum conservation requires $\partial_x \langle n v_x v_y \rangle = 0$ so that the turbulence only moves momentum from one location to another, giving rise to bipolar flow layers in which $v_y(x)$ changes sign. However, structures, such as blobs and convective cells,[82] that cross from closed (edge) to open (SOL) field lines, carry momentum into the SOL where it is ultimately dissipated in sheaths.[31] In this case, net unidirectional flows in the edge can be created. For a model drift-wave system it was found that the flows are in the electron diamagnetic direction in the edge region, and in the ion diamagnetic direction in the SOL.[31] The flows in this simulation were driven by a net momentum flux, illustrated in Fig. 19. It has been suggested that an analogous transport of *toroidal* momentum by blobs into the SOL is associated with the phenomenon of "spontaneous" toroidal rotation.[85] Finally, it should be noted that **E**×**B** flows in the ion diamagnetic direction in the SOL are expected in any case due to the radial variation of the sheath potential ($\Phi_{sh} \sim 3T_e$).

Experimentally, the observation of strongly sheared flows in edge plasmas is ubiquitous.[1] It is frequently found (e.g. see Ref. 283) that flows reverse from the electron to the ion direction across the separatrix. The relationship between these flows and the edge turbulence (blobs) is still not well understood. In the linear CSDX device,[284] flows

were shown to be described by a residual stress term that could have its origins in either blob emission or radial wave propagation arising from symmetry breaking at the plasma boundary. Earlier studies[285] also demonstrated some links between bursts of outward going particle flux and momentum flux associated with the dynamics of the shear layer. In contrast to these results, in experiments on the simple magnetized torus, TORPEX,[203] it was found that cross-field flows transfer energy to the blobs, and blob transport of toroidal (approximately parallel) momentum from the plasma region modifies the toroidal flows.[209] Very few tokamak experiments have attempted to diagnose the momentum and energy transfer mechanisms associated with blob dynamics. Exceptions are a set of experiments on JET[144] and ASDEX-U.[286] In Ref. 144 poloidal flows, momentum flux, and the energy transfer rate between the meso-scale (i.e. blob) turbulence and the flows was studied on JET. The blob formation and subsequent radial transport was associated with the driving of azimuthal flow. In Ref. 286 the radial transport of poloidal momentum in the SOL of ASDEX-U was investigated using a reciprocating probe with a special probe head that can measure the radial and poloidal electric fields. This allows each of the momentum flux components to be inferred separately. The time history of the integrated radial flux of poloidal momentum at a point in the SOL was compared for L- and H-modes, and the flux of poloidal momentum was found to be almost two orders of magnitude larger in H-mode than in L-mode. In these H-mode experiments there was a large external momentum input due to neutral beam injection, and this momentum was transported into the SOL by the ELM filaments.[286] Interestingly, the mechanisms responsible for the momentum flux (e.g. Reynolds stress and passive flux, as discussed in Sec. VIII.A) differed in the L- and H-mode cases.

B. Ballooning and parallel transport in the SOL

It is well known that curvature-driven instabilities in both high-beta ($\beta \equiv 8\pi p / B^2$) and resistive plasmas have their largest amplitudes on the outboard low-

field side of the torus. This "ballooning" effect allows the modes to concentrate in the region of the field line where the pressure-gradient-weighted curvature is unfavorable for plasma stability. In a fully non-linear treatment, blobs are formed from the crests of unstable ballooning perturbations. Therefore, the plasma ejected by the newly formed blob-filament should have a higher pressure near the outboard midplane than elsewhere along the field line. In the SOL, parallel particle flow at the sound speed is expected to occur in response to this pressure imbalance. The time scale for achieving pressure balance along the field line, $\tau_{||} \sim L_{||}/c_s$, can be compared with a typical time scale for blob convection, $\tau_{\perp} \sim L_{\perp}/v_b$, where v_b is the blob velocity and $L_{\perp}$ is a perpendicular scale of interest (e.g. the blob radius, the near-SOL width, or the gap between the LCFS and the wall). If $\tau_{||} >> \tau_{\perp max}$ then particles are lost to the wall (e.g. as in the C-Mod main chamber recycling regime[13]); however, more generally, parallel sonic expansion will deliver some particles to the divertor plates and limiters.

The interplay of parallel flows and perpendicular convection can be very subtle. Perpendicular blob dynamics in toroidal geometry leads to radial, poloidal and toroidal displacements of the free end of the filament. As motion perpendicular to **B** occurs, theoretical calculations[74] show that parallel flow (typically with velocity less than c_s) determines whether the filament stays in contact with a fixed poloidal location, e.g. the X-point region[74] or the divertor plate; this affects the parallel closure physics and hence the blob velocity. The dynamics of blob-filaments undergoing simultaneous perpendicular convection and parallel expansion remains to be studied in detail in either 3D simulation or theory models, even at the fluid level. Moreover, it is likely that kinetic effects play a role in describing the parallel propagation of plasma. Similar issues have been addressed (at the fluid level) in the context of pellet fueling.[287]

Some of the underlying concepts have been modeled for the SOL using 2D fluid turbulence codes. In Refs. 86,93-95 qualitative agreement with TCV and JET data was obtained for the $\mathbf{B}\times\nabla\mathbf{B}$-independent part of the parallel SOL flow. In this work it was

assumed that as the blob drifts across a given field line it perturbs the local pressure and launches a sound wave towards both divertor plates. The parallel Mach number $M_{||} \sim v_{||} / c_s$ was estimated from the fraction of the time that intermittent blob events create a significant pressure excess on a given flux tube (i.e. from the packing fraction). The same model could be used to estimate the parallel Reynolds stress, i.e. $\langle v_r v_{||} \rangle \propto \langle v_r p \rangle$ where $p = nT_e$ is the pressure, and showed qualitative agreement with experimental measurements. However, studies of these effects in 3D turbulence models still remain for future work. Other experimental investigations of the parallel Reynolds stress[288,289] suggest a rich and bidirectional link between the parallel and perpendicular dynamics.

Experimentally, the ballooning nature of transport and the existence of consistently directed (i.e. sourced at the outboard midplane) parallel flows below the sound speed have been documented.[86,93,153,290-292] To our knowledge, however, the expected sound time scale $\tau_{||}$ for front propagation has not been observed directly in the context of blob-filaments. Some indirect evidence comes from the T-10 tokamak, where the propagation of turbulent structures from the outboard to the inboard side of the torus at the sound velocity was proposed as a possible mechanism to explain a radial shift of order $v_b \tau_{||}$ between inboard and outboard profiles of blob fluctuation levels and their statistical moments.[160]

In other experiments, faster propagation times (on the order of a few μs), more likely associated with the electron time scale, have been observed between midplane and divertor plate blob diagnostics.[136,141] These may represent parallel propagation times for electron energy or electrostatic potential through the background plasma on which the denser blob-filament sits, as its density expands along the field line at the slower sub-sonic speeds. Also see the discussion of blob parallel expansion in Ref. 74.

Perhaps the best direct evidence for parallel sonic expansion of filaments comes from the case of ELM filaments where the condition $\tau_{||} \sim \tau_{\perp}$ is more easily met. Data from both JET[95,293] and DIII-D[273,294] is consistent with the picture that ELM filaments

are ejected mostly on the low field side, thereby launching a sound wave or perhaps a sonic front that propagates along the field lines. However, at low densities, this picture is apparently not so clear.[294]

The implications of intermittent parallel flows and their likely origins in the radial transport of initially non-uniform (along **B**) ELM or blob filaments is a subject of active theoretical investigation.[288,289,295,296] In particular, the intermittent nature of these processes raises difficult issues for transport modeling. As is also the case for the intermittent cross-field blob transport, statistical closures would be needed to properly handle the averages of products (or non-linear functions) of density, temperature, flow velocity, etc. We return to this point later.

C. Electromagnetic effects on blob-filaments and ELMs

Up until now, we have considered the dynamics of blob-filaments in the electrostatic (ES) approximation. To the extent that comparison of blob theory and simulations with experiments has been possible, the electrostatic model appears to describe most of the observed features. The theory of electromagnetic (EM) effects on blob-filaments has been reviewed in previous works[3,45] and will not be discussed in any detail here. Rather, we focus on two electromagnetic aspects that appear to be related, at least qualitatively, to experimental observations. These are (i) field line bending and (ii) current-carrying filaments.

When the plasma contained by a blob has a sufficiently high value of $\beta \equiv 8\pi p / B^2$, the moving filament has the ability to carry "frozen in" magnetic field lines with it as it convects radially. In a tokamak, where the filaments have a ballooning structure on the outboard side of the torus, this physics causes the midplane region of the filament to move outward radially while the foot-points (near the top and bottom of the torus) are relatively fixed. The amount of bending of the field lines is estimated as[39] $\Delta \sim L_{||}^2 \beta / R$ where $L_{||}$ is the length of the filament and R the major radius of the torus.

Thus, the condition for the line bending to be important is $\beta > \beta_c \equiv R\,\Delta_w / L_{\|}^2$, where Δ_w is the distance from the separatrix to the first wall; when this condition is satisfied, the field lines will touch the wall at the midplane without their ends hitting the divertor plates. Physically, field line bending is related to parallel Alfvén wave emission. This emission provides dissipation which adds to sheath losses and competes with inertia to establish the blob or ELM filament dynamics.[39] The same mechanism has also been shown to be relevant for the expanding cloud of a high beta pellet injected into the core plasma.[117,297] In this regime, the physics governing the midplane filament velocity is independent of that at the foot-points, so the same dynamics also holds for high-β SOL blobs (in the RX-EM regime) that essentially terminate at the X-points.[48]

A second effect, in principle unrelated to the first, is the fact the blobs can transport current (as well as particles, energy and momentum). Parallel current transport, i.e. current-carrying filaments,[56] provides an additional mechanism by which electromagnetic effects enter the blob picture. An isolated filament carrying a unidirectional current propagates at the characteristic (current-free) blob speed, but has greater cohesion due to the attraction of mutual parallel currents within the structure.[56] In addition, because anti-parallel currents repel, filaments can interact with an image (e.g. current hole, or conducting wall) causing acceleration or deceleration.

Experimental evidence for these effects is qualitative at best. In reversed-field pinches (RFPs), which are inherently high-β devices, current-carrying filaments generated by the turbulence have been observed and studied by their magnetic signatures.[193,241,298] In tokamaks, evidence for field-line bending and current transport by filaments comes almost exclusively from ELM observations. ELM filaments are commonly observed in tokamak H-modes[19,24,32-36] (also see the review in Ref. 256) and in recent nonlinear MHD simulations of ELMs.[90,275,299-303] Ref. 90 explicitly discusses the observation in the simulations of ELM filaments which carry current. Here we note a

few cases in which observations seem to support the theoretical points (i) and (ii) mentioned earlier.

SOL currents have been observed in DIII-D and have been associated with ELMs.[304] Current-carrying ELM filaments have been observed in MAST[32,305] and JET[36] by their magnetic fluctuation signature. The current density in the filaments was found to be of the same order as that of the edge plasma where the filaments are believed to have been born. Field-aligned holes left behind after filament ejection have also been reported in experiments.[306,307] The repulsive interaction of the current filaments with the holes left behind is consistent with the acceleration of ELMs into the SOL that has been observed in some experiments,[308] although other experiments have reported radial deceleration of ELMs.[258,273] Moreover, initial radial acceleration is also qualitatively consistent with explosive ballooning instability theory[309] such as seen in the initial phase of nonlinear ELM formation in simulations.[275] Thus the role of current on the filament dynamics is largely open.

Many experimental papers have measured the radial propagation velocity of ELMs[25,33,35,273] and some have carried out scaling studies and/or made comparisons with simple (inertial and sheath-connected) blob propagation models.[258,293] However, there have been no attempts to date at quantitative identification of specifically EM regimes predicted by blob theory. There was an indication of a blob velocity scaling independent of normalized blob radius[30] (see Fig. 25 in Sec.VI.B) that is consistent with the high-β RX-EM regime;[48] however, the available data did not permit a strong conclusion.

Qualitatively, there are indications that field-line bending may describe certain features of ELM observations in the SOL. In spite of parallel losses, it was estimated[24] that the filament density in the far SOL is comparable to the pedestal density. It has also been estimated[33] that the energy loss from an ELM cannot be described by the energy content of a completely detached filament. These observations are consistent with the

picture that ELM filaments bulge and propagate out at the midplane and possibly interact with the wall,[310] but that, owing to high-β field bending, they retain their connection to the closed surfaces for some significant portion of the propagation time. This connection would keep the flux tube filled with plasma density and energy as it moves outwards, unlike a (detached) SOL flux tube which loses particles and energy to the sheath.

Thus, the EM blob convection regimes discussed in Refs. 39 and 48 may be responsible for the motion of the ELM filaments observed in many experiments, but more work is needed to confirm this point and to assess the effect of parallel currents on the ELM motion. Many other factors beyond the scope of this review must be understood before a predictive model of ELM particle and heat transport is possible. A good review of present theories of ELM filament formation and dynamics is given in Sec. IV of Ref. 257 and the experimental data is summarized in Ref. 256.

D. Comparison of turbulence simulations with experiments

There has been a growing effort to simulate edge and SOL turbulence in recent years because of the importance of the edge for core confinement and the interaction of the SOL plasmas with plasma facing components. In surveying the literature, the term "the edge" is used to describe both the transport barrier region where the drift wave and ion temperature gradient (ITG) instability (and/or their suppression) are dominant considerations, and the closed field line region just inside the separatrix or LCFS, where the drift-resistive-interchange and ballooning modes occur. A full discussion of edge turbulence in either of these closed field line regions is beyond the scope of this review, where we limit ourselves to the physics of blob-filaments. The region just inside the separatrix has been briefly discussed in the section on blob generation. In the present section, we focus the discussion on turbulence in the SOL outside the LCFS.

Quantitative modeling of SOL turbulence and blobs in experiments is not easy for a number of reasons. First, one cannot experimentally measure all of the inputs to such

codes, and setting the remaining parameters requires good judgment. This is particularly true when trying to model a 3D SOL plasma with a 2D code. Many runs and careful comparison of simulation trends with the experimental data are required to take into account both input uncertainties and model sensitivity. Second, it is important to process both the simulation data and experimental data using exactly the same algorithms and approximations. Finally, there is a trade-off between the fidelity of the model and the ability to obtain useful information: e.g. 3D codes are time-consuming and difficult to run for this sort of study (which involves full profile evolution with large fluctuations in the SOL), whereas 2D codes allow extensive parameter studies with self-consistent SOL profiles, but are only approximations to the full 3D physics (neglecting, or modeling in an over-simplified way, most physics parallel to **B**).

With regard to this last point, the justification for using 2D turbulence codes to treat toroidal plasmas deserves further discussion. If taken literally, the assumption of interchange-like behavior along the magnetic field is hard to justify in the edge region of a tokamak. By design, a field line inside the LCFS is stable to an ideal interchange mode because of the pressure-weighted good curvature in the high-field region. However, ballooning modes which localize on the outside of the torus can go unstable. In the same way, blob generation by curvature requires resistive effects to isolate the bad curvature region. Either the plasma resistivity localizes the mode structure to the outer midplane (resistive ballooning) or, in diverted tokamaks, X-point shear, together with even a small resistivity, localizes it between X-points[111,112] (RX mode). Recent measurements with fast visible imaging on Tore Supra[292] showing filaments only on the outside of the torus illustrate this point. The important point is that 2D turbulence codes can approximate this disconnection from the good curvature region by an appropriate choice of effective curvature $1/R_c$ and parallel connection length $L_{||}$.

Some simulations have focused on studying and characterizing the statistics of intermittency and the formation of coherent structures; this work has been discussed in

earlier sections of this review. The simulations typically use BCs specifying the particle and heat flux at the LCFS, or other equivalent particle and heat sources in the edge region, to drive the turbulence. The turbulence then creates blobs as part of the turbulent saturation process. (Here, "saturation" means that the time-dependent intensity of the turbulent fluctuations settles down to a quasi-steady state after an initial transient.) By adjusting the parameters controlling the turbulent intensity (e.g. the parameters for source rates, the curvature-drive, dissipation, and sheared flow), one can control the rates of turbulent transport and blob generation. Comparisons of simulation with experiment can be carried out for the following quantities: radial profiles for n_e, T_e (or the GPI intensity), statistical quantities characterizing the turbulence (e.g. skewness S, kurtosis K, PDFs), statistical analysis of the blob distribution (e.g. PDFs of blob velocities and blob sizes), etc. The simulations also describe the competition in the near SOL between "normal" (Gaussian) turbulent transport and transport by blob-filaments.

A detailed discussion of this topic is outside the scope of the present review, but we would like to point the interested reader to a number of useful papers in this area, most of which deal with particle transport only. In Table V we summarize points of comparison between SOL turbulence simulations and experimental data relevant to blobs, which can be found in the published papers listed in the table. There are separate tables for 2D and 3D turbulence codes. In each case we have listed the name of the simulation code, the experiment, the areas of comparison, and references to the corresponding papers. A cross in the box means that the indicated comparison was attempted, but does not necessarily imply that good agreement was obtained. Both qualitative and quantitative comparisons were included in the table.

Table V Comparisons of SOL simulations and experimental data: (a) 2D simulations, (b) 3D simulations

2D codes	FDET	ESEL	ESEL	SOLT	----	ESEL
Experiment	Aditya	TCV	JET	NSTX	Helimak	ASDEX-Upgrade
Fluctuation levels	×	×	×	×		
Turbulent spectra					×	
Correlation times or lengths		×			×	×
Skewness, PDFs	×	×		×	×	
2D imaging		×	×	×		
Radial profiles		×	×	×	×	
Blob properties		×		×		×
References	61	93,100	86,94	46,82,101	102	272

3D Codes	BOUT	BOUT	BOUT	NLET	BOUT	GEMR
Experiment	DIII-D	C-Mod	NSTX	C-Mod	MAST	C-Mod
Fluctuation levels		×		×	×	×
Turbulent spectra			×	×		×
Correlation times or lengths		×	×	×		×
Skewness, PDFs					×	
2D imaging	×			×		
Radial profiles		×				
Blob properties	×	×		×	×	
Parallel mode structure		×	×			
References	88	74, 88,140	88	20,21	91	311

In the present review, special attention is focused on simulation studies that have made comparisons with experiments that relate directly to blob properties. As shown in Table V, such comparisons have been carried out for C-Mod,[20,74,88,140,311] DIII-D,[88] NSTX,[46,82,88,101] MAST[91] and TCV.[93,100]3D simulations have been used to make comparisons of blob size (or poloidal correlation length),[74,88] parallel filament structure,[74,88,140] and blob velocity.[74,91] Typically, the agreement was reasonable (factor of 2) for some quantities but poor for others. In some cases, it was impossible to compare the same quantities in both simulation and experiment; in other papers, the simulation parameters were not varied over a large enough range to optimize the comparison. 3D simulations are time-consuming, and such optimization is rarely possible. For this reason, 2D SOL turbulence simulations remain very useful, because they can be run over a wide parameter range to obtain optimal comparisons with data and to identify physical trends. Two examples are the comparison of the ESEL code simulations with TCV data[93,100] and the comparison of SOLT code simulations with NSTX data.[46,82,101]

The ESEL code results were compared with the TCV data in the form of radial profiles in the SOL of density, radial particle flux, skewness, flatness and the Mach number for parallel flow.[93,100] Also the "pulse shape" obtained by conditional averaging (see Fig. 17 of this review) and PDFs of density and radial particle flux (see Fig. 20) were compared with the TCV data[100], as discussed in Sec.VI.C. Experimental data was taken over a range of line-averaged densities[93] and it was found that the radial profiles varied with density or collisionality; the code results were in reasonable (factor of 2) agreement with the highest density cases ($\sim 0.8–1.0 \times 10^{14}$ cm^{-3}). This agrees with theoretical expectations because in these simulations the ESEL code modeled the inertial or resistive-ballooning (RB) regime (as defined in Fig. 23).

The SOLT 2D simulations of NSTX turbulence[46,82,101] added the new feature of a synthetic diagnostic for calculating the gas-puff-imaging (GPI) intensity I. This allowed a comparison in which the data from the simulation code and the experiment were

analyzed by identical algorithms. Radial profiles of the mean and median intensity and the skewness S_I of the intensity fluctuations were compared for both simulations and experiments. The sheath loss terms were retained (sheath-connected regime) so that the parallel connection length $L_{||}$ entered as a parameter in the model. Some effort was put into determining the optimal effective values for the curvature drive, connection length, and dissipation parameters in order to get the best agreement with the experimental profiles. Another unique feature of these simulations was an analysis of blob statistics, obtained by creating a blob database and using a blob tracking algorithm to follow the structures from frame to frame in the GPI time sequence. This analysis[46] yielded the number of intensity blobs per radius, the PDF of poloidal blob size, and the PDF of image and **E**×**B** velocities.

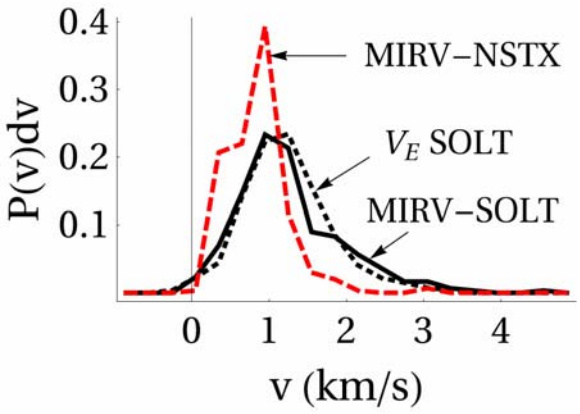

Fig. 33 (color online) The distribution of the maximum image radial velocity (MIRV) for the SOLT simulation (solid, black) and for the NSTX shot (dashed, red), and the distribution of the radial convection velocity, v_{Ex}, measured at the intensity maximum of the brightest blob in each frame of the SOLT simulation (dotted, black). Reprinted from Ref. 46 with permission from the American Institute of Physics.

One of the few examples of a quantitative comparison of blob properties (as opposed to general turbulence statistics) between simulation and experiment is shown in

Fig. 33, for the PDF of the radial blob velocity. Figure 33 employs a sophisticated analysis procedure which serves to illustrate the difficulties in these types of comparisons. Simulations give access to all dynamical variables and one can extract the local electric field and hence calculate the **E**×**B** velocity of the blobs directly. This is not the case for the experimental GPI data, where only the image velocity (i.e. the velocity at which the visible intensity structures appear to move) is available. This raises several validation issues.[46] One issue is whether blob images in the experiment really move with the local **E**×**B** velocity, which can also include internal structure (Fig. 14) as well as a spin component. For a structure that is changing shape while traversing the SOL it is difficult to determine where to measure the **E**×**B** velocity (center of mass, leading edge, at the point of maximum amplitude). A related issue has to do with the method and reliability of extracting a velocity from the moving (and constantly distorting) images in the GPI data. In fact, the latter problem is rather subtle, and has been addressed in work which employs the method of hybrid optical flow and pattern matching velocimetry (HOP-V).[312] HOP-V assigns a velocity field, and hence a maximum image velocity (MIRV) to each GPI frame. Subjecting both the simulated and experimental GPI data to exactly the same analysis stream results in the curves labeled "MIRV" in Fig. 33. The curve labeled "V_E SOLT" is obtained by using a blob finder to create a database of blobs from the simulation data; this curve uses the radial **E**×**B** velocity measured at the intensity maximum of the brightest blob in each frame of the SOLT simulation. For the simulation data, this analysis concluded that the MIRV (image) velocity is indeed distributed similarly to the radial **E**×**B** velocity. Also, MIRV results for SOLT and NSTX data can be compared directly, and can be seen to show good agreement. Although tedious and difficult, validation of blob theory and simulations models will require more work of this type.

E. Modeling intermittent transport

It has been pointed out[3,83,84] that the intermittency associated with blob transport poses problems for transport codes based on averaged plasma parameters. In fact, in the limit of large skewness (small packing fraction), these parameters experience very strong fluctuations due to the passage of the blobs. The intermittency problem can be expressed by the following relation:[3] $< f(p) > \neq f(< p >)$, where f is a nonlinear function, p is a plasma state variable (e.g. n_e or T_e), and $< ... >$ is an average over z (the B field coordinate) and time. It is not easy to obtain a closure relation expressing $< f(p) >$ in terms of the average variables $< p >$ evolved in transport codes. Examples of nonlinear functions relevant to the SOL include blob convection, neutral ionization and radiation, sputtering, recycling, etc.

The specific example of impurity avalanche due to intermittent blobs was treated analytically in Ref. 83, and a more general discussion of the intermittent plasma transport problem was given in Ref. 84. In more recent work[313] the spatiotemporal features of blobs and ELMs were modeled using the 2D transport code UEDGE in a time-dependent mode. The model is based on multi-fluid simulation of an ensemble of plasma "macro-blobs" appropriately seeded in the edge plasma to simulate the experimental statistics of blobs. The model projects inherently 3D filamentary structures associated with blobs onto the 2D poloidal geometry. More work is needed to benchmark this approach against experimental data. All of this work is motivated by the need to take intermittency into account in order to understand the nonlinear physics of the SOL.

F. Finite T_i effects

All of the analytical blob theory and most of the blob simulations reviewed so far in this paper invoke the cold ion model, $T_i = 0$. This model is sufficient to describe the essential physics of blob theory (ion polarization drifts, parallel electron currents, sheaths and curvature drive, or most other charge-polarizing forces). While $T_i << T_e$ is realistic

in most small basic physics experiments, it is not realistic in the tokamak SOL where $T_e < T_i$ is typical. Finite ion temperature enters blob physics in several ways. First, ion pressure contributes to the interchange-curvature drive (Sec. III.A) so that $F \sim n m_i c_s^2 / R_c \propto (T_e + T_i)/R_c$. Second, in the Bohm sheath condition, which enters through $J_{||}$ in the vorticity equation Eq. (1), the ion flux at the sheath entrance must be generalized[314] to include the T_i dependence of $c_s \sim (T_e + \gamma_s T_i)^{1/2}/m_i^{1/2}$. These two effects are simple to include in the analytical scalings for the blob velocity. For example, in the sheath-connected regime, we find $v_{xCS} \propto L_{||} T_e (T_e + T_i)^{1/2}/(B^2 \delta^2 R)$ and in the electrostatic RX regime $v_{xRX} \propto n_e L_{||}^2 (T_e + T_i)/(T_e^{3/2} B^2 \delta^2 R)$ (where the ratio of specific heats γ_s is set to unity). Finite ion Larmor radius and gyro-vicious physics is more difficult to include. Terms describing these effects in the fluid approximation have been treated in BOUT code simulations [see e.g. Ref. 88], and are present kinetically in a PIC numerical study[103] of blobs. Additionally, analytical work has been carried out to obtain a reduced blob model retaining some finite T_i effects.[315] Seeded blob simulations were carried out with this model, which showed T_i-driven poloidal blob motion and modifications of the density-potential blob structure, but stability properties and blob speed were not qualitatively affected. More work is needed to fully explore the role of finite T_i on blob formation and dynamics, to understand how it limits the structure size on the ρ_i scale, and to address the impact of finite T_i and T_i gradients in the SOL when modeling tokamak experiments. This study has been inhibited both by the paucity of experimental data on the SOL T_i and by the complexity of modeling finite Larmor radius effects.

IX. Summary and discussion

This paper has reviewed the present state of research on blob formation, dynamics and transport mechanisms with an emphasis on comparing theory and experiment. Separate overviews of blob theory (Secs. II) and experiments (Sec. IV) were given, and

the results of analytic theory, computer simulations and experiments were compared for a number of topics related to blob structure and motion (Secs. III, V and VI) and the generation of blobs by turbulence (Sec. VII). The discussion emphasized topics for which there exists experimental data. For example, most of the discussion concerned the transport of particles by blobs, which is the aspect that has received the most theoretical and experimental attention; the corresponding transport of heat, momentum, and current was only briefly discussed (Sec. VIII).

This review shows that analytic blob theory has explained the basic experimental observations:

- the existence of higher-than-background density filaments (blobs) propagating outwards, and lower-than-background density filaments (holes) propagating inwards (Sec. III.A);
- the dipole charge polarization of blobs (compare Figs. 1, 14, and 15), which provides a robust mechanism for the observed convective transport and enhanced wall recycling in both toroidal and linear experiments;
- the characteristic pulse shape (steep rise and slow decay, compare Figs. 16 and 17);
- intermittent turbulence (compare Figs. 3 and 4) with order unity skewness of fluctuations in the SOL (compare Figs. 18 and 19) and non-Gaussian probability distribution function (compare Figs. 20 and 21);

Edge turbulence simulations, which model the blob creation process in the near SOL, agree qualitatively with experiments on the resulting statistical characterization of the edge and SOL: the intermittent, non-Gaussian transport which produces skewed probability distribution functions and characteristic radial profiles of skewness and kurtosis (Sec. V.B). Simulations and experiments also support the theoretical picture that blobs are born by saturation of the turbulence, with the blob birth zone located near the maximum logarithmic gradient of the pressure (i.e. near the maximum linear growth rate,

see Fig. 31). This picture is modified slightly by strong sheared flows, as discussed in Sec. VII.A.

Attempts to confirm the analytic scalings for the blob velocity as a function of blob size, collisionality and magnetic geometry have had mixed success (Sec. VI). Seeded blob simulations support the analytic theory scaling (e.g. the blob correspondence principle) but turbulence simulations and, even more so, experimental tests show a lot of scatter. This scatter is probably due to a number of factors. First, the underlying turbulent nature of the blobs ensures that the assumptions of the analytical theory, such as a circular shape with uniform temperature, are violated in practice, and the experimental blobs show a variety of shapes (see Figs. 5 - 11). Also, there are a number of unknown factors which can vary randomly from blob to blob in the simulation and experimental datasets, including initial vorticity, density "height" above background, structure parallel to **B**, the amount of sheared flow or background rotation encountered, contact with wall or divertor plate, etc.

The limitations on comparison of theory and experiment imposed by this scatter is one of the important conclusions of this review. However, it is also significant that in at least two experiments the measured velocities in a database of blobs are bounded by the theoretical prediction in a reasonable way (Sec. VI.B, Figs. 25 and 26), as is the multi-machine database (Fig. 27). Also, it is encouraging that the collisionality dependence of the blob velocity in the high-collisionality regime is consistent (at least qualitatively) with several experiments (Sec. VI.C).

Looking to the future, there are a number of promising areas for future work. One is the use of 2D and 3D simulation codes to model experimental data on edge and SOL turbulence and blob transport (see Secs. VI.C.2 and VIII.D). We listed a number of papers on simulation-experimental comparisons in Table V. Existing work in this area, particularly with regard to model validation in the presence of blobs and strong turbulence, can be viewed as exploratory rather than comprehensive. In the future, such

comparisons should include the radial profiles of density, temperature, fluxes and statistical quantities, as well as PDFs of the blob properties (size and velocity). For quantitative studies of tokamaks, STs and stellarators, the codes should take into account the 3D effects of magnetic geometry and X-points, although 2D codes remain very useful for understanding and for parameter studies. Experimental diagnostics to measure the parallel structure of the blobs along field lines should be developed. Possibly important extensions of present fluid models include modeling divertor plate sheath conditions, SOL ionization and radiation, wall recycling and kinetic effects.

To date, work on electromagnetic theory and simulation of blob-filaments is in an early stage, and extension of this work and its integration with edge MHD efforts to describe ELM formation and propagation in the SOL is of great scientific and practical importance.

Other topics that should receive additional attention in future years, and would benefit from theoretical-experimental collaboration, include the following, discussed briefly in earlier sections:

- turbulent and blob heat transport in edge and SOL and its relation to the density limit;
- blob transport of momentum and interaction with sheared flows, and especially simulations of these processes validated with high-resolution experimental data;
- parallel structure and dynamics of blobs and ELMs;
- blob and ELM transport of parallel current and other electromagnetic effects;
- X-point effects and divertor leg blobs;
- trigger mechanism for blob generation and release, and an understanding of the net blob generation rate (packing fraction);
- intermittency effects in transport code simulations.

In summary, our understanding of edge and SOL turbulence and the role of blob convective transport has improved greatly in the past ten years. There is enough

agreement between theory, simulations and experiments to encourage future work in this area. However, quantitative agreement has not yet been obtained in more than a few cases and will likely require further development in both the models and the experimental diagnostics.

Acknowledgments

The authors have benefited a great deal from the contributions of their collaborators in the course of research on blob physics and the writing of this review. In particular, we wish to thank the following people for a critical reading of the manuscript and for many useful suggestions (in alphabetical order): M. Agostini, R. H. Cohen, A. Diallo, O. Grulke, S. I. Krasheninnikov, R. J. Maqueda, V. Naulin, D. A. Russell and J. L. Terry. This work was supported by U.S. Department of Energy (DOE) under grants DE-FG02-97ER54392 and DE-AC02-09CH11466; however, such support does not constitute an endorsement by the DOE of the views expressed herein.

Appendix: List of abbreviations and symbols

BC	Boundary Condition
BD	Biorthogonal Decomposition
BES	Beam Emission Spectroscopy diagnostic
ELM	Edge Localized Mode
EM	Electromagnetic
ES	Electrostatic
GPI	Gas Puff Imaging diagnostic
LCFS	last closed flux surface
MHD	Magnetohydrodynamic
PDF	Probability distribution function
SOC	Self Organized Criticality
SOL	Scrape-off Layer

$\mathbf{B}$	background magnetic field
$\mathbf{b}$	$\mathbf{B}/B$
$\mathbf{F}$	charge-polarizing force
$\mathbf{E}$	electric field induced by charge polarization
R	major radius (for toroidal devices)
R_c	radius of curvature ($R_c \sim R$)
$\mathbf{g}$	effective gravity (force for interchange instability and blob motion)
x	radial coordinate
y	binormal (approximately poloidal) coordinate
z	coordinate along $\mathbf{b}$
n, n_e	density
T, T_e	electron temperature
κ	curvature of field lines
$J_{\|}$	parallel current
$L_{\|}$	blob parallel scale length, or correlation length
Φ	electrostatic potential
Φ_B	Bohm sheath potential ($\Phi_B \approx 3T_e$)
$\mathbf{v}_E$	$\mathbf{E}\times\mathbf{B}$ velocity
v_x	blob radial velocity (theory)
V_r	blob radial velocity (experiment)
v_*	$= c_s(\delta_*/R)^{1/2}$, characteristic blob speed
c_s	sound speed
ρ_s	sound Larmor radius
δ, δ_b	blob radius (or scale size in poloidal direction if blob is not circular)
δ_*	$= \rho_s^{4/5} L_{\|}^{2/5} / R^{1/5}$, characteristic blob scale size, most stable blob

$\hat{\delta}$	$= \delta_b / \delta_*$
Θ	$= \hat{\delta}^{5/2}$
Ω, Ω_i	ion gyro-frequency
Ω_e	electron gyro-frequency
<…>	statistical average
σ	standard deviation
S	skewness
K	kurtosis
E_{pol}	poloidal (y) electric field
Γ	particle flux
Λ	blob collisionality parameter, $= \nu_{ei} L_{\|} / (\Omega_e \rho_s) = (m_e / m_i)^{1/2} \nu_{*e}$
$\eta_{\|}$	parallel Spitzer resistivity = $1/\sigma_{\|}$
f_G	$\bar{n} / n_G$ = Greenwald parameter, normalized line density
β	$= 8\pi p / B^2$, normalized plasma pressure

References

[1] S. J. Zweben, J. A. Boedo, O. Grulke, C. Hidalgo, B. LaBombard, R. J. Maqueda, P. Scarin, and J. L. Terry, Plasma Phys. Controlled Fusion **49**, S1 (2007).

[2] B. A. Carreras, J. Nucl. Mater. **337-339**, 315 (2005).

[3] S. I. Krasheninnikov, D. A. D'Ippolito, and J. R. Myra, J. Plasma Phys. **74**, 679 (2008).

[4] O. E. Garcia, Plasma and Fusion Research **4**, 019 (2009).

[5] B. Lipschultz, X. Bonnin, G. Counsell, A. Kallenbach, A. Kukushkin, K. Krieger, A. Leonard, A. Loarte, R. Neu, R. A. Pitts, T. Rognlien, J. Roth, C. Skinner, J. L. Terry, E. Tsitrone, D. Whyte, S. Zweben, N. Asakura, D. Coster, R. Doerner, R. Dux, G. Federici, M. Fenstermacher, W. Fundamenski, P. Ghendrih, A. Herrmann, J. Hu, S. Krasheninnikov, G. Kirnev, A. Kreter, and B. L. V. Kurnaev, S. Lisgo, T. Nakano, N. Ohno, H.D. Pacher, J. Paley, Y. Pan, G. Pautasso, V. Philipps, V. Rohde, D. Rudakov, P. Stangeby, S. Takamura, T. Tanabe, Y. Yang and S. Zhu, Nucl. Fusion **47**, 1189 (2007).

[6] H. Zohm, Plasma Phys. Controlled Fusion **38**, 105 (1996).

[7] D. H. J. Goodall, J. Nucl. Mater. **111-112**, 11 (1982).

[8] S. J. Zweben, Phys. Fluids **28**, 974 (1985).

[9] M. Endler, H. Niedermeyer, L. Giannone, E. Holzhauer, A. Rudyj, G. Theimer, N. Tsois, and the ASDEX Team, Nucl. Fusion **35**, 1307 (1995).

[10] M. Endler, J. Nucl. Mater. **266-269**, 84 (1999).

[11] Y. Sarazin and P. Ghendrih, Phys. Plasmas **5**, 4214 (1998).

[12] G. Y. Antar, S. I. Krasheninnikov, P. Devynck, R. P. Doerner, E. M. Hollmann, J. A. Boedo, S. C. Luckhardt, and R. W. Conn, Phys. Rev. Lett. **87**, 065001 (2001).

[13] M. V. Umansky, S. I. Krasheninnikov, B. LaBombard, and J. L. Terry, Phys. Plasmas **5**, 3373 (1998).

[14] I. H. Hutchinson, R. Boivin, F. Bombarda, P. Bonoli, S. Fairfax, C. Fiore, J. Goetz, S. Golovato, R. Granetz, M. Greenwald, S. Horne, A. Hubbard, J. Irby, and B. L. B. LaBombard, E. Marmar, G. McCracken, M. Porkolab, J. Rice, J. Snipes, Y. Takase, J. Terry, S. Wolfe, C. Christensen, D. Garnier, M. Graf, T. Hsu, T. Luke, M. May, A. Niemczewski, G. Tinios, J. Schachter, and J. Urbahn, Phys. Plasmas **1**, 1511 (1994).

[15] S. I. Krasheninnikov, Phys. Lett. A **283**, 368 (2001).

[16] D. A. D'Ippolito, J. R. Myra, and S. I. Krasheninnikov, Phys. Plasmas **9**, 222 (2002).

[17] J. L. Luxon, Nucl. Fusion **42**, 614 (2002).

[18] J. A. Boedo, D. Rudakov, R. Moyer, S. Krasheninnikov, D. Whyte, G. McKee, G. Tynan, M. Schaffer, P. Stangeby, P. West, S. Allen, T. Evans, R. Fonck, E. Hollmann, and A. M. A. Leonard, G. Porter, M. Tillack, and G. Antar, Phys. Plasmas **8**, 4826 (2001).

[19] D. L. Rudakov, J. A. Boedo, R. A. Moyer, S. I. Krasheninnikov, A. W. Leonard, M. A. Mahdavi, G. R. McKee, G. D. Porter, P. C. Stangeby, J. G. Watkins, W. P. West, D. G. Whyte, and G. Antar, Plasma Phys. Controlled Fusion **44**, 717 (2002).

[20] S. J. Zweben, D. P. Stotler, J. L. Terry, B. LaBombard, M. Greenwald, M. Muterspaugh, C. S. Pitcher, K. Hallatschek, R. J. Maqueda, B. Rogers, J. L. Lowrance, V. J. Mastrocola, and G. F. Renda, Phys. Plasmas **9**, 1981 (2002).

[21] J. L. Terry, S. J. Zweben, K. Hallatschek, B. LaBombard, R. J. Maqueda, B. Bai, C. J. Boswell, M. Greenwald, D. Kopon, W. M. Nevins, C. S. Pitcher, B. N. Rogers, D. P. Stotler, and X. Q. Xu, Phys. Plasmas **10**, 1739 (2003).

[22] M. Agostini, S. J. Zweben, R. Cavazzana, P. Scarin, G. Serianni, R. J. Maqueda, and D. P. Stotler, Phys. Plasmas **14**, 102305 (2007).

[23] M. Ono, S. M. Kaye, Y.-K. M. Peng, G. Barnes, W. Blanchard, M. D. Carter, J. Chrzanowski, L. Dudek, R. Ewig, D. Gates, R. E. Hatcher, T. Jarboe, S. C. Jardin, and R. K. D. Johnson, M. Kalish, C.E. Kessel, H.W. Kugel, R. Maingi, R. Majeski, J. Manickam, B. McCormack, J. Menard, D. Mueller, B.A. Nelson, B.E. Nelson, C. Neumeyer, G. Oliaro, F. Paoletti, R. Parsells, E. Perry, N. Pomphrey, S. Ramakrishnan, R. Raman, G. Rewoldt, J. Robinson, A.L. Roquemore, P. Ryan, S. Sabbagh, D. Swain, E.J. Synakowski, M. Viola, M. Williams, J.R. Wilson and NSTX Team, Nucl. Fusion **40**, 557 (2000).

[24] D. L. Rudakov, J. A. Boedo, R. A. Moyer, P. C. Stangeby, J. G. Watkins, D. G. Whyte, L. Zeng, N. H. Brooks, R. P. Doerner, T. E. Evans, M. E. Fenstermacher, M. Groth, E. M. Hollmann, S. I. Krasheninnikov, C. J. Lasnier, A. W. Leonard, M. A. Mahdavi, G. R. McKee, A. G. McLean, A. Yu. Pigarov, W. R. Wampler, G. Wang, W. P. West, and C. P. C. Wong, Nucl. Fusion **45**, 1589 (2005).

[25] R. A. Pitts, W. Fundamenski, S. K. Erents, Y. Andrew, A. Loarte, C. Silva, and a. J.-E. contributors, Nucl. Fusion **46**, 82 (2006).

[26] M. Greenwald, Plasma Phys. Controlled Fusion **44**, R27 (2002).

[27] B. LaBombard, R. L. Boivin, M. Greenwald, J. Hughes, B. Lipschultz, D. Mossessian, C. S. Pitcher, J. L. Terry, S. J. Zweben, and the Alcator Group, Phys. Plasmas **8**, 2107 (2001).

[28] B. LaBombard, J. W. Hughes, D. Mossessian, M. Greenwald, B. Lipshultz, J. L. Terry, and the Alcator C-Mod Team, Nucl. Fusion **45**, 1658 (2005).

[29] D. A. D'Ippolito and J. R. Myra, Phys. Plasmas **13**, 062503 (2006).

[30] J. R. Myra, J. Boedo, B. Coppi, D. A. D'Ippolito, S. I. Krasheninnikov, B. P. LeBlanc, M. Lontano, R. Maqueda, D. A. Russell, D. P. Stotler, M. C. Varischetti, S. J. Zweben, and the NSTX Team, in Fusion Energy 2006 (Proc. 21st Int. Conf. Chengdu, 2006) (Vienna: IAEA) CD-ROM file TH/P6-21 and http://wwwnaweb.iaea.org/napc/physics/FEC/FEC2006/html/index.htm.

[31] J. R. Myra, D. A. Russell, and D. A. D'Ippolito, Phys. Plasmas **15**, 032304 (2008).

[32] A. Kirk, H. R. Wilson, G. F. Counsell, R. Akers, E. Arends, S. C. Cowley, J. Dowling, B. Lloyd, M. Price, M. Walsh, and the MAST Team, Phys. Rev. Lett. **92**, 245002 (2004).

[33] A. Kirk, N. B. Ayed, G. Counsell, B. Dudson, T. Eich, A. Herrmann, B. Koch, R. Martin, A. Meakins, S. Saarelma, R. Scannell, S. Tallents, M. Walsh, H. R. Wilson, and the MAST team, Plasma Phys. Cont. Fusion **48**, B433 (2006).

[34] J.L. Terry, I. Cziegler, A.E. Hubbard, J.A. Snipes, J.W. Hughes, M.J. Greenwald, B. LaBombard, Y. Lin, P. Phillips and S. Wukitch, J. Nucl. Mater. **363–365**, 994 (2007).

[35] R. J. Maqueda and R. Maingi, Phys. Plasmas **16**, 056117 (2009).
[36] P. Migliucci, V. Naulin, and JET EFDA Contributors, Phys. Plasmas **17**, 072507 (2010).
[37] G. Q. Yu and S. I. Krasheninnikov, Phys. Plasmas **10**, 4413 (2003).
[38] D. A. D'Ippolito, J. R. Myra, S. I. Krasheninnikov, G. Q. Yu, and A. Yu. Pigarov, Contrib. Plasma Phys. **44**, 205 (2004).
[39] S. I. Krasheninnikov, D. Ryutov, and G. Yu, J. Plasma Fusion Res. **6**, 139 (2004).
[40] D. A. Russell, D. A. D'Ippolito, J. R. Myra, W. M. Nevins, and X. Q. Xu, Phys. Rev. Lett. **93**, 265001 (2004).
[41] A. Y. Aydemir, Phys. Plasmas **12**, 62503 (2005).
[42] J. Madsen, J. Staerk, V. Naulin, J. J. Rasmussen, A. Kendl, O. E. Garcia, and A. H. Nielsen, *Proceedings of the 33nd EPS Plasma Physics Conference*. (19.23.6.2006, Roma, Italy) (2006).
[43] D. Ryutov, Phys. Plasmas **13**, 122307 (2006).
[44] D. Jovanović, P. K. Shukla, and F. Pegoraro, Phys. Plasmas **15**, 112305 (2008).
[45] G. S. Xu, V. Naulin, W. Fundamenski, J. Juul Rasmussen, A. H. Nielsen, and B. N. Wan, Phys. Plasmas 17, 022501 (2010).
[46] D. A. Russell, J. R. Myra and D. A. D'Ippolito, T. L. Munsat, Y. Sechrest, R. J. Maqueda, D. P. Stotler, S. J. Zweben, B. P. LeBlanc, Phys. Plasmas **18**, 022306 (2011).
[47] S. I. Krasheninnikov, A. I. Smolyakov, G. Yu, and T. K. Soboleva, Czech. J. of Phys. **55**, 307 (2005).
[48] J. R. Myra and D. A. D'Ippolito, Phys. Plasmas **12**, 092511 (2005).
[49] O. E. Garcia, N. H. Bian, and W. Fundamenski, Phys. Plasmas **13**, 082309 (2006).
[50] O. E. Garcia, V. Naulin, A. H. Nielsen, and J. J. Rasmussen, Phys. Scr. **T122**, 89 (2006).
[51] J. R. Myra, D. A. Russell, and D. A. D'Ippolito, Phys. Plasmas **13**, 112502 (2006).
[52] O. E. Garcia, R. A. Pitts, J. Horacek, A. H. Nielsen, W. Fundamenski, and e. al, J. Nucl. Mater. **363-365**, 575 (2007).
[53] D. A. Russell, J. R. Myra, and D. A. D'Ippolito, Phys. Plasmas **14**, 102307 (2007).
[54] S. I. Krasheninnikov, A. Yu. Pigarov, S. A. Galkin, G. Q. Yu, D. A. D'Ippolito, J. R. Myra, D. R. McCarthy, W. M. Nevins, T. D. Rognlien, X. Q. Xu, J. A. Boedo, D. L. Rudakov, M. J. Schaffer, W. P. West, and D. G. Whyte, *Proceedings of the 19th IAEA Fusion Energy Conference*, Lyon, France (IAEA, Vienna, 2003), paper IAEA-CN-94/TH/4-1 (2003)
[55] N. Bisai, A. Das, S. Deshpande, R. Jha, P. Kaw, A. Sen, and R. Singh, Phys. Plasmas **12**, 102515 (2005).
[56] J. R. Myra, Phys. Plasmas **14**, 102314 (2007).
[57] N. Bian, S. Benkadda, J.-V. Paulsen, and O. E. Garcia, Phys. Plasmas **10**, 671 (2003).
[58] O. E. Garcia, N. H. Bian, J.-V. Paulsen, S. Benkadda, and K. Rypdal, Plasma Phys. Controlled Fusion **45**, 919 (2003).
[59] O. E. Garcia, V. Naulin, A. H. Nielsen, and J. J. Rasmussen, Phys. Rev. Lett. **92**, 165003 (2004).
[60] N. Mahdizadeh, M. Ramisch, U. Stroth, C. Lechte, and B. D. Scott, Phys. Plasmas **11**, 3932 (2004).

[61] N. Bisai, A. Das, S. Deshpande, R. Jha, P. Kaw, A. Sen, and R. Singh, Phys. Plasmas **12**, 072520 (2005).
[62] O. E. Garcia, V. Naulin, A. H. Nielsen, and J. J. Rasmussen, Phys. Plasmas **12**, 062309 (2005).
[63] J. Anderson and E.-J. Kim, Phys. Plasmas **15**, 122303 (2008).
[64] J. A. Krommes, Phys. Plasmas **15**, 030703 (2008).
[65] S. Servidio, L. Primavera, V. Carbone, A. Noullez, and K. Rypdal, Phys. Plasmas **15**, 012301 (2008).
[66] I. Sandberg, S. Benkadda, X. Garbet, G. Ropokis, K. Hizanidis, and D. del-Castillo-Negrete, Phys. Rev. Lett. **103**, 165001 (2009).
[67] D. A. D'Ippolito and J. R. Myra, Phys. Plasmas **10**, 4029 (2003).
[68] D. A. D'Ippolito, J. R. Myra, D. A. Russell, and G. Q. Yu, Phys. Plasmas **11**, 4603 (2004).
[69] J. R. Myra, D. A. D'Ippolito, S. I. Krasheninnikov, and G. Q. Yu, Phys. Plasmas **11**, 4267 (2004).
[70] G. Q. Yu, S. I. Krasheninnikov, and P. N. Guzdar, Phys. Plasmas **13,** 042508 (2006).
[71] S. I. Krasheninnikov and A. I. Smolyakov, Phys. Plasmas **10**, 3020 (2003).
[72] S. I. Krasheninnikov, A. I. Smolyakov, and T. K. Soboleva, Phys. Plasmas **12**, 072502 (2005).
[73] R. H. Cohen and D. D. Ryutov, Contrib. Plasma Phys. **46**, 678 (2006).
[74] R. H. Cohen, B. LaBombard, D. D. Ryutov, J. L. Terry, M. V. Umansky, X. Q. Xu, and S. Zweben, Nucl. Fusion **47**, 612 (2007).
[75] D. D. Ryutov and R. H. Cohen, Contrib. Plasma Phys. **48**, 48 (2008).
[76] D. D. Ryutov and R. H. Cohen, Contrib. Plasma Phys. **44**, 168 (2004).
[77] M. V. Umansky, T. D. Rognlien, X. Q. Xu, R. H. Cohen, and W. M. Nevins, Contrib. Plasma Phys. **44**, 182 (2004).
[78] R.H.Cohen and D. D. Ryutov, Plasma Phys. Controlled Fusion **47**, 1187 (2005).
[79] P. Ghendrih, Y. Sarazin, G. Attuel, S. Benkadda, P. Beyer, G. Falchetto, C. Figarella, X. Garbet, V. Grandgirard, and M. Ottaviani, Nucl. Fusion **43,** 1013 (2003).
[80] S. I. Krasheninnikov and A. I. Smolyakov, Phys. Plasmas **14**, 102503 (2007).
[81] D. A. Russell, J. R. Myra, and D. A. D'Ippolito, Phys. Plasmas **16**, 122304 (2009).
[82] J.R. Myra, D.A. Russell, D.A. D'Ippolito, J-W. Ahn, R. Maingi, R.J. Maqueda, J. Boedo, D.P. Lundberg, D.P. Stotler, S.J. Zweben, M. Umansky, and the NSTX team, Phys. Plasmas **18**, 012305 (2011).
[83] D. A. D'Ippolito and J. R. Myra, Phys. Plasmas **15**, 082316 (2008).
[84] S. I. Krasheninnikov, A. Yu. Pigarov, T. K. Soboleva, and D. L. Rudakov, Phys. Plasmas **16**, 014501 (2009).
[85] B. Coppi, D. A. D'Ippolito, S. I. Krasheninnikov, M. Lontano, J. R. Myra, P. Nataf, and D. A. Russell, *Proceedings of the 33rd EPS Conference on Plasma Physics*, Rome, 19 - 23 June, 2006 ECA Vol.30I, O-4.017 (2006) (2006).
[86] W. Fundamenski, O. E. Garcia, V. Naulin, R. A. Pitts, A. H. Nielsen, J. J. Rasmussen, J. Horacek, J. P. Graves, and JET EFDA contributors, Nucl. Fusion **47**, 417 (2007).
[87] P. B. Parks, Nucl. Fusion **32**, 2137 (1992).

[88] X. Q. Xu, W. M. Nevins, R. H. Cohen, J. R.Myra, and P. B. Snyder, New J. Phys. **4**, 53 (2002).
[89] R. V. Shurygin, Plasma Physics Reports **32**, 799 (2006).
[90] G. T. A. Huysmans and O. Czarny, Nucl. Fusion **47**, 659 (2007).
[91] B. D. Dudson, N. B. Ayed, A. Kirk, H. R. Wilson, G. Counsell, X. Xu, M. Umansky, P. B. Snyder, B. Lloyd, and the MAST team, Plasma Phys. Controlled Fusion **50**, 124012 (2008).
[92] A. I. Smolyakov and S. I. Krasheninnikov, Phys. Plasmas **15**, 072302 (2008).
[93] O. E. Garcia, J. Horacek, R. A. Pitts, A. H. Nielsen, W. Fundamenski, V. Naulin, and J. J. Rasmussen, Nucl. Fusion **47**, 667 (2007).
[94] V. Naulin, W. Fundamenski., A.H. Nielsen, J. Juul Rasmussen, O.E. Garcia., B. Gonçalves, C. Hidalgo, M. Hron and JET-EFDA Contributors, *Proc. 21st Int. Conf. on Fusion Energy 2006* (Chengdu, 2006) (Vienna: IAEA) CD-ROM file TH/P6-22.
[95] R.A. Pitts, J. Horacek, W. Fundamenski, O.E. Garcia, A.H. Nielsen, M. Wischmeier, V. Naulin and J. Juul Rasmussen, J. Nucl. Mater. **363–365**, 505 (2007).
[96] S. Sugita, M. Yagi, S.-I. Itoh, and K. Itoh, Plasma Fus. Res. **3**, 040 (2008).
[97] S. Benkadda, T. Dudok de Wit, A. Sen, ASDEX team, and X. Garbet, Phys. Rev. Lett **73**, 3403 (1994).
[98] Y. Sarazin, P. Ghendrih, G. Attuel, C. Clément, X. Garbet, V. Grandgirard, M. Ottaviani, S. Benkadda, P. Beyer, N. Bian, and C. Figarella, J. Nucl. Mater. **313-316**, 796 (2003).
[99] P. Ghendrih, Y. Sarazin, G. Attuel, S. Benkadda, P. Beyer, G. Darmet, G. Falchetto, C. Figarella, X. Garbet, V. Grandgirard, and M. Ottaviani, J. Nucl. Mater. **337-339**, 347 (2005).
[100] O. E. Garcia, J. Horacek, R. A. Pitts, A. H. Nielsen, W. Fundamenski, J. P. Graves, V. Naulin, and J. J. Rasmussen, Plasma Phys. Controlled Fusion **48**, L1 (2006).
[101] D. A. D'Ippolito, J. Boedo, D. P. Lundberg, R. Maqueda, J. R. Myra, D. A. Russell, D. P. Stotler, and S. J. Zweben, *Plasma Physics and Controlled Nuclear Fusion Research 2008* (IAEA, Vienna, 2009), paper IAEA-CN-165-TH/P4-17.
[102] B. Li, B. N. Rogers, P. Ricci, and K. W. Gentle, Phys. Plasmas **16**, 082510 (2009).
[103] S. Ishiguro and H. Hasegawa, J. Plasma Phys. **72**, 1233 (2006).
[104] V. Naulin, T. Windisch, and O. Grulke, Phys. Plasmas **15**, 012307 (2008).
[105] A. Yu. Pigarov, S. I. Krasheninnikov, T. D. Rognlien, M. J. Schaffer, and W. P. West, Phys. Plasmas **9**, 1287 (2002).
[106] A. Yu. Pigarov, S. I. Krasheninnikov, W. P. West, T. D. Rognlien, J. A. Boedo, D. G. Whyte, C. J. Lasnier, T. W. Petrie, M. J. Schaffer, and J. G. Watkins, J. Nucl. Mater. **313-316**, 1076 (2003).
[107] A. Yu. Pigarov, S. I. Krasheninnikov, T. D. Rognlien, W. P. West, B. LaBombard, B. Lipschultz, R. Maingi, and V. Soukhanovskii, Contrib. Plasma Phys. **44**, 228 (2004).
[108] A. Yu. Pigarov, E. M. Hollmann, S. I. Krasheninnikov, T. D. Rognlien, and W. P. West, J. Nucl. Mater. **337-339**, 371 (2005).
[109] A. V. Nedospasov, Sov. J. Plasma Phys. **15**, 659 (1989).
[110] X. Garbet, L. Laurent, J.-P. Roubin, and A. Samain, Nucl. Fusion **31**, 967 (1991).
[111] J. R. Myra, D. A. D'Ippolito, X. Q. Xu, and R. H. Cohen, Phys. Plasmas **7**, 2290 (2000).

[112] J. R. Myra, D. A. D'Ippolito, X. Q. Xu, and R. H. Cohen, Phys. Plasmas **7**, 4622 (2000).
[113] X. Q. Xu, R. H. Cohen, T. D. Rognlien, and J. R. Myra, Phys. Plasmas **7**, 1951 (2000).
[114] M. N. Rosenbluth and C. L. Longmire, Annals Phys. **1**, 120 (1957).
[115] G. Tonetti, A. Heym, F. Hofmann, C. Hollenstein, J. Koechili, K. Lahlou, J. B. Lister, Ph. Marmillod, J. M. Mayor, J. C. Magnin, F. Marcus, and R. Rage, *Proceedings of the 16th Symposium on Fusion Technology*, London, U.K., edited by R. Hemsworth (North-Holland, Amsterdam, 1991), p. 587 (1991).
[116] P. T. Lang, K. Büchl, M. Kaufmann, R. S. Lang, V. Mertens, H. W. Müller, J. Neuhauser, and ASDEX Upgrade and NBI Teams, Phys. Rev. Lett. **79**, 1487 (1997).
[117] P. B. Parks, W. D. Sessions, and L. R. Baylor, Phys. Plasmas **7**, 1968 (2000).
[118] T. Huld, A. H. Nielsen, H. L. Phseli, and J. J. Rasmussen, Phys. Fluids B **3**, 1609 (1991).
[119] O. Grulke, T. Klinger, M. Endler, A. Piel, and the W7-AS Team, Phys. Plasmas **8**, 5171 (2001).
[120] M. Kotschenreuther, T. Rognlien, and P. Valanju, Fus. Eng. Design **72**, 169 (2004).
[121] O. E. Garcia, N. H. Bian, V. Naulin, A. H. Nielsen, and J. J. Rasmussen, Phys. Plasmas **12**, 090701 (2005).
[122] A. J. Wootton, B. A. Carreras, H. Matsumoto, K. McGuire, W. A. Peebles, C. P. Ritz, P. W. Terry, and S. J. Zweben, Phys. Fluids B **2**, 2879 (1990).
[123] C. Hidalgo, Plasma Phys. Controlled Fusion **37**, A53 (1995).
[124] J. A. Boedo, J. Nucl. Mater. **390–391**, 29 (2009).
[125] Y. H. Xu, S. Jachmich, R. R. Weynants, and the TEXTOR team, Plasma Phys. Controlled Fusion **47**, 1841 (2005).
[126] J. Cheng, L. W. Yan, W. Y. Hong, K. J. Zhao, T. Lan, J. Qian, A. D. Liu, H. L. Zhao, Yi Liu, Q. W. Yang, J. Q. Dong, X. R. Duan and Y. Liu, Plasma Phys. Controlled Fusion **52**, 055003 (2010).
[127] G. Y. Antar, G. Counsell, and J.-W. Ahn, Phys. Plasmas **12**, 082503 (2005).
[128] "Intermittency in the scrape-off layer of the National Spherical Torus Experiment during H-mode confinement," R.J. Maqueda, D.P. Stotler, S.J. Zweben and The NSTX team, J. Nucl. Mater. (in press, 2010).
[129] J. A. Boedo, D. L. Rudakov, R. A. Moyer, G. R. McKee, R. J. Colchin, M. J. Schaffer, P. G. Stangeby, W. P. West, S. L. Allen, T. E. Evans, R. J. Fonck, E. M. Hollmann, S. Krasheninnikov, A. W. Leonard, W. Nevins, M. A. Mahdavi, G. D. Porter, G. R. Tynan, D. G. Whyte, and X. Xu, Phys. Plasmas **10**, 1670 (2003).
[130] T. A. Carter, Phys. Plasmas **13**, 10701 (2006).
[131] N. Katz, J. Egedal, W. Fox, A. Le, and M. Porkolab, Phys. Rev. Lett. **101**, 015003 (2008).
[132] I. Furno, B. Labit, M. Podestà, A. Fasoli, S. H. Müller, F. M. Poli, P. Ricci, C. Theiler, S. Brunner, A. Diallo, and J. Graves, Phys. Rev. Lett. **100**, 055004 (2008).
[133] J. A. Boedo, D. L. Rudakov, R. J. Colchin, R. A. Moyer, S. Krasheninnikov, D. G. Whyte, G. R. McKee, G. Porter, M. J. Schaffer, P. G. Stangeby, W. P. West, S. L. Allen, and A. W. Leonard, J. Nucl. Mater. **313-316**, 813 (2003).

[134] S. J. Zweben, R. J. Maqueda, D. P. Stotler, A. Keesee, J. Boedo, C. E. Bush, S. M. Kaye, B. LeBlanc, J. L. Lowrance, V. J. Mastrocola, R. Maingi, N. Nishino, G. Renda, D. W. Swain, J. B. Wilgen, and the NSTX Team, Nucl Fusion **44**, 134 (2004).
[135] J. R. Myra, D. A. D'Ippolito, D. P. Stotler, S. J. Zweben, B. P. LeBlanc, J. E. Menard, R. Maqueda, and J. Boedo, Phys. Plasmas **13**, 092509 (2006).
[136] R.J. Maqueda, D.P. Stotler and the NSTX Team, Nucl. Fusion **50**, 075002 (2010).
[137] J. L. Terry, N. P. Basse, I. Cziegler, M. Greenwald, O. Grulke, B. LaBombard, S. J. Zweben, E. M. Edlund, J. W. Hughes, L. Lin, Y. Lin, M. Porkolab, M. Sampsell, B. Veto, and S. J. Wukitch, Nucl. Fusion **45**, 1321 (2005).
[138] O. Grulke, J. L. Terry, B. LaBombard, and S. J. Zweben, Phys. Plasmas **13**, 012306 (2006).
[139] J. L. Terry, B. LaBombard, B. Lipschultz, M. J. Greenwald, J. E. Rice, and S. J. Zweben, Fusion Science and Tech **51**, 342 (2007).
[140] J. L. Terry, S. J. Zweben, M. V. Umansky, I. Cziegler, O. Grulke, B. LaBombard, and D. P. Stotler, J. Nucl. Mater. **390**, 339 (2009).
[141] "Parallel correlation of turbulent fluctuations in the SOL of Alcator C-Mod," O. Grulke, J.L. Terry, B. LaBombard, I. Cziegler, and S.J. Zweben, *Proceedings of the 37th EPS Conference on Plasma Physics*, (EPS, Dublin, 2010), paper P1-1036.
[142] B. Gonçalves, C. Hidalgo, C. Silva, M. A. Pedrosa, and K. Erents, J. Nucl. Mater. **337-339**, 376 (2005).
[143] C. Silva, B. Gonçalves, C. Hidalgo, M. A. Pedrosa, W. Fundamenski, and et al, Journal of Nuclear Mater. **390**, 355 (2009).
[144] G. S. Xu, V. Naulin, W. Fundamenski, C. Hidalgo, J. A. Alonso, C. Silva, B. Goncalves, A. H. Nielsen, J. J. Rasmussen, S. I. Krasheninnikov, B. N. Wan, M. Stamp, and JET EFDA Contributors, Nucl. Fusion **49**, 092002 (2009).
[145] Y. Xu, R. R. Weynants, S. Jachmich, M. V. Schoor, M. Vergote, P. Peleman, M. W. Jakubowski, M. Mitri, D. Reiser, B. Unterberg, and K. H. Finken (the TEXTOR team), Phys. Rev. Lett. **97**, 165003 (2006).
[146] Y. Xu, R. R. Weynants, M. V. Schoor, and S. J. M. Vergote, M. W. Jakubowski, M. Mitri, O. Schmitz, B. Unterberg, P. Beyer, D. Reiser, K. H. Finken, M. Lehnen and the TEXTOR Team, Nucl. Fusion **49**, 035005 (2009).
[147] Y. Xu, R. R. Weynants, M. V. Schoor, and S. J. e. a. M. Vergote, J. Nucl. Mater. **390-391**, 372 (2009).
[148] N. Asakura, Y. Koide, and K. Itami, J. Nucl. Mater. **220-222**, 104 (1995).
[149] N. Asakura, N. Ohno, H. Tanaka, H. Kawashima, and T. Nakano, J. Nucl. Mater. **390-391**, 364 (2009).
[150] H. Tanaka, N. Ohno, N. Asakura, Y. Tsuji, H. Kawashima, S. Takamura, Y. Uesugi, and the JT-60U Team, Nucl. Fusion **49**, 065017 (2009).
[151] P. Devynck, P. Ghendrih, and Y. Sarazin, Phys. Plasmas **12**, 050702 (2005).
[152] M. Farge, K. Schneider, and P. Devynck, Phys. Plasmas **13**, 042304 (2006).
[153] J. P. Gunn, C. Boucher, M. Dionne, I. Ďuran, V. Fuchs, T. Loarer, I. Nanobashvili, R. Pánek, J.-Y. Pascal, F. Saint-Laurent, J. Stöckel, T. V. Rompuy, R. Zagórski, J. Adámek, J.

Bucalossi, G. Ciraolo, and P. D. R. Dejarnac, Ph. Ghendrih, P. Hertout, M. Hron, P. Moreau, B. Pégourié, F. Rimini, Y. Sarazin, A. Sarkissian, G. Van Oost, *Plasma Physics and Controlled Nuclear Fusion Research 2006* (IAEA, Vienna, 2007), paper IAEA-CN-149-EX/P4-9.

154 I. Nanobashvili, J. P. Gunn, and P. Devynck, J. Nucl. Mater. **363-365**, 622 (2007).

155 N. Fedorczak, J. P. Gunn, P. Ghendrih, and A. P. P. Monier-Garbet, J. Nucl. Mater. **390-391**, 368 (2009).

156 J. P. Graves, J. Horacek, R. A. Pitts, and K. I. Hopcraft, Plasma Phys. Controlled Fusion **47**, L1 (2005).

157 O. E. Garcia, R. A. Pitts, J. Horacek, J. Madsen, V. Naulin, A. H. Nielsen, and J. J. Rasmussen, Plasma Phys. Controlled Fusion **49**, B47 (2007).

158 G. S. Kirnev, V. P. Budaev, S. A. Grashin, E. V. Gerasimov, and L. N. Khimchenko, Plasma Phys. Controlled Fusion **46**, 621 (2004).

159 G. S. Kirnev, V. P. Budaev, S. A. Grashin, E. V. Gerasimov, and L. N. Khimchenko, J. Nucl. Mater. **337-339**, 352 (2005).

160 G. S. Kirnev, V. P. Budaev, S. A. Grashin, L. N. Khimchenko, and D. V. Sarytchev, Nucl. Fusion **45**, 459 (2005).

161 G. Y. Antar, G. Counsell, J.-W. Ahn, Y. Yang, M. Price, A. Tabasso, and A. Kirk, Phys. Plasmas **12**, 032506 (2005).

162 B. Hnat, B. D. Dudson, R. O. Dendy, G. F. Counsell, A. Kirk, and the MAST team, Nucl. Fusion **48**, 085009 (2008).

163 N. Ben-Ayed, A. Kirk, B. Dudson, S. Tallents, R. G. L. Vann, H. R. Wilson, and the MAST team, Plasma Phys. Controlled Fusion **51**, 035016 (2009).

164 M. V. A. P. Heller, Z. A. Brasilio, I. L. Caldas, and J. P. J. Stockel, Phys. Plasmas **6**, 846 (1999).

165 E. Martines, M. Hron, and J. Stockel, Plasma Phys. Controlled Fusion **44**, 351 (2002).

166 P. Devynck, G. Bonhomme, E. Martines, J. Stöckel, G. Van Oost, I. Voitsekhovitch, J. Adámek, A. Azeroual, F. Doveil, I. Duran, E. Gravier, J. Gunn, and M. Hron, Plasma Phys. Controlled Fusion **47**, 269 (2005).

167 P. Devynck, J. Brotankova, P. Peleman, M. Spolaore, H. Figueiredo, M. Hron, G. Kirnev, E. Martines, J. Stöckel, G. Van Oost, and V. Weinzettl, Phys. Plasmas **13**, 102505 (2006).

168 G. Y. Antar, M. Tsalas, E. Wolfrum, V. Rohde, and the ASDEX Upgrade Team, Plasma Phys. Controlled Fusion **50**, 095012 (2008).

169 B. Nold, G D Conway, T Happel, H W Müller, M Ramisch,V Rohde, U Stroth and the ASDEX Upgrade Team, Plasma Phys. Controlled Fusion **52**, 065005 (2010).

170 R. Jha, P. K. Kaw, S. K. Mattoo, C. V. S. Rao, Y. C. Saxena, and the ADITYA team, Phys. Rev. Lett. **69**, 1375 (1992).

171 R. Jha, S. K. Mattoo, and Y. C. Saxena, Phys. Plasmas **4**, 2982 (1997).

172 B. K. Joseph, R. Jha, P. K. Kaw, S. K. Mattoo, C. V. S. Rao, Y. C. Saxena, and the Aditya Team, Phys. Plasmas **4**, 4292 (1997).

173 R. Jha, P. K. Kaw, D. R. Kulkarni, and J. C. Parikh, Phys. Plasmas **10**, 699 (2003).

[174] S. K. Saha and S. Chowdhury, Phys. Plasmas **13**, 092512 (2006).
[175] S. K. Saha and S. Chowdhury, Phys. Plasmas **15**, 012305 (2008).
[176] V. Budaev, Y. Kikuchi, Y. Uesugi, and S. Takamura, Nucl. Fusion **44**, S108 (2004).
[177] G. S. Xu, B. N. Wan, W. Zhang, Q. W. Yang, L. Wang, and Y. Z. Wen, Phys. Plasmas **13**, 102509 (2006).
[178] L. Dong, L. Wang, C. Feng, Z. Li, Q. Zhao, and G. Wang, Phys. Rev. E **57**, 5929 (1998).
[179] "Acceleration of Blob driven by Helical Instability in a Simple Magnetic Configuration in QUEST," H. Q. Liu, K. Hanadab, N. Nishinoc, R. Ogataa, M. Ishiguroa, H. Zushib, K. Nakamurab, M. Sakamotob, H. Ideib, A. Fujisawab, M. Hasegawab, Y. Higashizonob, S. Kawasakib, H. Nakashimab, A. Higashijimab, and QUEST Group, J. Nucl. Mater. (in press, 2010).
[180] N. Ohno, S. Masuzaki, H. Miyoshi, S. Takamura, V. P. Budaev, and et al., Contrib. Plasma Phys. **467-469**, 692 (2006).
[181] K. Tanaka, C. Michael, A. L. Sanin, L. N. Vyacheslavov, K. Kawahata, and et al., Nucl. Fusion **46**, 110 (2006).
[182] J. M. Dewhurst, B. Hnat, N. Ohno, R. O. Dendy, S. Masuzake, T. Morisake, and A. Komori, Plasma Phys. Controlled Fusion **50**, 095013 (2008).
[183] N. P. Basse, S. Zoletnik, P. K. Michelsen, and the W7-AS Team, Phys. Plasmas **12**, 012507 (2005).
[184] T. Happel, F. Greiner, N. Mahdizadeh, B. Nold, M. Ramisch, and U. Stroth, Phys. Rev. Lett. **102**, 255001 (2009).
[185] J. A. Alonso, S. J. Zweben, P. Carvalho, J. L. de Pablos, E. de la Cal, C. Hidalgo, T. Klinger, B. P. v. Milligen, R. J. Maqueda, M. A. Pedrosa, C. Silva, M. Spolaore, H. Thomsen, and the TJ-II team, Plasma Phys. Controlled Fusion **48**, B465 (2006).
[186] J. A. Alonso, S. J. Zweben, J. L. de Pablos, E. de la Cal, C. Hidalgo, T. Klinger, B. Ph. Van Milligen, M. A. Pedrosa, C. Silva, H. Thomsen, Fusion Sci. Tech **50**, 301 (2006).
[187] V. Antoni, V. Carbone, R. Cavazzana, G. Regnoli, N. Vianello, E. Spada, L. Fattorini, E. Martines, G. Serianni, M. Spolaore, L. Tramontin, and P. Veltri, Phys. Rev. Lett. **87**, 045001 (2001).
[188] M. Spolaore, V. Antoni, R. Cavazzana, G. Regnoli, G. Serianni, E. Spada, N. Vianello, H. Bergsåker, and J. R. Drake, Phys. Plasmas **9**, 4110 (2002).
[189] M. Spolaore, V. Antoni, E. Spada, H. Bergsaker, R. Cavazzana, J. R. Drake, E. Martines, G. Regnoli, G. Serianni, and N. Vianello, Phys. Rev. Lett. **93**, 215003 (2004).
[190] F. Sattin, P. Scarin, M. Agostini, R. Cavazzana, G. Serianni, M. Spolaore, and N. Vianello, Plasma Phys. Controlled Fusion **48**, 1033 (2006).
[191] M. Agostini, P. Scarin, R Cavazzana, F Sattin, G Serianni, M Spolaore and N Vianello, Plasma Phys. Controlled Fusion **51**, 105003 (2009).
[192] M. Spolaore, N. Vianello, M. Agostini, R. Cavazzana, E. Martines, G. Serianni, P. Scarin, E. Spada, M. Zuin and V. Antoni, J. Nucl. Mater. **390-391**, 448 (2009).
[193] M. Spolaore, N. Vianello, M. Agostini, R. Cavazzana, E. Martines, P. Scarin, G. Serianni, E. Spada, M. Zuin, and V. Antoni, Phys. Rev. Lett. **102**, 165001 (2009).

[194] V. Antoni, H. Bergsåker, R. Cavazzana, V. Carbone, J. Drake, E. Martines, G. Regnoli, G. Serianni, E. Spada, M. Spolaore, and N. Vianello, Contrib. Plasma Phys. **44**, 458 (2004).
[195] N. Vianello, M. Spolaore, G. Serianni, H. Bergsåker, V. Antoni and J.R. Drake, Plasma Phys. Controlled Fusion **44**, 2513 (2002).
[196] R. Cavazzana, G. Serianni, P. Scarin, M. Agostini, N. Vianello, Y. Yagi, H. Koguchi, S. Kiyama, H. Sadadita, and Y. Hirano, Plasma Phys. Controlled Fusion **49**, 129 (2007).
[197] M. Agostini, R. Cavazzana, P. Scarin, G. Serianni, Y. Yagi, H. Koguchi, S. Kiyama, H. Sakakita, and Y. Hirano, Plasma Phys. Controlled Fusion **50**, 095004 (2008).
[198] A. Fasoli, B. Labit, M. McGrath, S. H. Müller, G. Plyushchev, M. Podestà, and F. M. Poli, Phys. Plasmas **13**, 055902 (2006).
[199] S. H. Müller, A. Diallo, A. Fasoli, I. Furno, B. Labit, G. Plyushchev, M. Podestà, and F. M. Poli, Phys. Plasmas **13**, 100701 (2006).
[200] B. Labit, A. Diallo, A. Fasoli, I. Furno, D. Iraji, S. H. Müller, G. Plyushchev, M. Podestà, F. M. Poli, P. Ricci, C. Theiler, and J. Horaček, Plasma Phys. Controlled Fusion **49**, B281 (2007).
[201] B. Labit, I. Furno, A. Fasoli, A. Diallo, S. H. Müller, G. Plyushchev, M. Podestà, and F. M. Poli, Phys. Rev. Lett. **98**, 255002 (2007).
[202] S. H. Müller, A. Diallo, A. Fasoli, I. Furno, B. Labit, and M. Podestà, Phys. Plasmas **14**, 110704 (2007).
[203] A. Diallo, A. Fasoli, I. Furno, B. Labit, M. Podestà, and C. Theiler, Phys. Rev. Lett. **101**, 115005 (2008).
[204] I. Furno, B. Labit, A. Fasoli, F. M. Poli, P. Ricci, C. Theiler, S. Brunner, A. Diallo, J. P. Graves, M. Podestà, and S. H. Müller, Phys. Plasmas **15**, 055903 (2008).
[205] M. Podestà, A. Fasoli, B. Labit, I. Furno, P. Ricci, F. M. Poli, A. Diallo, S. H. Müller, and C. Theiler, Phys. Rev. Lett. **101**, 045001 (2008).
[206] C. Theiler, A. Diallo, A. Fasoli, I. Furno, B. Labit, M. Podestà, F. M. Poli, and P. Ricci, Phys. Plasmas **15**, 042303 (2008).
[207] S. H. Müller, C. Theiler, A. Fasoli, I. Furno, B. Labit, G. R. Tynan, M. Xu, Z. Yan, and J. H.Yu, Plasma Phys. Controlled Fusion **51**, 055020 (2009).
[208] C. Theiler, I. Furno, P. Ricci, A. Fasoli, B. Labit, S. H. Müller, and G. Plyushchev, Phys. Rev. Lett. **103**, 065001 (2009).
[209] A. Fasoli, A. Burckel, L. Federspiel, I. Furno, K. Gustafson, D. Iraji, B. Labit, J. Loizu, G. Plyushchev, P. Ricci, C. Theiler, A. Diallo, S. H. Mueller, M. Podestà and F. Poli, Plasma Phys. Controlled Fusion **52**, 124020 (2010).
[210] C. Riccardi and Å. Fredriksen, Phys. Plasmas **8**, 199 (2001).
[211] Å. Fredriksen, C. Riccardi, L. Cartegni, and H. Pecseli, Plasma Phys. Controlled Fusion **45**, 721 (2003).
[212] F. J.Oynes, O.-M. Olsen, H. L. Pécseli, Å. Fredriksen, and K. Rypdal, Phys. Rev. E **57**, 2242 (1998).
[213] O. Grulke, F. Greine, T. Klinger, and A. Piel, Plasma Phys. Controlled Fusion **43**, 525 (2001).

[214] O. Grulke and T. Klinger, New Journal of Physics **4**, 67 (2002).
[215] R. Barni and C. Riccardi, Plasma Phys. Controlled Fusion **51**, 085010 (2009).
[216] T. A. Carter and J. E. Maggs, Phys. Plasmas **16**, 012304 (2009).
[217] D. C. Pace, M. Shi, J. E. Maggs, G. J. Morales, and T. A. Carter, Phys. Plasmas **15**, 122304 (2008).
[218] F. Brochard, T. Windisch, O. Grulke, and T. Klinger, Phys. Plasmas **13**, 122305 (2006).
[219] T. Windisch, O. Grulke, and T. Klinger, Phys. Plasmas **13**, 122303 (2006).
[220] G. N. Kervalishvili, R. Kleiber, R. Schneider, B. D. Scott, O. Grulke, and T. Windisch, Contrib. Plasma Phys. **48**, 32 (2008).
[221] T. Windisch, O. Grulke, and T. Klinger, J. Nucl. Mater. **390-391**, 395 (2009).
[222] G. Y. Antar, J. H. Yu, and G. Tynan, Phys. Plasmas **14**, 022301 (2007).
[223] G. Y. Antar, Phys. Plasmas **10**, 3629 (2003).
[224] T. Pierre, A. Escarguel, D. Guyomarc'h, R. Barni, and C. Ricardi, Phys. Rev. Lett. **92**, 065004 (2004).
[225] R. Barni, C. Riccardi, Th. Pierre, G. Leclert, A. Escarguel, D. Guyomarc'h and K Quotb, New J. Physics **7**, 225 (2005).
[226] S. Magni, H. E. Roman, R. Barni, C. Riccardi, T. Pierre, and D. Guyomarc'h, Phys. Rev. E **72**, 026403 (2005).
[227] H. Tanaka, N. Ohno, Y. Tsuji, and S. Kajita, Controlled Plasma Phys. **50**, 256 (2010).
[228] T. Yamada, S.-I. Itoh, T. Maruta, N. Kasuya, Y. Nagashima, S. Shinohara, K. Terasaka, M.Yagi, S. Inagaki, Y.Kawai, A. Fujisawa, and K. Itoh, Nature Physics **4**, 721 (2008).
[229] A. H. Nielsen, H. L. Pecseli, and J. J. Rasmussen, Phys. Plasmas **3**, 1530 (1996).
[230] B. LaBombard, Phys. Plasmas **9**, 1300 (2002).
[231] A. Huber, U. Samm, B. Schweer and Ph. Mertens, Plasma Phys. Controlled Fusion **47**, 409 (2005).
[232] B. Kurzan, L. D. Horton, H. Murmann, J. Neuhauser, W. Suttrop and the ASDEX Upgrade Team, Plasma Phys. Controlled Fusion **49**, 825 (2007).
[233] Y. Hamada, T. Watari, A. Nishizawa, K. Narihara, Y. Kawasumi, T. Ido, M. Kojima, and K. Toi (JIPPT-IIU Group), Phys. Rev. Lett. **96**, 115003 (2006).
[234] T. Peacock and J. Dabin, Chaos **20**, 017501 (2010).
[235] V. Antoni, V. Carbone, E. Martines, G. Regnoli, G. Serianni, N. Vianello and P. Veltri, Europhys. Letter **54**, 51 (2001).
[236] "Estimate of convective radial transport due to SOL turbulence as measured by GPI in Alcator C-Mod," S.J. Zweben, J.L. Terry, B. LaBombard, M.Agostini, M. Greenwald, O. Grulke, J.W. Hughes, D.A. D'Ippolito, S.I. Krasheninnikov, J.R. Myra, D.A. Russell, D.P. Stotler, M. Umansky, J. Nucl. Mater. (in press, 2010).
[237] E. Spada, V. Carbone, R. Cavazzana, L. Fattorini, G. Regnoli, N. Vianello, V. Antoni, E. Martines, G. Serianni, M. Spolaore, and L. Tramontin, Phys. Rev. Lett. **86**, 3032 (2001).
[238] V. P. Budaev, S. Takamura, N. Ohno, and S. Masuzaki, Nucl. Fusion **46**, S181 (2006).
[239] V. P. Budaev, N. Ohno, S. Masuzaki, T. Morisaki, A. Komori, and S. Takamura, Nucl. Fusion **48**, 024014 (2008).

[240] N. Mahdizadeh, F. Greiner, T. Happel, A. Kendl, M. Ramisch, B.D. Scott and U. Stroth, Plasma Phys. Cont. Fusion **49**, 1005 (2007).
[241] P. Piovesan, A. Almagri, B. E. Chapman, D. Craig, L. Marrelli, P. Martin, S. C. Prager, and J. S. Sarff, Nucl. Fusion **48**, 095003 (2008).
[242] I. Nanobashvili, P. Devynck, J. P. Gunn, S. Nanobashvili, J. Stöckel, and G. Van Oost, Phys. Plasmas **16**, 022309 (2009).
[243] G. Y. Antar, G. Counsell, Y. Yu, B. Labombard, and P. Devynck, Phys. Plasmas **10**, 419 (2003).
[244] F. Sattin, M. Agostini, P. Scarin, N. Vianello, R. Cavazzana, L. Marrelli, G. Serianni, S. J. Zweben, R. J. Maqueda, Y. Yagi, H. Sakakita, H. Koguchi, S. Kiyama, Y. Hirano, and J. L. Terry, Plasma Phys. Controlled Fusion **51**, 055013 (2009).
[245] B. A. Carreras, B. van Milligen, M. A. Pedrosa, R. Balbın, C. Hidalgo, D. E. Newman, E. Sánchez, M. Frances,I. Garcıa-Cortés, J. Bleuel, M. Endler, S. Davies, and G. F. Matthews, Phys. Rev. Lett. **80**, 4438 (1998).
[246] G. Serianni, M. Agostini, V. Antoni, R. Cavazzana, E. Martines, F. Sattin, P. Scarin, E. Spada, M. Spolaore, N. Vianello, and M. Zuin, Plasma Phys. Controlled Fusion **49**, B267 (2007).
[247] K. Bodi, S. I. Krasheninnikov, and A. I. Smolyakov, Phys. Plasmas **15**, 102304 (2008).
[248] J.A. Boedo, R.J. Maqueda, D.L. Rudakov, G.R. McKee, H. Kugel, R. Maingi, N. Crocker, R.A. Moyer, V.A. Soukhanovskii, J. Menard, J.G. Watkins, S.J. Zweben , D.A. D'Ippolito, T.E. Evans, M.E. Fenstermacher, M. Groth, E.M. Hollmann, C.J. Lasnier, J.R. Myra, L.A. Roquemore, W.P. West, and L. Zeng, in *Plasma Physics and Controlled Nuclear Fusion Research* 2006 (IAEA, Vienna, 2007), paper IAEA-CN-149- EX/P4-2.
[249] C. Hidalgo, B. Gonçalves, M. A. Pedrosa, J. Castellano, K. Erents, A. L. Fraguas, M. Hron, J. A. Jiménez, G. F. Matthews, B. van Milligen and C. Silva, Plasma Phys. Controlled Fusion **44**, 1557 (2002).
[250] B. A. Carreras, C. Hidalgo, E. Sanchez, M. A. Pedrosa, R. Balbın, I. Garcıa-Cortes, B. van Milligen, D. E. Newman and V. E. Lynch, Phys. Plasmas **3**, 2664 (1996)
[251] V. Naulin, O.E. Garcia, A.H. Nielsen, J. Juul Rasmussen, Phys. Letters A **321**, 355 (2004).
[252] F.Sattin, M. Agostini, R. Cavazzana, G. Serianni, P. Scarin and N. Vianello, Physica Scripta **79**, 045006 (2009).
[253] E. Kim and J. Anderson, Phys. Plasmas **15**, 114506 (2008).
[254] D. Farina, R. Pozzoli, and D. D. Ryutov, Nucl. Fusion **33**, 1315 (1993).
[255] J.W. Connor, Plasma Phys. Controlled Fusion **40**,191 (1998).
[256] K. Kamiya, N. Asakura, J. Boedo, T. Eich, G. Federici, M. Fenstermacher, K. Finken, A. Herrmann, J. Terry, A. Kirk, B. Koch, A. Loarte, R. Maingi, R. Maqueda, E. Nardon, N. Oyama and R. Sartori, Plasma Phys. Controlled Fusion **49**, S43 (2007).
[257] W. Fundamenski, V. Naulin, T. Neukirch, O. E. Garcia and J. Juul Rasmussen, Plasma Phys. Controlled Fusion **49**, R43 (2007).
[258] A. Schmid, A. Herrmann, H. W. Müller, and the ASDEX Upgrade Team, Plasma Phys. Controlled Fusion **50**, 045007 (2008).

[259] V. Rozhansky and A. Kirk, Plasma Phys. Controlled Fusion **50**, 025008 (2008).
[260] B. N. Rogers and J. F. Drake, Phys. Rev. Lett. **79**, 229 (1997).
[261] B. Scott, Plasma Phys. Controlled Fusion **39**, 1635 (1997).
[262] B. N. Rogers, J. F. Drake, and A. Zeiler, Phys. Rev. Lett. **81**, 4396 (1998).
[263] X. Q. Xu, W. M. Nevins, T. D. Rognlien, R. H. Bulmer, M. Greenwald, A. Mahdavi, L. D. Pearlstein, and P. Snyder, Phys. Plasmas **10**, 1773 (2003).
[264] B. Lipschultz, D. Whyte, and B. LaBombard, Plasma Phys. Controlled Fusion **47**, 1559 (2005).
[265] B. LaBombard, M. V. Umansky, R. L. Boivin, J. A. Goetz, J. Hughes, B. Lipschultz, D. Mossessian, C. S. Pitcher, J. L. Terry, and A. Group, Nucl. Fusion **40**, 2041 (2000).
[266] "Linear eigenvalue code for edge plasma in full tokamak X-point geometry," D. A. Baver, J. R. Myra and M.V. Umansky, Lodestar Report #LRC-10-137, submitted to Comp. Physics Comm. (2010).
[267] J. Terry, private communication (2010).
[268] H. Berk, D. D. Ryutov, and Y. A. Tsidulko, JETP Lett. **52**, 23 (1990).
[269] H. L. Berk, D. D. Ryutov, and Y. A. Tsidulko, Phys. Fluids B **3**, 1346 (1991).
[270] H. L. Berk, R. H. Cohen, D. D. Ryutov, Yu.A. Tsidulko and X.Q. Xu, Nucl. Fusion **33**, 263 (1993).
[271] X. S. Lee, P. J. Catto, and R. E. Aamodt, Phys. Fluids **25**, 1491 (1982).
[272] J. Horacek, J. Adamek, H.W. Müller, J. Seidl, A.H. Nielsen, V. Rohde, F. Mehlmann, C. Ionita, E. Havlíčková and the ASDEX Upgrade Team, Nucl. Fusion 50, 105001 (2010).
[273] J. A. Boedo, D. L. Rudakov, E. Hollmann, D. S. Gray, K. H. Burrell, R. A. Moyer, G. R. McKee, R. Fonck, P. C. Stangeby, T. E. Evans, P. B. Snyder, A. W. Leonard, M. A. Mahdavi, M. J. Schaffer, and M. E. F. W. P. West, M. Groth, S. L. Allen, C. Lasnier, G. D. Porter, N. S. Wolf, R. J. Colchin, L. Zeng, G. Wang, J. G. Watkins, and T. Takahashi, Phys. Plasmas **12**, 072516 (2005).
[274] G. R. Tynan, C. Holland, J. H. Yu, A. James, D. Nishijima, M. Shimada, and N. Taheri, Plasma Phys. Controlled Fusion **48**, S51 (2006).
[275] P. B. Snyder, H. R. Wilson, and X. Q. Xu, Phys. Plasmas **12**, 056115 (2005).
[276] P. Ricci and B. N. Rogers, Phys. Rev. Lett. **104,** 145001 (2010).
[277] T. Yamada, S.-I. Itoh, S. Inagaki, Y. Nagashima, N. Kasuya, K. Kamataki, H. Arakawa, T. Kobayashi, M. Yagi, A. Fujisawa, and K. Itoh, Phys. Rev. Lett. **105**, 225002 (2010).
[278] S. J. Zweben, R. J. Maqueda, R. Hager, K. Hallatschek, S. M. Kaye, T. Munsat, F. M. Poli, A. L. Roquemore, Y. Sechrest, and D. P. Stotler, Phys. Plasmas **17**, 102502 (2010).
[279] T. Ribeiro and B.D. Scott, Plasma Phys. Controlled Fusion, **47**, 1657 (2005).
[280] R. Sanchez, B. P. v. Milligen, D. E. Newman, B. A. Carreras, and Phys. Rev. Lett. 90, Phys. Rev. Lett. **90**, 185005 (2003).
[281] P. H. Diamond, S.-I. Itoh, K. Itoh, and T. S. Hahm, Plasma Phys. Controlled Fusion **47**, R35 (2005).
[282] P. Ricci, B. N. Rogers and S. Brunner, Phys. Rev. Lett. **100**, 225002 (2008).
[283] I. Cziegler, J. L. Terry, J. W. Hughes, and B. LaBombard, Phys. Plasmas **17**, 056120 (2010).

[284] Z. Yan, M. Xu, P.H. Diamond, C. Holland, S. H. Müller, G. R. Tynan, and J. H. Yu, Phys. Rev. Lett. **104**, 065002 (2010).

[285] Z. Yan, J. H. Yu, C. Holland, M. Xu, S. H. Müller, and G. R. Tynan, Phys. Plasmas **15**, 092309 (2008).

[286] "Transport of momentum in the SOL of ASDEX UPGRADE," F. Mehlmann, C. Ionita, V. Naulin, J.J. Rasmussen, H.W. Müller, N. Vianello, Ch. Maszl, V. Rohde, M. Zuin, R. Cavazzana, M. Maraschek, R. Schrittwieser, *Proceedings of the 37th EPS Conference on Plasma Physics*, (EPS, Dublin, 2010), paper P1-1064.

[287] P. B. Parks and L. R. Baylor, Phys. Rev. Lett. **94**, 125002 (2005).

[288] B. Gonçalves, C. Hidalgo, M. A. Pedrosa, R. O. Orozco, E. Sánchez, and C. Silva, Phys. Rev. Lett. **96**, 145001 (2006).

[289] C. Hidalgo, B. Gonçalves, C. Silva, M. A. Pedrosa, K. Erents, M. Hron, and G. F. Matthews, Phys. Rev. Lett. **91**, 065001 (2003).

[290] J. P. Gunn, C. Boucher, M. Dionne, I. Ďuran, V. Fuchs, T. Loarer, I. Nanobashvili, R. Pánek, J.-Y. Pascal, F. Saint-Laurent, J. Stöckel, T. V. Rompuy, R. Zagórski, J. Adámek, J. Bucalossi, R. Dejarnac, P. Devynck, P. Hertout, M. Hron, G. Lebrun, P. Moreau, F. Rimini, A. Sarkissian, and G. Van Oost, J. Nucl. Mater. **363–365**, 484 (2007).

[291] B. LaBombard, B. LaBombard, J.E. Rice, A.E. Hubbard, J.W. Hughes, M. Greenwald, J. Irby, Y. Lin, B. Lipschultz, E.S. Marmar, C.S. Pitchera, N. Smick, S.M.Wolfe, S.J. Wukitch and the Alcator Group, Nucl. Fusion **44**, 1047 (2004).

[292] "Experimental investigation on the poloidal extent of the turbulent radial flux in tokamak scrape-off layer," N. Fedorczak, J.P. Gunn, G. Bonhomme, F. Brochard, H. Bufferand, G. Ciraolo, M. Farge, Ph. Ghendrih, J.P. Gunn, P. Hennequin , L. Isoardi, R. Nguyen, C. Reux, F. Schwander, P. Tamain, and L. Vermare, J. Nucl. Mater. (in press, 2010).

[293] W. Fundamenski and W. Sailer, Plasma Phys. Controlled Fusion **46**, 233 (2004).

[294] J. H. Yu, J. A. Boedo, E. M. Hollmann, R. A. Moyer, D. L. Rudakov, and P. B. Snyder, Phys. Plasmas **15**, 032504 (2008).

[295] "Parallel expansion of density bursts," G. Chiavassa, H. Bufferand, G. Ciraolo, Ph. Ghendrih, H. Guillard, L. Isoardi, A. Paredes, F. Schwander, E. Serre, P. Tamain, J. Nucl. Mater. (in press, 2010).

[296] "The effect of plasma fluctuations on parallel transport parameters in the SOL," E. Havlíčková, W. Fundamenski, V. Naulin, A. H. Nielsen, J. Seidl, J. Horáček, J. Nucl. Mater. (in press, 2010).

[297] V. Rozhansky, I. Veselova, and S. Voskoboynikov, Plasma Phys. Controlled Fusion **37**, 399 (1995).

[298] N. Vianello, M. Spolaore, E. Martines, R. Cavazzana, G. Serianni, M. Zuin, E. Spada and V. Antoni, Nucl. Fusion **50**, 042002 (2010).

[299] N. Mizuguchi, R. Khan, T. Hayachi, and N. Nakajima, Nucl. Fusion **47**, 579 (2007).

[300] R. Khan, N. Mizuguchi, N. Nakajima, and T. Hayachi, Phys. Plasmas **14**, 062302 (2007).

[301] C. R. Sovinec, D. D. Schnack, A. Y. Pankin, D. P. Brennan, H. Tian, D. C. Barnes, S. E. Kruger, E. D. Held, C. C. Kim, X. S. Li, D. K. Kaushik, S. C. Jardin, and the NIMROD team, J. Phys.: Conf. Ser. **16**, 25 (2005).
[302] H. R. Strauss, L. Sugiyama, C. S. Chang, G. Y. Park, S. Ku, W. Park, J. Breslau, and S. Jardin, in *Proceedings of the 21st IAEA Fusion Energy Conference*, 16–20 October 2006, Chengdu (IAEA, Vienna, 2006), paper IAEA-CN-116/TH/P8-6.
[303] L. E. Sugiyama and H. R. Strauss, Phys. Plasmas **17**, 062505 (2010).
[304] H. Takahashi, E. D. Fredrickson, and M. J. Schaffer, Phys. Rev. Lett. **100**, 205001 (2008).
[305] A. Kirk, H. R. Wilson, R. Akers, N. J. Conway, G. F. Counsell, S. C. Cowley, J. Dowling, B. Dudson, A. Field, F. Lott, B. Lloyd, R. Martin, H. Meyer, M. Price, D. Taylor, M. Walsh, and the MAST team, Plasma Phys. Controlled Fusion **47**, 315 (2005).
[306] B. Kurzan, H. D. Murmann, and J. Neuhauser, Phys. Rev. Lett. **95**, 145001 (2005).
[307] R. Scannell, A. Kirk, N. B. Ayed, P. G. Carolan, G. Cunningham, J. McCone, S. L. Prunty, and M. J. Walsh, Plasma Phys. Controlled Fusion **49**, 1431 (2007).
[308] A. Kirk, B. Koch, R. Scannell, and G. C. H. R. Wilson, J. Dowling, A. Herrmann, R. Martin, M. Walsh and the MAST team, Phys. Rev. Lett. **96**, 185001 (2006).
[309] H. R. Wilson and S. C. Cowley, Phys. Rev. Lett. **92**, 175006 (2004).
[310] G.Y. Antar, S.I. Krasheninnikov, P.B. Snyder, R.A. Moyer, R. Pugno and D.S. Gray, Nucl. Fusion **49**, 032001 (2009).
[311] S. J. Zweben, B. D. Scott, J. L. Terry, B. LaBombard, J. W. Hughes, and D. P. Stotler, Phys. Plasmas **16**, 082505 (2009).
[312] T. Munsat and S. J. Zweben, Rev. Sci. Instrum. **77**, 103501 (2006).
[313] "New approach in multi-fluid modeling of edge plasma transport with high intermittency due to blobs and ELMs," A.Yu. Pigarov, S. I. Krasheninnikov, and T. D. Rognlien, Bull. Am. Phys. Soc. **55**, 280 (2010), paper PP9-145.
[314] Peter C. Stangeby, *The Plasma Boundary of Magnetic Fusion Devices*, (Institute of Physics Publishing, Bristol and Philadelphia, PA, 2000).
[315] D. Jovanovic, P.K. Shukla and F. Pegararo Phys. Plasmas **15**, 112305 (2008).